Technische Universiteit Delft

Automated implant configuration optimisation for high dose rate brachytherapy

Remco Dirks

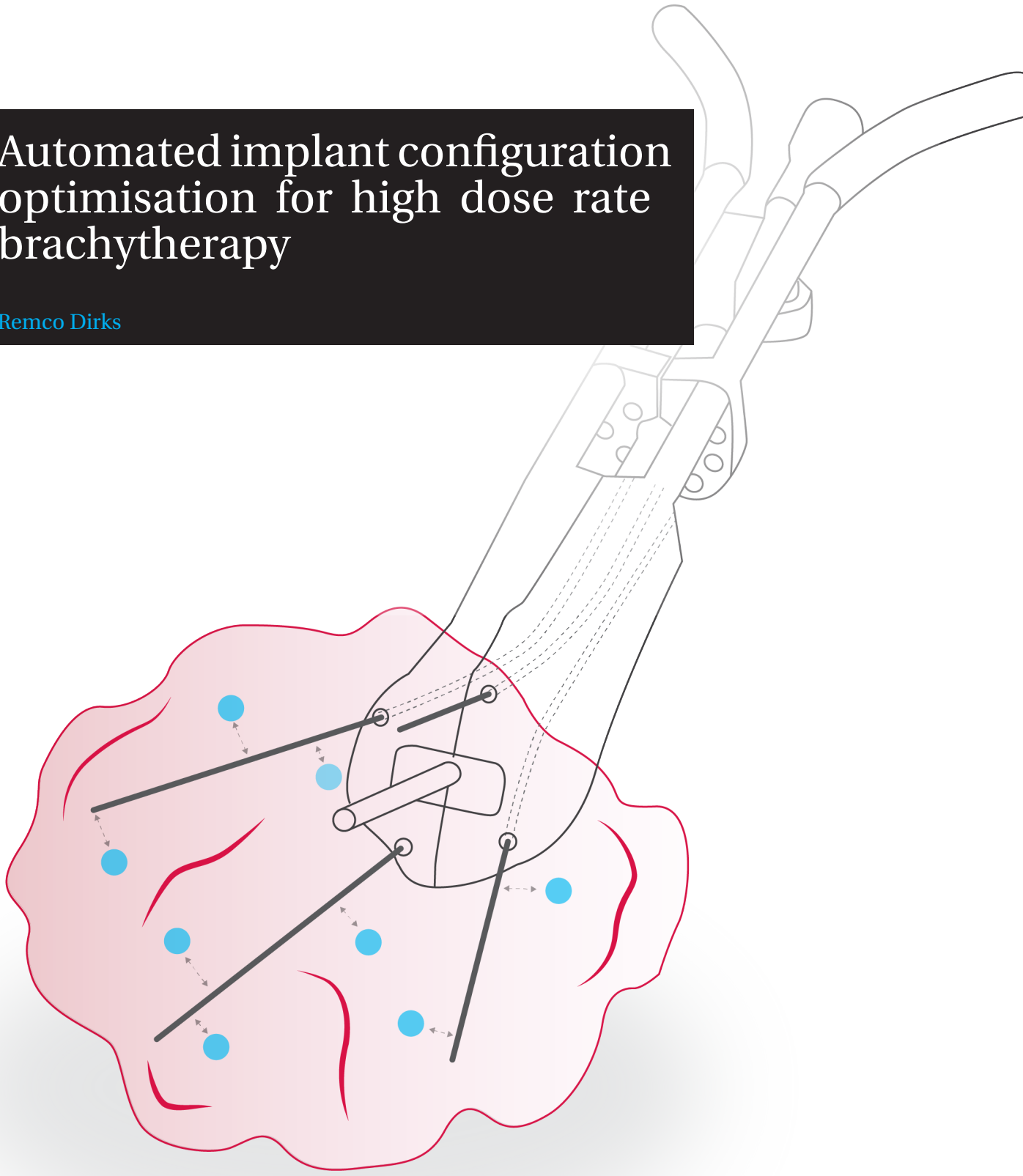

TU Delft Delft University of Technology

Challenge the future

AUTOMATED IMPLANT CONFIGURATION OPTIMISATION FOR HIGH DOSE RATE BRACHYTHERAPY

Master thesis

By
Remco Dirks

March 25, 2024

Student number:	4708776
Faculty:	Mechanical Engineering (ME)
Master:	Robotics
Main supervisor:	Dr. Javier Alonso-Mora
Daily supervisor:	Ir. Robin Straathof

TU Delft Delft University of Technology

PREFACE

Reflecting on the completion of this master's thesis, I am filled with a deep sense of gratitude for the individuals who have supported me along the way. Moreover, I am thankful I was allowed to work on the ARCHITECT research conducted by the TU Delft and the Erasmus Medical Centre and happy I could contribute to better treatments for cervical cancer patients. This work has been enriched and made possible by the contributions and encouragement of both my professional and personal circles.

First and foremost, I wish to express my gratitude to my supervisors. Their expert guidance, valuable insights, and support have been essential for this research. I thank Javier for his valuable insights into potential path-planning methods and for seeking additional perspectives from colleagues; Robin, my daily supervisor, for his continuous help and good talks about the different topics in this thesis. Without your unwavering enthusiasm and willingness to help, this thesis would not have been the same; and Linda, for making time for my questions about BiCycle and implementing the option to use BiCycle on a grid. Moreover, I would like to thank all members of my graduation committee for their time and effort in reviewing my work.

I am also thankful to my family and friends, who have always encouraged me during this project's most challenging periods. Their supportive presence and listening ears, especially during coffee breaks, were essential throughout this project.

As I step forward into the next phase of my career, I carry with me not only the technical knowledge and skills gathered during this project but also the appreciation and enthusiasm of all the people around me.

Remco Dirks
Delft, March 2024

ABSTRACT

Brachytherapy (BT) is an essential component in the curative treatment of cervical cancer. With commercial BT implant devices, called applicators, the radioactive sources can only be positioned in fixed intracavitary channels or in a fixed array of interstitial needles. Patient-tailored BT applicators containing individualised needle channels have the potential to enhance the delivered dose to the tumour while minimising tissue damage of the organs-at-risk (OARs). During the optimisation process of the needle channels, several constraints must be considered. The needle paths in the applicator are curvature-constrained, and the needles should not collide with each other or potentially perforate OARs. Furthermore, clinicians can impose additional constraints based on their preferences.

Existing approaches in literature for optimising needle placement in patient-tailored BT applicators for cervical cancer treatment have employed various algorithms. However, these approaches often rely on significant approximations. For instance, some assume that all needles are inserted in parallel or focus solely on optimising geometric coverage as opposed to optimising the dose distribution. Moreover, the few methods in literature incorporating needle path planning in the optimisation process require manually pre-specified dwell positions. To improve dose conformity and minimise the dependence on the clinician's expertise and time, there is a need for the development of software that optimises the needle placement and paths without resorting to these severe assumptions.

This work proposes and validates a novel three-stage approach to generate a patient-tailored applicator configuration without resorting to fully geometric optimisation. First, a high-potential set of dwell positions is obtained by running a modified version of the dwell time optimisation software BiCycle (Erasmus Medical Centre, Rotterdam, the Netherlands) on a grid of possible dwell positions. This results in a resolution optimal treatment plan when not considering geometry and applicator constraints. The positions with the highest dwell times according to the resolution optimal treatment plan are selected in the high-potential set. Next, a weighted set cover problem is used iteratively to find a combination of feasible needle segments to cover all dwell points in the high-potential set at a minimum distance. Lastly, needle channels to steer the needle to these segments are simultaneously optimised to be of minimum curvature and mutually collision-free.

To evaluate our approach, a virtual configuration and planning study was performed in a cohort of 22 locally advanced cervical cancer patients previously treated with the Venezia (Elekta AB, Stockholm, Sweden). The resulting treatment plans of the clinically used configuration were compared with the resulting treatment plans of the proposed patient-tailored and grid configurations on clinically relevant dose-volume histogram parameters, dwell times, conformity index and number of interstitial needles. Statistical significance is assessed with Wilcoxon signed-rank tests.

The proposed workflow was demonstrated to be feasible, and for every patient, a configuration could be generated in clinically acceptable time. All treatment plans generated for the grid configuration, the patient-tailored configuration and the clinical configuration were acceptable following the EMBRACE ll aims. Planning aims, however, were met more frequently with both the grid configurations (145/151 instances) and the patient-tailored configurations (137/151 instances) in comparison with the clinically used configurations (119/151 instances). The treatment plans generated with the grid configurations obtained significantly better ($p < 0.01$) median normalised CTV_{IR} D_{98} dose with respect to the clinical configurations. Moreover, with the grid configurations, there was a significant improvement in median normalised D_{2cm^3} dose for the bladder ($p < 0.001$), rectum ($p < 0.001$), sigmoid ($p < 0.01$) and bowel ($p < 0.001$) compared to treatment plans obtained with the clinical configurations. The treatment plans generated with the patient-tailored configurations obtained comparable target doses, but median normalised D_{2cm^3} doses for the bladder ($p < 0.001$), rectum ($p < 0.01$) and bowel ($p < 0.01$) were significantly better for the patient-tailored configurations compared to the clinical configurations.

The proposed automated patient-tailored BT source channel configuration planning method was demonstrated to be clinically feasible. The resulting treatment plans have dosimetric advantages over the treatment plans generated with the clinical applicator configuration. Improvements to the intracavitary dwell position placement are expected to further increase dose conformity.

PRELIMINARIES

0.1. LIST OF ABBREVIATIONS

AI	Artificial Intelligence
BED	Biologically Effective Dose
BT	Brachytherapy
COIN	Conformity Index
CTV	Clinical Target Volume
DIs	Dosimetric Indices
DVH	Dose Volume Histogram
EBRT	External Beam Radiation Therapy
EQD2	Equieffective Dose in 2 Gray Fractions
GTV	Gross Tumour Volume
Gy	Gray
HDR	High-Dose-Rate
HR	High-Risk
IC	Intracavitary
ILP	Integer Linear Program
IMRT	Intensity Modulated Radiation Therapy
IR	Intermediate-Risk
IS	Interstitial
IQR	Interquartile Range
IU	Intrauterine
LS	Local Search
MRI	Magnetic Resonance Imaging
OAR	Organ At Risk
RFAT	Radio-Frequency Ablation Therapy
RRT	Rapidly-Exploring Random Tree
SCP	Set Cover Problem
TrajOpt	Trajectory Optimisation
VCP	Vertex Cover Problem
WSCP	Weighted Set Cover Problem

0.2. NOMENCLATURE

	Radiotherapy
D	Total dose of radiation delivered
u	Total number of fractions
d	Dose delivered per fraction
$\frac{a}{b}$	Tissue-specific radiosensitivity ratio
D_V	Dose in Gy that is received by at least a volume V
V_D	Partial volume that receives a dose of at least D
	Coverage problem
U	Ground set of n candidate dwell points
n	Number of candidate dwell points in the high-potential ground set
$\mathbb{S}$	Candidate set of m candidate needle segments
m	Number of candidate needle segments in candidate set
c_s	Non-negative cost of needle s
x_s	Denotes if needle s has been selected
$A_{s,j}$	Denotes if dwell point j has been covered by needle s
C	Collision matrix
d_c	Cover distance
$d_{s,j}$	Distance between needle s and dwell point j
N_{max}	Maximum number of selected needles
$\mathbb{B}$	Pairwise validity matrix
	Path planner
$b_n^i(t)$	Bernstein's polynomial basis
c_j	Set of control points of the jth piece of the Bézier curve
E_{bend}	Bending energy
κ	Curvature of the needle path
k	Derivative order
n	Bezier curve order
μ	Index denoting one of the three orthogonal dimensions
$\mathbb{M}$	Set containing all m selected needles by the weighted set cover
$\hat{v}_q$	Direction of the needle segment q
$\hat{u}$	Upward direction in the entry region
$d_{\text{y,z,fast}}$	The distance between needles m and z or between needle m and part z of the IU tandem structure according to the fact-checking algorithm
$d_{\text{y,z,needed}}$	The required distance between needles m and z or between needle m and part z of the IU tandem structure
$\mathbb{T}$	Set containing the small and large tubes of the IU tandem structure

CONTENTS

List of Figures

List of Tables

1 INTRODUCTION

1.1. BACKGROUND

Cervical cancer ranks as the fourth most frequently diagnosed cancer and the fourth leading cause of cancer death in women [1]. Due to this form of cancer, an estimated 342,000 deaths occurred worldwide in 2020 [2]. High-dose-rate (HDR) brachytherapy (BT) is an important part of the curative treatment of locally advanced cervical cancer and is often used as a boost to external beam radiation therapy (EBRT) [3].

In BT the radioactive source is placed in close proximity to or inside the tumour. An afterloader drives this source through intracavitary (IC) channels in an implant device - called an applicator - or interstitial (IS) needles guided by this implant. The main goal of HDR-BT is to maximise the radiation in the target region whilst minimising the radiation to the organs at risk (OARs, including the rectum, sigmoid, bowel and bladder for cervical cancer) as much as possible. To achieve this, treatment planning is essential. Treatment planning involves determining the dwell time the source is positioned at prespecified locations, called dwell positions. In conventional applicators, the dwell positions are fixed due to the ability to only select from a standard configuration of needles and source channel sizes. Therefore, target coverage and local control with conventional applicators remain sub-optimal for large or complex tumours or difficult anatomies [4]. In addition, high dose to organs leads to frequent side effects and reduces the quality of life [5]. Figure 1.1a shows the conventional Utrecht IS/IS CT/MR applicator, and Figure 1.1b shows an example dose distribution.

(a) Utrecht IC/IS CT/MR applicator.

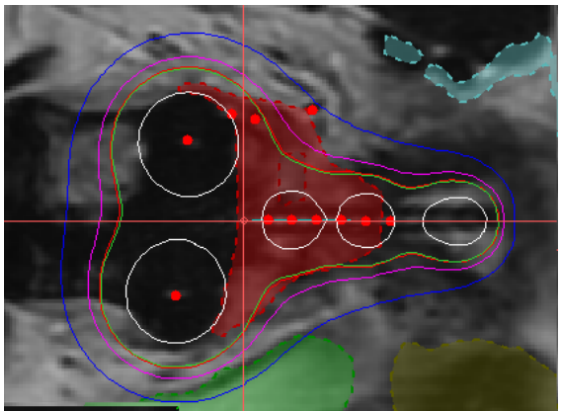

(b) A slice of an example dose distribution. The dwell positions are shown in red. The white, pink, green, and blue lines are the iso-dose lines. Image taken from [6].

Figure 1.1: Example of a conventional applicator (a) and a slice of an example dose distribution (b).

Due to recent developments, applicators can now be patient-tailored. This has the following foreseen benefits: i) increased target coverage and absorbed dose to the target volume with reduced or equal trauma to the surrounding tissues and organs at risk (OARs), ii) improved needle guidance and minimisation of the required number of needles and iii) reliable and comfortable placement [7]. An example of a patient-tailored applicator is the ARCHITECT applicator, which contains optimised source channels. The vaginal vault, the clinical target volumes, and the OARs are segmented on MR images. The outer shape of the ARCHITECT applicator is based on the shape of the vaginal cavity. After shape and source channel determination, the applicator is 3D printed [8]. In the current ARCHITECT concept, the 3D-printed halves are used as add-ons to the Elekta Geneva IU tandem. Figure 1.2a shows the ARCHITECT applicator, and Figure 1.2b shows a schematic representation of an applicator implanted in a patient.

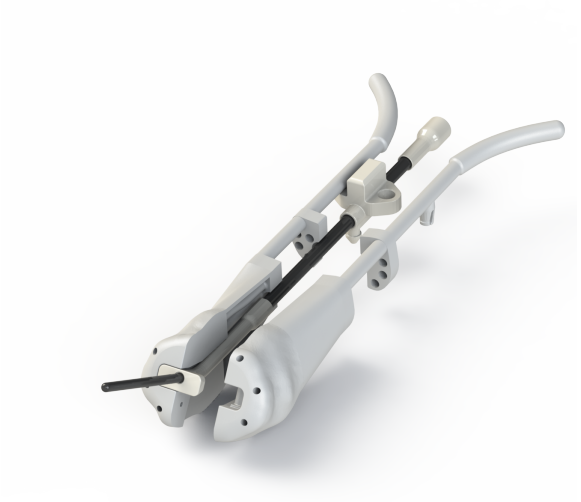

(a) Custom 3D-printed ARCHITECT applicator.

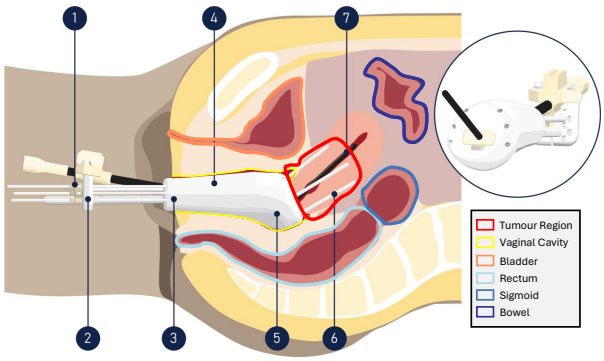

(b) Schematic visualisation of the ARCHITECT applicator implanted in a patient with relevant structures annotated. The marked parts are the following: (1) needle lock insert (Elekta), (2) needle template, (3) entry region, (4) swept section, (5) patient-tailored top, (6) ProGuide IS needle (Elekta), and (7) Geneva IU tandem (Elekta). Image taken and adapted from [9].

Figure 1.2: The patient-tailored 3D-printed ARCHITECT applicator shown with parts separated (a) and implanted in a patient (b).

Treatment planning in HDR-BT is fundamentally multi-objective and concerns qualitative aspects that make a plan or implant suitable. Regarding treatment planning, trade-offs between the dose in the target regions and OARs must be accomplished. Moreover, homogeneity in the dwell times is preferred [10]. Another important aspect to consider is that hot spots, very high dose regions, and cold spots, regions with substantial dose deficits, should be prevented [11], [12]. Regarding catheter placement, clinicians want safety margins between the needle and OARs to avoid perforation. Lastly, if a needle is inserted at an excessively steep angle relative to the outward normal of the tissue, there is a risk of the needle sliding along the tissue surface rather than penetrating it. Such deviations lead to imprecise needle placement and thus, must be prevented.

Treatment planning for conventional applicators long concerned manual dwell time modifications, a trial and error process dependent on time and skills of the treating physician [13]. Several automated dwell time optimisation approaches have been proposed which demonstrate superiority over manually generated plans [14] - [16]. With the increased flexibility of source positioning due to patient-tailored applicators, manual planning will become increasingly complex, substantially increasing the need for automated needle and dwell position planning. Additionally, as the patient-tailored ARCHITECT applicator channels are used to steer the needles, the optimisation should also consider source channel planning. Since not all catheter placements lead to feasible source channels, the dwell position optimisation should also consider the feasibility of the channels.

This study aims to combine dwell time optimisation and source channel planning for interstitial needles without resorting to fully geometric coverage planning. This work proposes a three-stage approach. First, a high-potential set of dwell positions is obtained by running a modified version of the dwell time optimisation software BiCycle (Erasmus Medical Centre, Rotterdam, the Netherlands) on a grid of possible dwell positions [14]. This results in a resolution optimal treatment plan when not considering geometry and applicator constraints. The positions with the highest dwell times according to the resolution optimal treatment plan are selected in the high-potential set. Next, a weighted set cover problem is used iteratively to find a combination of feasible needles to cover all dwell points in the high-quality set at a minimum distance. Lastly, needle channels to the applicator's entry region are simultaneously optimised to be of minimum curvature and mutually collision-free. Channel centrelines are represented by Bézier curves, which enables fast collision checking to be used. The proposed method and the grid configuration are validated based on virtual treatment plans in a representative patient cohort.

1.2. THESIS STRUCTURE

Several fundamental concepts in BT that are required for obtaining an understanding of the presented method and results are introduced in Chapter 2. Readers familiar with BT can skip this chapter missing no crucial information. Those new to the subject are advised to read this chapter before proceeding with the rest of the thesis.

Chapter 3 discusses works related to the method proposed in this thesis, focusing on the set cover problem and path-planning methods in radiotherapy or related fields.

The main results and the novel method of this thesis are presented in Chapter 4 in the form of an article. The paper proposes a method to combine dwell time optimisation and source channel planning for the interstitial needles without resorting to fully geometric coverage planning. The proposed method and the used grid configuration are validated based on virtual treatment plans in a representative patient cohort.

Supplementary explanation of the concepts proposed in the paper is presented in Chapter 5. In Chapter 6 more results are presented and discussed that give valuable insights in the proposed method but are not shown in the paper. Furthermore, a component-based analysis of the proposed methodology is presented in this chapter.

2 FUNDAMENTAL CONCEPTS IN BRACHYTHERAPY

In this chapter, different BT concepts that are used in this work will be explained. The concepts discussed and the corresponding sections are: the regions of interest for HDR-BT (Section 2.1), the different treatment categories in BT (Section 2.2), the combination of BT with EBRT (Section 2.3), the dose definitions and calculations used in this work (Section 2.4), the treatment planning aims (Section 2.5), and the BiCycle optimisation algorithm (Section 2.6).

2.1. REGIONS OF INTEREST

The main goal of HDR-BT is to maximise the radiation in the target region whilst minimising the radiation to the OARs. The target region for cervical cancer consists of different volumes. One of these volumes is the Gross Tumour Volume (GTV), the primary tumour volume with the highest tumour cell density. The GTV_{Res} is the residual gross tumour volume, indicating the amount of visible tumour that remains post-surgery or after EBRT. Another relevant volume is the Clinical Target Volume (CTV), which consists of the GTV and any volume suspected of containing microscopic disease. There are two different CTV areas: the first is the CTV High-Risk (CTV_{HR}) and the second is the CTV Intermediate-Risk (CTV_{IR}). The CTV_{HR} is always entailed in the CTV_{IR}. The high and intermediate risk split allows for tailored radiation therapy plans to maximise the treatment effect on the tumour while minimising the damage to healthy tissue. OARs that are considered in cervical cancer HDR-BT are the bladder, rectum, sigmoid and small bowel. In Figure 2.1 the delineation of the volumes of interest, the target region and the OARS on an MRI image is shown.

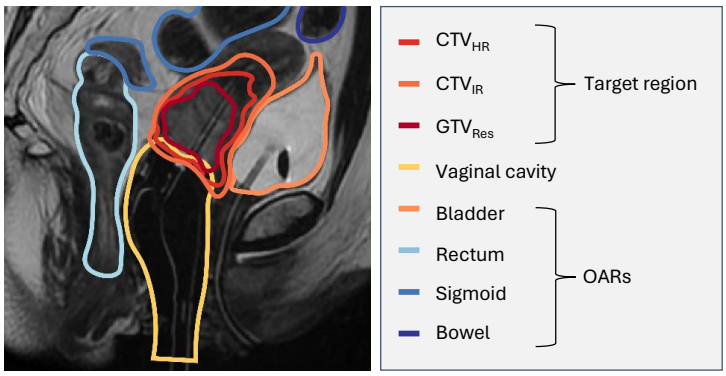

Figure 2.1: Delineation of regions of interest on a sagittal T2 weighted MR image.

2.2. BRACHYTHERAPY TREATMENT CATEGORIES

Different categories of BT treatment types can be distinguished based on the rate at which the radiation dose is administered. HDR-BT is characterised by the delivery of a high radiation dose over a short duration, typically minutes per session, necessitating the temporary placement of the radioactive source. HDR-BT is often defined as brachytherapy with an absorbed dose rate larger than 12 Gy/h [17]. On the other side, low-dose-rate BT involves the administration of radiation at a lower dose rate over a prolonged period, often days, with the radioactive sources either permanently implanted in the form of seeds or temporarily placed [18]. The focus of this thesis will be on HDR-BT.

2.3. TREATMENT SCHEDULE

As stated HDR-BT is often used in combination with EBRT. Typically, HDR-BT is applied in the last 2-3 weeks of the radiotherapy, with both treatment types accounting for approximately half of the resulting biologically effective dose [17]. HDR-BT mostly consists of 3 or 4 fractions, where a fraction is a continuous irradiation period with a specified absorbed dose. The decision to use 3 or 4 fractions in the total treatment is made based on the ability to meet the planning constraints and aims. Therefore, the patients receiving 4 fractions generally have more complicated anatomies than patients receiving 3 fractions. Examples of a dose delivery schedule for 4 HDR-BT fractions in combination with EBRT can be seen in Figure 2.2. The visualisation only shows example treatment schedules; the exact treatment schedule differs from clinic to clinic and from patient to patient, and preferred schedules change over time.

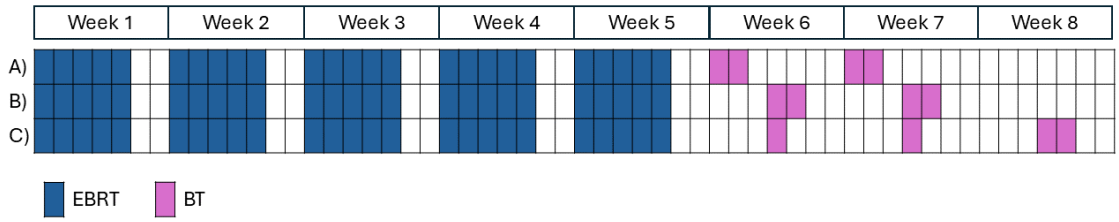

Figure 2.2: Visualisation of example overall treatment schedules for radiotherapy combining 25 fractions of EBRT (typically 1.8 Gy per fraction) and 4 fractions in 2 or 3 applications (continuous applicator insertion periods) of BT for the curative treatment of cervical cancer. The example configurations are: A) the proposed EMBRACE workflow 1. B) the proposed EMBRACE workflow 2. C) a typical Erasmus Medical Centre workflow. A coloured block illustrates a single fraction in the treatment. Image extracted and adapted from [19].

The procedure of the Erasmus Medical Centre of applying a single fraction consists of different steps [20]:

1. *Implantation preparation:* The patient is checked and prepared to be transferred to the operating room by a nurse in the short-stay unit.
2. *Implantation of the applicator:* After the patient is anaesthetised, a urinary catheter and the applicator are implanted.
3. *Recovery from implantation:* The patient recovers from the applicator implantation in the recovery room while vital signs are monitored.
4. *Waiting before imaging:* The patient is returned to the short-stay unit to wait until the imaging room is free.
5. *Imaging:* The patient's bladder is filled in the imaging room, and MRI images are made.
6. *Treatment planning:* The patient waits in the short stay unit and is regularly checked by a nurse.
   (a) The contours of the target volumes and the OARs are delineated by one radiation oncologist and verified by another.
   (b) At the same time, the applicator, catheters and relevant points are reconstructed by one radiotherapy technologist and verified by another.
   (c) After approval of both steps, the radiotherapy technologist initially makes a treatment plan. This plan is verified and optimised by the radiotherapy technologist, radiation oncologist, and medical physicist together.
7. *Treatment delivering:* The treatment plan is uploaded to the afterloader and the patient is transferred to the treatment room. The applicator is connected to the afterloader and after checking all source channels with a dummy source the irradiation begins.
8. *Removal of applicator:* The applicator is removed.
9. *Recovery:* The patient recovers in the short stay unit until the patient can be discharged.

2.4. DOSE DEFINITIONS AND CALCULATIONS

2.4.1. EQD2

The equieffective dose in 2 Gy fractions (EQD2) is used in radiation oncology to compare the biological effectiveness of different radiation therapy regimens with varying fraction sizes and total doses [21]. It provides a standardised way to evaluate and compare the effects of radiation treatments delivered in different schedules but intended to achieve similar therapeutic outcomes. This concept is particularly important when considering treatments with combined BT and EBRT as the EQD2 allows for simple addition of the doses delivered in both modalities. The EQD2 is based on the linear-quadratic model, which describes the relationship between the dose of radiation and the biological effect it produces in tissues [22]. In the calculation of the EQD2, the biologically effective dose (BED), a predictor of the biological effect as a function of the delivered dose, is used. The formulas to calculate the BED and the EQD2 for one treatment modality are shown below [23]:

$$\text{BED} = u \cdot d \left(1 + \frac{d}{\alpha/\beta}\right) \tag{2.1}$$

$$\text{EQD2} = \frac{BED}{\left(\frac{2}{\alpha/\beta} + 1\right)} \tag{2.2}$$

Here, u is the total number of fractions, d is the physical dose delivered per fraction and $\frac{\alpha}{\beta}$ is the tissue-specific radiosensitivity ratio. In this work, the target volumes are assumed to have a uniform radiosensitivity ratio of 10 Gy and the OARs have a uniform radiosensitivity of 3 Gy [17].

2.4.2. DOSE VOLUMETRIC HISTOGRAM

The dose-volume histogram (DVH) is a fundamental tool in radiation therapy planning and analysis [24], as it summarises the dose distribution within the target volume and surrounding tissues [25]. As clinical outcomes are related to these DVH parameters, the latter are often used for treatment planning and prescription [26], e.g., in EMBRACE II planning aims or limits [27]. Dose parameters are also known as dosimetric indices (DIs). Two types of parameters are extracted from DVHs: the dose and volume parameters. The dose parameter (D_V), measured in Gray (Gy), refers to the specific level of radiation received by the tissue volume (V), expressed in percentage or cm^3 [28]. Similarly, the volume parameter (V_D), measured in percentage or cm^3, refers to the partial volume (V) that receives a dose of at least D. These dose parameters are respectively defined as:

$$D_V = \{D(v) \mid v \geq V\} \tag{2.3}$$

$$V_D = \{V(\mathscr{D}) \mid \mathscr{D} \geq D\} \tag{2.4}$$

The DVH parameters used in this study for the target volumes are the $D_{90\%}$ and the $D_{98\%}$. For the OARs, the recommended DVH parameter is the D_{2cm^3} [17].

There are several limitations to the use of DVH parameters. One main limitation of the DVH parameters is that these reduce the spatial dosimetric information into two-dimensional dose-volume relations, resulting in valuable information being lost. For example, DVHs cannot indicate where within a structure hot or cold spots are present [28]. Similarly, an asymmetric dose distribution over a specified volume could result in a similar DVH as when computed for a symmetric dose distribution over the same volume [29]. Furthermore, as treatment progresses and time elapses, there might be changes to the patient's anatomy (i.e. patients lose weight, tumours shrink, organs change shape) [30].

2.5. TREATMENT PLANNING AIMS

The treatment planning aims used in the Erasmus Medical Centre are based on the EMBRACE II study by the gynaecological working group of the European Society, GYN GEC-ESTRO [17]. The planning must adhere to treatment aims (soft limits) and dose limits (hard limits). These constraints and objectives are based on the DIs. In some cases not all planning aims can be met and in other cases it is possible to find

a better plan according to all DIs. In Table 2.1, a simplified clinical planning protocol with constraints and goals for the different DIs of the target volume and the different OARs is shown.

Table 2.1: A simplified clinical planning protocol from the EMBRACE II study [27]. In this study, the EQD2 is used as a unit for the dose. For the target volume the EQD2 is the $EQD2_{3Gy}$ and for the OAR the EQD2 is the $EQD2_{10Gy}$.

Region	DI	Hard limit (EQD2)	Aim (EQD2)
CTV_{HR}	$D_{90\%}$	≥ 85 Gy	≥ 90 Gy, ≤ 95 Gy
CTV_{HR}	$D_{98\%}$	≥ 90 Gy	≥ 95 Gy
CTV_{IR}	$D_{98\%}$	-	≥ 75 Gy
Bladder	D_{2cm^3}	≤ 90 Gy	≤ 80 Gy
Rectum	D_{2cm^3}	≤ 75 Gy	≤ 65 Gy
Sigmoid	D_{2cm^3}	≤ 75 Gy	≤ 70 Gy
Bowel	D_{2cm^3}	≤ 75 Gy	≤ 70 Gy

As can be seen in Table 2.1, the planning aims and hard limits are given in EQD2. Assuming that all BT fractions deliver an equal dose and there are 25 EBRT fractions with a dose of 1.8 Gy per fraction, the first fraction BT planning aims in Gy according to the EMBRACE ll study are shown in Table 2.2 for 3 and 4 fractions. In practice, treatment is adaptive, and prescribed doses in subsequent fractions are changed accordingly. However, in this work, all fractions are assumed to deliver equal doses to calculate the projected total dose of treatment based on the first fraction.

Table 2.2: The planning aims in Gy for 3 and 4 BT fractions, corresponding to Table 2.1, assuming that all BT fractions deliver an equal dose and there are 25 EBRT fractions with a dose of 1.8 Gy per fraction.

Region	DI	3 fractions	4 fractions
CTV_{HR}	$D_{90\%}$	≥ 9.42 Gy, ≤ 10.10 Gy	≥ 7.74 Gy, ≤ 8.31 Gy
CTV_{HR}	$D_{98\%}$	≥ 7.17 Gy	≥ 5.83 Gy
CTV_{IR}	$D_{98\%}$	≥ 4.38 Gy	> 3.50 Gy
Bladder	D_{2cm^3}	≤ 6.47 Gy	≤ 5.45 Gy
Rectum	D_{2cm^3}	≤ 4.71 Gy	≤ 3.93 Gy
Sigmoid	D_{2cm^3}	≤ 5.35 Gy	≤ 4.48 Gy
Bowel	D_{2cm^3}	≤ 5.35 Gy	≤ 4.48 Gy

2.6. BiCycle

As stated before, the treatment planning problem is multi-objective. The multi-objective optimisation used in this work is the BiCycle algorithm [14], which was developed in the Erasmus Medical Centre. BiCycle is based on a wishlist approach. The multi-objective problem is stated as a sequential optimisation of single-objective problems in which a pre-specified wishlist determines the optimisation order. After every single objective optimisation, the found solution is added as a new constraint for the following optimisations. Some tolerance on the found solution is added to ensure enough space to optimise in the following optimisations. After optimising each criterion, the second phase is started. In this phase, all objectives that meet their goal are further optimised while keeping all other objectives constrained.

3 RELATED WORK

3.1. TREATMENT PLANNING

Patient-tailored applicator planning requires both dwell time optimisation and catheter placement optimisation. This section lists some of the methods proposed in the literature.

Treatment planning for conventional applicators concerned dwell time modifications and was performed manually, a trial and error process that takes a long time and is dependent on the skills of the clinician [13]. With the use of optimisation models, the treatment plan quality can be improved [31].

There are different types of approaches to dwell time optimisation. Firstly, there are penalty models such as linear penalty models [32], [33], and quadratic penalty models [34]. Secondly, single objective dose-volume optimisation models have been proposed. Some single objective dose-volume models solve a mixed integer linear program [35], use a heuristic to simplify the problem [36], or use a Heaviside function approximation [37]. As an alternative to dose-volume optimisation, optimisation using mean-tail-dose models has been suggested [38]. Lastly, there are three multi-objective dose-volume models: BiCycle [37], GOMEA [39], [40], and gMCO [15].

The run time of these automated multi-objective dose-volume model approaches to arrive at a clinical plan is typically in the order of minutes, making it clinically infeasible to use these methods directly for integrated catheter placement optimisation. Different categories of previous approaches are proposed for catheter optimisation for HDR-BT [41]. Several approaches using constraints on the number of catheters optimise the dwell times and positions simultaneously while having restrictions on the number of catheters used [36], [42], [43]. All three approaches have run times up to hours, making them clinically infeasible. Several other approaches are based on geometric coverage optimisation, e.g., by assuming constant dwell times for each dwell position [13], [44], [45]. However, geometric optimisation might be less appropriate due to the complicated shape of the target region and the proximity to the OARs in cervical cancer. Another category of approaches uses an iterative strategy, where catheters that contribute the least to the objective are iteratively removed [31], [46], or a combination of addition and removal of catheters based on contribution to the objective [47]. The problem with iterative optimisations based on needle contribution is that after deleting more needles, previously removed needles must be reconsidered because now these needles might contribute significantly.

In this work, besides dwell time optimisation and catheter placement optimisation, source channels are also planned. In the previous works that have performed partially automated planning of curved source channels in HDR-BT applicators, RRT and its variants are often used [48] - [50]. The approaches are visualised in Figure 3.1 and will be discussed below.

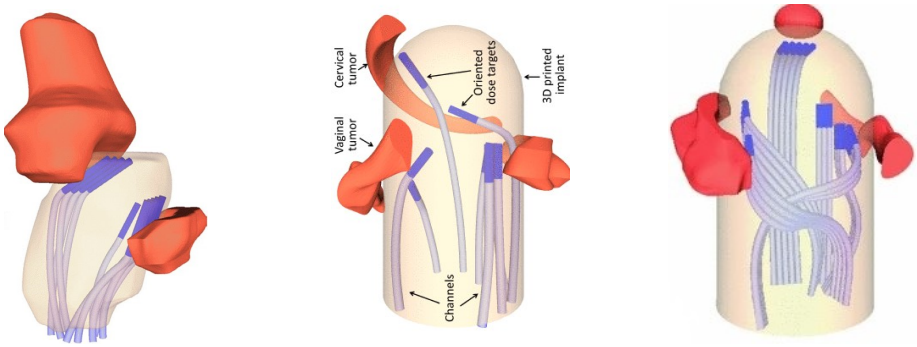

(a) Garg et al. [48]. (b) Duan et al. [49]. (c) Patil et al. [50].

Figure 3.1: Visualisation of the different path planning methods in HDR-BT.

The first method by Garg et al. is a channel layout method that computes a set of non-intersecting curvature-constrained channels within the implant that reach the dwell positions proximal to the tumour [48]. This method uses RRTs to find collision-free curvature-constrained paths from the a priori-defined dwell positions back to the entry region of the applicator. The method starts with the dwell segment most distant from the entry region, and after a feasible path is found, this is added as an obstacle while finding the paths from the following dwell segments.

The second method by Duan et al. computes mutually collision-free curvature-constrained channels within the implant [49]. The path optimisation (TrajOpt) is performed by leveraging randomly perturbed variations of a previously discovered path. Opposed to single-channel optimisation, the authors also tried multi-channel optimisation. The method aims to minimise a cost function that includes the total twist of the needle path, the path length, and the distance between the paths and obstacles. The authors have demonstrated that this method yields high-quality channel layouts with a higher planning success rate while maintaining comparable computation times to the method proposed by Garg et al. [48]. The limitations of this approach are that it can only guarantee local optimality and has high running times. Moreover, due to the randomness of the optimisation, it is dependent on the seed path for optimisation.

The third method by Patil et al. proposes a method that computes multiple collision-free curvature- and torsion-constrained ribbons (group of channels) [50]. The ribbons are traced out by sweeping a constant-width rigid body along spatial curves. The method has a two-stage approach. In the first stage, an RRT-based planner plans curvature and torsion-constrained feasible ribbons. In the second stage, the curvature and torsion of these ribbons are locally optimised using sequential quadratic programming. The limitations of this approach are: i) it can only reach local optimality, ii) it has high running times, iii) in narrow passages, the RRT-based planner is not guaranteed to find a feasible path, and iv) if the RRT planner finds solutions in the same homotopy class, the local optimisation finds a sub-optimal solution (see Figure 3.2).

In all papers mentioned above, the dwell segments are manually specified. A method that optimises the dwell segments to get the optimal dose distribution whilst considering the feasible dwell segments within the applicator is desired. Furthermore, all papers above only plan paths for IC channels. For the curative treatment of locally advanced cervical cancer, IS needles are needed and should, therefore, also be included in the planning.

(a) Example of two paths from the same homotopy class.

(b) Example of two paths from different homotopy classes.

Figure 3.2: Two functions are called homotopic if they can be continuously deformed into each other. Two paths are from the same homotopy class if they are homotopic. A visualisation is shown in this Figure. A visualisation of paths from the same homotopy (a) and different homotopy classes (b) is shown. Images obtained from [51].

Another previously proposed approach to automate source channel planning used minimum curvature Bézier curve trajectory optimisation for each candidate channel in the first stage [9]. The Bézier curve formulation enabled the use of fast quadratic programming [52]. Feasible configurations were selected with geometric coverage optimisation in the next stage. Therefore, the quality of the returned solutions is dependent on the candidate set and promising needle candidates may be discarded instead of re-optimising the configuration around these. Simultaneous optimisation of channels may circumvent these issues. The method made use of a brute force line-segment collision check.

3.2. COVER PROBLEMS

In this work, a weighted set cover formulation is used to solve the coverage problem. There are already some approaches in HDR-BT or similar fields that perform treatment optimisation using cover problem formulations.

In implant optimisation in HDR-BT, straight needles are used. Analogously, in other EBRT variants, such as Intensity Modulated Radiation Therapy (IMRT), straight beams are used. Some ablation therapy variations, a form of tumour therapy, such as radio-frequency ablation therapy (RFAT) [53], use straight needles.

The approaches in similar fields are shown in Table 3.1. In the table, the methods are listed, including the coverage problem formulation that is used and the medical field in which it is used. Furthermore, the objective of the approach and how the optimisation is solved are listed. Extra steps to make the optimisation possible or to speed up the optimisation are also listed. Lastly, if the method uses inter-needle collision checking and if the method uses co-planar geometry, basically reducing it into a 2D problem, is stated.

Table 3.1: Coverage methods in radiation and ablation therapy.

Approach	Mathematical formulation	Field	Objective	Solving method	Extra steps taken in the approach	Collision Checking	Non planar geometry
Acosta et al. [54]	WSCP	IMRT	Maximise voxel coverage	Solving ILP (using CPLEX v6.6)	Sample beam options	×	✓
Ehrgott et al. [55]	WSCP	IMRT	Maximise voxel coverage	Solving ILP (using CPLEX v6.6)	Sample beam options	×	×
Haas et al. [56]	WSCP	IMRT	Pareto ranking of weighted linear penalty function	Genetic algorithm	Initialisation of penalty weights	×	×
Ehrgott et al. [57]	WSCP	IMRT	Conformity to desired dose volumetric constraints	Local search	Sample beam options	×	×
Djajaputra et al. [58]	MKCP	IMRT	Conformity to desired dose volumetric constraints	Simulated annealing	Sample beam options	×	×
Lee et al. [59]	MSCP (weighted)	IMRT	Maximise voxel coverage + OAR sparing	Greedy + post-processing using LS	Sample beam options + select covering threshold	×	✓
Siauw et al. [44]	SCP	HDR-BT	Minimise number of needles	Solving ILP (using CPLEX v12.1)	Define entry region select covering threshold	✓	✓
Aleman et al. [60]	WSCP	IMRT	Maximise voxel coverage	Greedy	Make non-dominated adjacency matrix	×	✓
Liang et al. [61]	WSCP	RFAT	Minimise number of needles + OAR sparing + trajectory optimisation	solving ILP (using GAMS CPLEX)	Sample needle options + Set penalty weights + solve surface coverage	✓	✓
Yu et al. [62]	WSCP	RFAT	Maximise distance to OAR + minimise insertion depth + maximise insertion angle	Genetic algorithm	Set penalty weights + number of needles can increase	×	✓
Kulkarni-Thaker et al. [63]	WSCP	RFAT	Minimise OAR coverage	solving ILP	Only consider boundary voxels + iteratively add constraints	✓	✓
Altobelli et al. [64]	VCP	IMRT	Maximise voxel coverage minimise OAR damage	-	Create directed bipartite graph	×	✓

4 PAPER

LOGO GENERIC COLORIZED JOURNAL, VOL. XX, NO. XX, XXXX 2017 1

AUTOMATED IMPLANT CONFIGURATION OPTIMISATION INCLUDING SIMULTANEOUS SOURCE CHANNEL PLANNING FOR HIGH DOSE RATE BRACHYTHERAPY

R. Dirks, R. Straathof, J. Alonso-Mora, L. Rossi

***Abstract*— Patient-tailored brachytherapy applicators designed for the curative treatment of cervical cancer have the potential to enhance the delivered dose to the tumour while minimising tissue damage of surrounding organs. This work presents a novel three-stage approach to optimise channel configurations in patient-tailored applicators. First, the automated treatment planning algorithm BiCycle is adapted to identify a set of high-potential dwell positions from a grid. Next, a weighted set cover problem is solved iteratively based on the high-potential dwell points to select straight needle segments from a candidate set. Feasibility of this selection is checked and the selection is updated based on the ability of a simultaneous path planning algorithm to plan minimum curvature mutually collision-free source channels in the applicator. Treatment plans are generated with BiCycle for the clinically used, grid and patient-tailored configurations for the first fraction of 22 locally advanced cervical cancer patients. The proposed method and the grid configuration were demonstrated to be clinically feasible according to EMBRACE II aims. Furthermore, the grid configuration obtained a significantly larger target volume dose with a significantly lower bladder, rectum, sigmoid and bowel dose compared to the clinically used configuration. The proposed method found a similar dose in the target volumes and a significantly lower dose for the bladder, rectum and bowel compared to the clinically used configurations. The proposed approach can generate patient-tailored applicators for locally advanced cervical cancer brachytherapy with dosimetric advantages over the clinically used configuration.**

***Index Terms*— Cervical cancer brachytherapy, Implant configuration optimisation, Patient-tailored, Simultaneous path planning, Bézier curves**

I. Introduction

Cervical cancer ranks as the fourth most frequently diagnosed cancer and the fourth leading cause of cancer death in women [1]. Due to this form of cancer, an estimated 342,000 deaths occurred worldwide in 2020 [2]. High-dose-rate (HDR) brachytherapy (BT) is an important part of the curative treatment of locally advanced cervical cancer and is often used as a boost to external beam radiation therapy (EBRT) [3].

Target coverage and local control with conventional applicators remain sub-optimal for large or complex tumours [4]. This leads to frequent side effects and reduces the quality of life [5]. Due to recent developments, applicators can now be patient-tailored. This has the following foreseen benefits: i) increased target coverage and absorbed dose to the target volume with reduced or equal trauma to the surrounding tissues and organs at risk (OARs), ii) improved needle guidance and minimisation of the required number of needles and iii) reliable and comfortable placement [6]. An example of a patient-tailored applicator is the ARCHITECT applicator, which contains optimised source channels. The vaginal vault, the clinical target volumes, and the OARs are segmented on MR images. The outer shape of the ARCHITECT applicator is based on the shape of the vaginal cavity. After shape and source channel determination, the applicator is 3D printed [7].

Treatment planning for conventional applicators concerned dwell time modifications and was performed manually, a trial and error process dependent on time and skills of the treating physician [8]. Several automated dwell time optimisation approaches have been proposed, which demonstrate superiority over manually generated plans [9] - [11]. With the increased flexibility of source positioning due to patient-tailored applicators, manual planning will become increasingly complex, substantially increasing the need for automated needle and dwell position planning.

The source channel planning for the ARCHITECT applicator consists of planning paths from the entry region of the applicator to the desired needle segments. The planned needle channels should i) be mutually collision-free, ii) be contained in the applicator, iii) avoid collision with the intrauterine (IU) tandem, and iv) avoid OAR perforation. To ensure smooth insertion of the needles, the curvature of the source channels in the applicator is limited and to be minimised [12]. Furthermore, clinicians can impose additional constraints based on their preferences. Figure 1 shows a visualisation of these constraints.

This project was supported by a grant from the Dutch Research Council (NWO), Dutch Cancer Society (KWF) and Top Sector Life Sciences & Health (LSH) (Project No. 17921).

Dirks R. and Alonso-Mora J. are with the Delft University of Technology, Department of Cognitive Robotics, Delft, the Netherlands

Straathof R. is with the Delft University of Technology, Department of BioMechanical Engineering, Delft, the Netherlands

Rossi, L is with the Erasmus MC Cancer Institute, University Medical Centre Rotterdam, Department of Radiotherapy, the Netherlands

This study aims to combine dwell time optimisation and source channel planning for interstitial needles without resorting to fully geometric coverage planning. This work proposes a three-stage approach. First, a high-potential set of dwell positions is obtained by running a modified version of the dwell time optimisation software BiCycle (Erasmus Medical Centre, Rotterdam, the Netherlands) on a grid of possible dwell positions [9]. This results in a resolution optimal treatment plan when not considering geometry and applicator constraints. The positions with the highest dwell times according to the resolution optimal treatment plan are selected in the high-potential set. Next, a set cover problem is used iteratively to find a combination of feasible needles to cover all dwell points in the high-quality set at a minimum distance. Lastly, needle channels to the applicator's entry region are simultaneously optimised to be of minimum curvature and mutually collision-free. Channel centrelines are represented by Bézier curves, which enables fast collision checking to be used. The proposed method and the grid configuration are validated based on virtual treatment plans in a representative patient cohort.

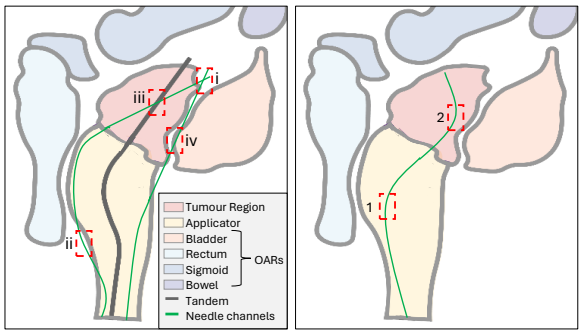

Fig. 1. Visualisation of the different constraints on the needles channels (left) and the curvature constraints/goals (right) in a sagittal view. The different constraints are that the needle channels should i) be mutually collision-free, ii) be contained inside the applicator, iii) avoid collision with the IU tandem and iv) avoid OAR perforation. The curvature constraints limit the curvature of the source channels in the applicator (1) and allow no curvature outside the applicator (2).

A. Related work

The approach in this paper combines treatment planning and catheter placement for HDR-BT. Previously proposed approaches for catheter optimisation in HDR-BT can be categorised [13]. Several approaches using constraints on the number of catheters optimise the dwell times and positions simultaneously while having restrictions on the number of catheters used [14] - [16]. These approaches have run times up to hours, making them clinically infeasible. Several other approaches are based on geometric coverage optimisation, e.g., by assuming constant dwell times for each dwell position [8], [17], [18]. However, geometric optimisation might be less appropriate due to the complicated shape of the target region and the proximity to the OARs in cervical cancer. Another category of approaches uses an iterative strategy, where catheters that contribute the least to the objective are iteratively removed [19], [20], or a combination of addition and removal of catheters based on contribution to the objective [21]. The problem with iterative optimisations based on needle contribution is that after deleting more needles, previously removed needles must be reconsidered because now these needles might contribute significantly.

In this work, geometric coverage planning is extended to take treatment planning into account using a weighted set cover problem formulation. Geometric coverage has been used in similar fields, namely intensity-modulated radiation therapy (IMRT) and radio-frequency ablation therapy (RFAT). In IMRT, the weighted set cover formulation has often been used to maximise the voxel coverage [22] - [25]. The weighted set cover formulation has also been used to optimise a weighted linear penalty function [26], or the conformity to the desired dose volumetric constraints [27]. In RFAT, the weighted set cover formulation is used to minimise the number of needles [28], maximise the distance to the OARs [29], or minimise the OARs coverage [30].

With regards to HDR-BT, an unweighted version of this formulation is used [17], and a related max-k cover formulation is used in our previous work [31]. Whereas these approaches solely rely on geometry, the proposed method in this work generates and selects a candidate set based on the high-potential dwell points returned by treatment planning optimisation.

Partially automated planning of curved source channels in HDR-BT applicators approaches have used RRT, trajectory optimisation, or a combination thereof [32] - [34]. In these approaches, the desired dwell positions are manually specified, and simultaneous optimisation of source channels is not possible in clinically feasible time.

The automated source channel planning workflow proposed in our previous work uses minimum curvature Bézier curve trajectory optimisation for each candidate channel in the first stage [31]. Bézier curve trajectory planning has also been considered for UAVs [35], [36], and for autonomous vehicles [37], [38]. The Bézier curve formulation enables the use of fast quadratic programming [39]. Feasible configurations are selected with geometric coverage optimisation in the next stage. Therefore, the quality of the returned solutions is dependent on the candidate set and promising needle candidates may be discarded instead of re-optimising the configuration around these. Simultaneous optimisation of channels may circumvent these issues. As this requires fast collision checking, culling methods and warm starting are used in this work to improve computational efficiency [40].

II. METHOD

A. General Overview

An overall overview of the workflow in this paper is presented in Figure 2, with subsequent sections providing a more detailed explanation of every step of this process. The algorithm is implemented in MATLAB 2021b on one of the computing clusters of the Erasmus Medical Centre [41]. The used cluster consists of two 8-core 2.90 GHz Intel Xeon E50-2690 CPUs.

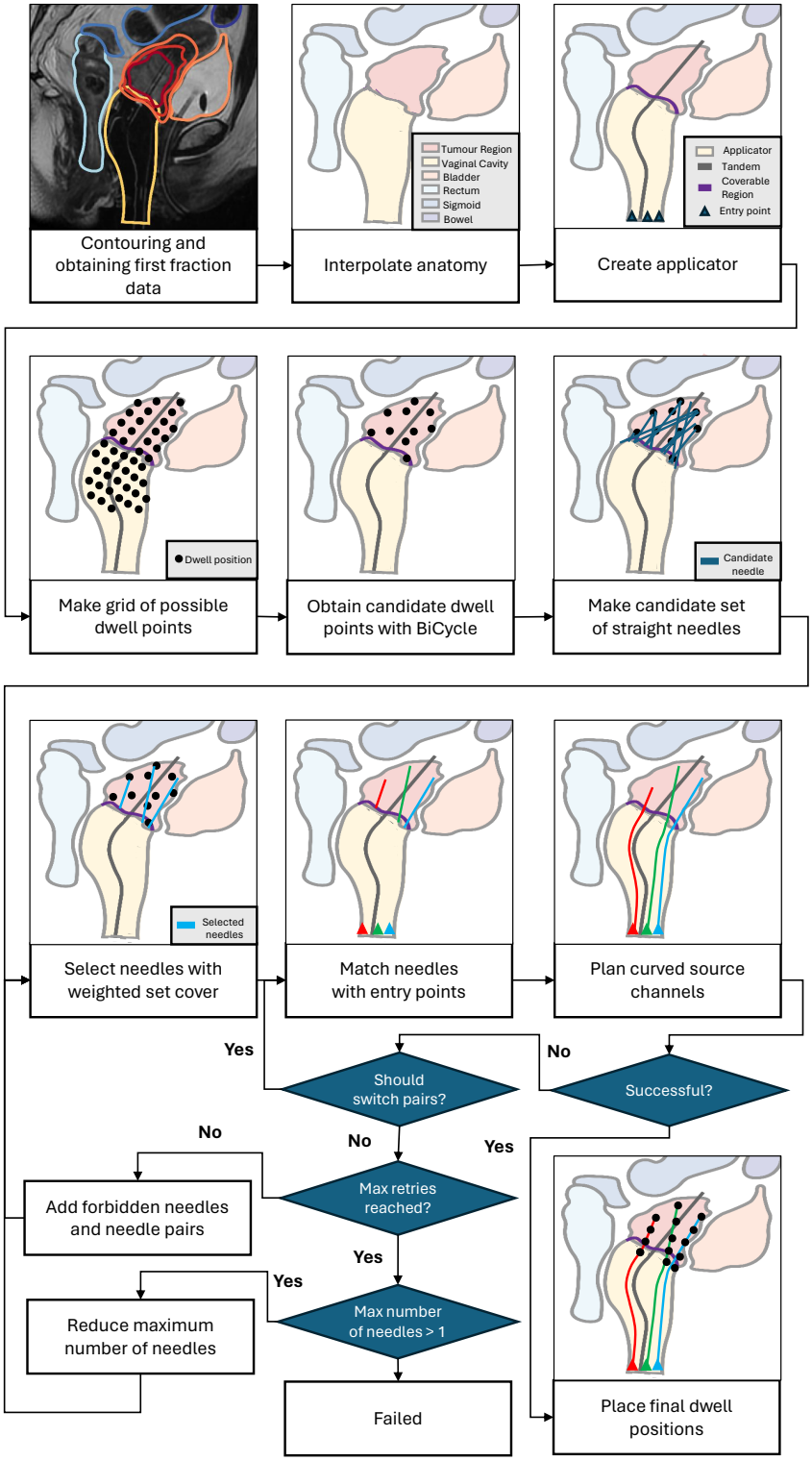

Fig. 2. Overview of the workflow proposed in the paper to optimise the patient-tailored applicator geometry (see text for further explanation).

1) Interpolate Anatomy: Contours of the regions of interest, target volumes, OARs, and vaginal cavity, are drawn on axial MR slices. The first step in the process is contour interpolation of the segmentations to obtain triangular meshes of the relevant structures [31].

2) Create Applicator: The geometry of the applicator is determined based on the triangular mesh of the vaginal cavity. The ARCHITECT applicator consists of two 3D-printed halves connected to the IU tandem structure. In this work, needles are assumed to be able to cross from one half to another. The top part of the applicator is connected to a standardised circular entry region with a diameter of 25 mm by a swept tapered section. The entry region of the ARCHITECT applicator is the part where the clinician inserts the needles. The feasible entry points for the needles are standardised and do not collide with the IU tandem structure.

In the applicator, the structures connecting to the IU tandem are added. The collision space of the tandem structure is also added, this is done by creating an offset of the outer geometry by a distance equating the channel lumen radius (= 1.4 mm) plus the wall thickness of the 3D print (= 1 mm) [31]. The feasible planning space for the source channels consists of the applicator volume minus the collision space.

Based on the applicator shape, the coverable region of the applicator is determined. The coverable region consists of possible applicator-exit points for the needles. All vertex points on the surface of the applicator with an outward normal deviating less than $\Delta\theta_{\text{tandem}}$ (= 20°) from the tandem direction are added to this coverable region. All vertex points that have an outward normal deviating less than $\Delta\theta_{\text{midpoint}}$ (= 80°) from the vector pointing to the centre of mass of the CTV_{HR} are also added to the coverable region.

3) GridBiCycle: To obtain the high-potential dwell positions, BiCycle is used on a grid of possible dwell positions. This grid is established with a step size of 10 mm, both perpendicular and parallel to the IU tandem direction. The grid points are filtered to ensure all grid points lie within the offset of the target regions and the vaginal cavity. A modified version of BiCycle with an adapted wishlist is started on the filtered grid points to obtain a set of dwell times indicating the relative importance of each position. The wishlist adheres to the EMBRACE II aims and considers dose to the CTV_{HR}, CTV_{IR}, the OARs (bladder, rectum, sigmoid and bowel) and different dose points. The relative contributions of the needles, taken into account in the clinical version of the BiCycle wishlist, are not considered. The result of the BiCycle run on the grid configuration is used to select dwell points. All dwell points outside the vaginal cavity are considered for interstitial (IS) needle optimisation. The D_{max} (empirically determined to be 35) points with the highest dwell times are chosen and referred to as candidate dwell points.

4) Make candidate needle set: The candidate needle set contains straight interstitial needles created using three types of sampling: i) in the tandem direction, ii) shortest distance, and iii) based on sets of candidate dwell positions. The tandem direction needles are created from every candidate dwell point to the coverable region in the direction of the tandem. The shortest distance needles are created from every candidate dwell point to the closest point in the coverable region. The set needles combine candidate dwell points. A line is fitted through all dwell points in the set, forcing it to go through the closest point in the coverable region. The line fitting is done in matrix form: Let the dwell positions in the group be $x_1, ..., x_n$. The eigenvector u of covariance matrix $M = \frac{1}{n}\sum_{i=1}^{n} x_{i,new}\ x_{i,new}^T$, where $\overline{x}$ denotes the mean is the direction vector of the needle: $\overline{x} + tu : t \in \mathbb{R}$. The endpoint of the needle is determined based on the projection of the furthest dwell point in the group on the line, plus the distance to the needle tip (= 5 mm).

Only needle segments meeting all constraints are added to the candidate set, the other needle segments are discarded directly. The primary constraint involves avoiding collision with the IU tandem. This is ensured by maintaining a minimum distance between the needle and the IU tandem. To avoid OAR perforation, a safe operational distance (= 10 mm) from the needle tip to OARs is maintained, and the distance in the radial direction should also be larger than 5 mm. Lastly, if a needle is inserted at an excessively steep angle relative to the outward normal of the tissue, there is a risk of the needle sliding along the tissue surface rather than penetrating it. Such deviations lead to imprecise needle placement and thus, must be prevented. Therefore, the angle between the needle and the inward tissue normal is constrained to be below 30^o.

5) Select needles: The set of needle segments to cover all candidate dwell points is selected from the candidate set by making use of a weighted set cover problem (WSCP). In our problem formulation of the weighted set cover problem $U = 1, 2, ..., n$ is a ground set of n high-potential dwell points. $\mathbb{S}$ is the candidate set of m candidate needle segments of U, $|\mathbb{S}| = m$. A cover C is a collection of sets $C \subset \mathbb{S}$ whose union is U. Each $s \in \mathbb{S}$ has a cost c_s. The goal is to find a cover of maximum cost.

$$\text{maximise} \quad \sum_{s=1}^{m} c_s x_s \qquad \text{(WSCP)} \tag{1a}$$

$$\text{subject to} \quad \sum_{s:e\in\mathbb{S}} A_{s,j} \geq 1 \quad \text{for all} \quad j \in U \tag{1b}$$

$$x_s \in \{0, 1\} \quad \text{for all} \quad s \in \mathbb{S} \tag{1c}$$

$$x_y + x_z \leq 1 \quad \text{for all} \quad (y, z) \in \mathbb{B} \tag{1d}$$

$$\sum_{s=1}^{m} x_s \leq N_{max} \tag{1e}$$

In this formulation, x_s denotes if needle s has been selected and $A_{s,j}$ denotes if dwell point j has been covered by needle s. Constraint (1b) ensures that all dwell points are covered by at least one needle. A needle covers a dwell point if its distance to the dwell point is lower than the cover distance d_c. As the needles need to be mutually collision-free, constraint (1d) prevents collision pairs from being selected, as distinguished by the pairwise validity matrix $\mathbb{B}$. Constraint (1e) limits the number of needles to be selected to N_{max}.

Needles are scored based on the inverse squared distance to the dwell positions covered by the needle, and weighted by the corresponding dwell time in the BiCycle plan on the grid

configuration. The cost of a needle, c_s, is thus given by:

$$c_s = -\sum_{j \in J} A_{s,j} d_{s,j}^2 t_j \tag{2}$$

Here, $d_{s,j}$ is the distance from dwell point j to needle s, t_j is the dwell time of the high-potential dwell point j according to the BiCycle treatment plan. To minimise the needles and prevent distances to dwell points counting in multiple selected needles, the cover distance is iteratively increased until a feasible solution to the set cover problem is found. The covering indices A and needle scores are recalculated in every iteration. The process is also described in Algorithm 1. The weighted set cover problem is solved using Gurobi (Beaverton, Oregon, USA) [42].

Algorithm 1: Pseudocode of the needle selection algorithm

Function `SelectNeedles`(*candidateSet*, N_{max}, $d_{c,initial}$, $\mathbb{B}$, *dwellPoints*) **:**
  $d_c \leftarrow d_{c,\text{initial}}$;
  selectedNeedles $\leftarrow \emptyset$;
  while *selectedNeedles is* $\emptyset$ **do**
    $A \leftarrow$ `GetCoveringIndices`(*candidateSet*, *dwellPoints*, d_c);
    $c \leftarrow$ `ScoreNeedles`(*candidateSet*, *dwellPoints*, A);
    selectedNeedles $\leftarrow$ `SelectOptimalSet`(c, A, N_{max}, $\mathbb{B}$,*candidateSet*);
    if *selectedNeedles is* $\emptyset$ **then**
      $d_c \leftarrow d_c + 1$;
    end
  end
  return *selectedNeedles*, d_c;

6) Path planner: From the selected needle segments channel paths need to be planned back to the entry region.

Needle segments and entry points are matched considering that their respective channel should have minimum curvature and need to be mutually collision-free. First, a matching plane is defined, and the needle segments are projected in their direction onto this plane. The Hungarian method is used to reduce the overall squared distance from the projected needle points and the matched projected entry points [43]. The height of this plane is an important factor in determining the trade-off between channel curvature and collisions and is empirically determined to be in the middle of the entry region and applicator top plane.

As the needle segments are now placed and matched to an entry point, the channels from these needle segments to the entry region points need to be planned. Needles are enforced to enter the applicator in a direction perpendicular to the entry plane. The proposed method uses Bézier curves to represent the needle channels' centrelines. The total curvature of all channels is minimised based on an approximate expression for the bending energy of a Bézier curve [44]. The cost function J for minimising the kth derivative of a Bézier curve can be written in the following way:

$$J = \sum_{\mu \in [x,y,z]} \int_0^T \left(\frac{d^k f_\mu(t)}{dt^k}\right) dt \tag{3}$$

By using the Bernstein property, this problem can be rewritten into a quadratic problem, $P^T Q_0 P$, where P contains all three dimensions of the control points in a single column and Q_0 is the Hessian of the objective [39]. This Hessian can be precomputed based on the order of the derivative and the order of the Bézier curve, which makes the curvature minimisation computationally efficient. Fixed end directions of the channels are added as equality constraints, forcing the channel to be perpendicular to the entry region and in the direction of the needle segment on the other end.

The planned paths also need to be mutually collision-free. This can be checked by making use of the convex hull property [45], which results in overly conservative bounds [46], [47]. Another option is to use a point-per-point evaluation, which is slow and might suffer from the tunnelling effect. Hence, a method with a converging lower and upper bound on the distance between two Bézier curves is used [40]. The upper bound is determined by the minimum distance of the start and end points of the Bézier curves. The lower bound is determined by the distance between the two bounding boxes with the use of a GJK algorithm [48]. If the relative difference between the bounds is larger than the predefined tolerance (= 0.1), the Bézier curves are split using De Casteljau's algorithm and the process is repeated until the lower and upper bounds are within the tolerance [49]. The IU tandem shape is approximated by two Bézier curve sections with different diameters (thick section = 8 mm, thin section = 6 mm) to check for collisions with the converging collision checking method.

Simultaneous optimisation of multiple collision-constrained channels is performed via the workflow in Figure 2 using the MATLAB optimisation routine fmincon. For the sake of computational efficiency, path planning without consideration of collision constraints is used as initialisation. The paths are then optimised considering the aforementioned collision constraints and subsequently undergo verification through a brute force straight-line collision assessment. If all paths clear this verification step without any detected collisions the paths are approved. Conversely, if collisions are identified in instances where the rapid collision assessment failed to detect any, a more meticulous straight-line collision optimisation process is initiated. Should collisions persist after this optimisation, the entry points of the conflicting needle pairs are switched and the path planning process is restarted. If the algorithm fails to find a feasible solution using these needles after N (= 3) restarts, more retries with the same needles are unlikely to lead to a feasible solution. Hence, the number of restarts is limited to N restarts. If no feasible source channels are found, even after these restarts, a new set of needles is selected. In this set, needle pairs that have previously been in collision are not allowed to both be selected. Needles that have been in collision with the IU tandem are removed from the candidate set. If multiple collisions occur after the restarts, the maximum number of needles is reduced. The pseudocode of this process

is presented in Algorithm 2.

Algorithm 2: Algorithm to find feasible source channels using a candidate set

Function `CreateARCHITECT` (*dwellPoints, $N_{max,initial}$, $d_{c,initial}$, applicator, anatomy*) **:**
  (*candidateSet*,$\mathbb{B}$) ← `CreateCandidateSet` (*dwellPoints*, *applicator*, *anatomy*);
  $N_{\text{max}} \leftarrow N_{\text{max,initial}}$;
  paths ← $\emptyset$;
  $d_c \leftarrow d_{c,\text{initial}}$;
  while *paths is* $\emptyset$ ***and*** $N_{max} \geq 1$ **do**
    (*selectedNeedles*, d_c) ← `SelectNeedles` (*candidateSet, N_{max}, d_c, $\mathbb{B}$, dwellPoints*)
    (*paths*, *collisions*, $N_{\text{collisions}}$) ← `FindPaths` (*selectedNeedles, applicator*) ;
    if *paths is* $\emptyset$ **then**
      (*candidateSet*,$\mathbb{B}$) ← `UpdateCandidateSet` (*candidateSet, $\mathbb{B}$, collisions*) ;
      if $N_{collisions} > 1$ **then**
        $N_{\text{max}} \leftarrow N_{\text{max}}$ - 1;
      end
    end
  end
  return *paths*;

7) Generation of treatment planning configurations: Treatment planning is performed using BiCycle on the grid, clinical and ARCHITECT configurations. For the ARCHITECT configuration, dwell positions are spaced every 5 mm in each needle minimising the distance to the corresponding covering dwell points. Dwell points at least 6 mm below the applicator's top surface are treated as intracavitary dwell positions.

For treatment planning for the clinical and ARCHITECT configuration, the clinical wish list for cervical cancer is used that adheres to the EMBRACE II aims and considers dose to the CTV_{HR}, CTV_{IR}, OARs (bladder, rectum, sigmoid and bowel), and different dose points.

B. Patient Dataset

The patient dataset used in this study is the same as used in our previous work [31]. The first fractions of twenty-two patients with FIGO stage IB3-IV treated between 2021 and 2022 with HDR-BT using the IC/IS Venezia applicator are considered for the virtual planning study. Treatment included EBRT (25 fractions of 1.8 Gy) and MRI-guided BT (3-4 fractions).

C. Patient Evaluation

The evaluation of the treatment planning is done based on the normalised clinically relevant DVH parameters, the total dwell time, the conformity index (COIN = $\frac{V_{100}^{\text{CTV}_{\text{HR}}}}{V^{\text{CTV}_{\text{HR}}}} \cdot \frac{V_{100}^{\text{CTV}_{\text{HR}}}}{V_{100}^{\text{Total}}} \prod(1 - \frac{V_{100}^{o}}{v_o})$ with o denoting the OARs), and the number of needles used. Results for the GTV_{Res} are not shown here as it is not considered in the current wishlist. The normalised dosimetric indices for the target volumes are calculated by dividing the obtained dose by the planning aim dose ($D_{\text{plan}}/D_{\text{aim}}$). For the OARs, the normalised dosimetric indices are calculated by dividing the planning aim dose by the obtained dose ($D_{\text{aim}}/D_{\text{plan}}$). Hence, for all normalised dosimetric indices, a value above 1 depicts that the planning aim has been met, and the higher, the better.

The BiCycle results of the clinically used applicator configuration are used as the benchmark in these comparisons. Therefore, two comparisons are made, one between the clinical configuration and the grid configuration, and one between the clinical configuration and the ARCHITECT configuration. Statistical significance regarding the difference in normalised dosimetric indices and total dwell times is determined with Wilcoxon signed-rank tests. Spearman's rank tests are utilised to evaluate the correlation between the different parameters and the dosimetric indices.

III. Results

The proposed source channel planning algorithm found feasible solutions for all 22 patient cases. The source channels all had acceptable curvatures with a minimum local curvature radius of 40 mm [7]. Figure 6 shows the applicator geometries generated with the proposed method and the clinically used needle configurations. As observed, the proposed method generates configurations with needles in more diverse directions than the clinically used configurations. The number of needles used does not significantly differ between the clinical and the ARCHITECT configurations. The proposed method's average (range) runtime was 28 (18-52) minutes. This runtime includes the runtime of BiCycle on the grid configuration. On average (range), the proposed method tried a new needle combination 5.9 (2 - 12) times.

All generated treatment plans were considered acceptable according to EMBRACE ll aims, as no hard limits were exceeded. The planning aims, however, were not met for all the parameters and patient cases. The number of times planning aims were not met for the different configurations is shown in Table I. As can be observed from this table, in comparison with the clinical configuration, planning aims were met more often with the grid configuration, ensuring that the planning aims were met for all target volumes. The generated plans for the ARCHITECT configuration also met planning aims more often than those generated for the clinical configuration.

TABLE I
TABLE SHOWING THE NUMBER OF TIMES THE PLANNING AIMS WERE NOT MET FOR THE DIFFERENT CONFIGURATIONS FOR 22 PATIENT CASES.

Structure	Clinical	ARCHITECT	Grid
CTV_{HR} D_{90}	4	0	0
CTV_{HR} D_{98}	2	1	0
CTV_{IR} D_{98}	5	0	0
Bladder $D_{2\text{cm}^3}$	12	7	3
Rectum $D_{2\text{cm}^3}$	4	3	2
Sigmoid $D_{2\text{cm}^3}$	5	3	1
Bowel $D_{2\text{cm}^3}$	0	0	0

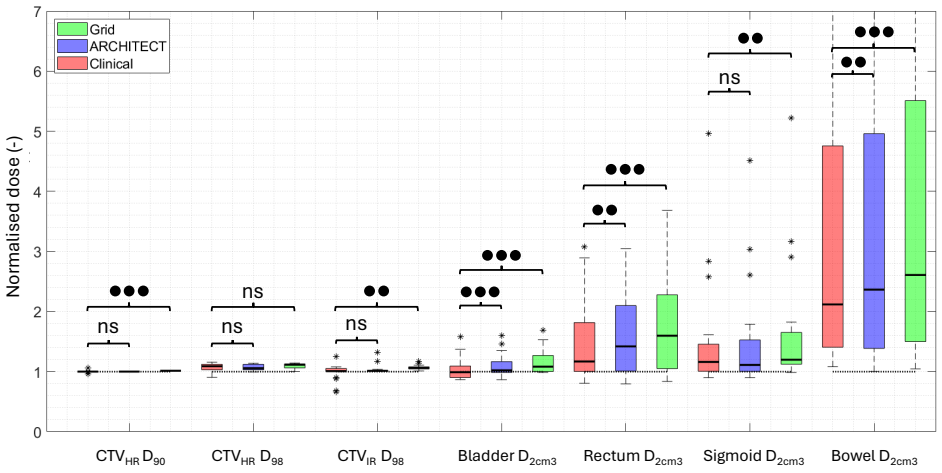

Fig. 3. Box plots showing normalised doses from treatment plans generated with clinical, ARCHITECT and grid configurations for selected DVH parameters. The black line indicates the median, the boxes indicate the interquartile ranges, the whiskers indicate the extrema without outliers, and the asterisks are the outliers. Significance levels are indicated with the black filled circles (● = $p < 0.05$, ●● = $p < 0.01$, ●●● = $p < 0.001$) and ns denotes no significant differences are found.

Figure 3 shows the normalised dose for the different relevant planning aims for the three configurations. The normalised CTV$_{HR}$ D$_{90}$ dose for the clinical and ARCHITECT configurations were comparable. There was a significant but marginal increase ($p < 0.001$) in normalised (median; IQR) CTV$_{HR}$ D$_{90}$ dose for the grid configuration (1.01; 1.01-1.02) with respect to the clinical configuration (1.00; 1.00-1.00). The normalised CTV$_{IR}$ D$_{98}$ dose for the clinical and ARCHITECT configurations were comparable. However, with the grid configuration (1.06; 1.05-1.08) there was a significant increase ($p < 0.01$) compared to the clinical configuration (1.01; 1.00-1.05). There were no significant changes in the CTV$_{HR}$ D$_{98}$ doses for the different configurations.

The normalised bladder D$_{2cm^3}$ doses (median; IQR) with the grid (1.08; 1.00-1.27) and the ARCHITECT (1.02; 0.99-1.17) configuration were significantly higher ($p < 0.001$) compared to the clinical configuration (0.99; 0.90-1.09). Similarly, the normalised rectum D$_{2cm^3}$ doses (median; IQR) with the grid (1.6; 1.05-2.28) and ARCHITECT (1.42; 1.01-2.1) configuration were significantly higher ($p < 0.01$) with respect to the clinical configuration (1.17; 1.00-1.82). The normalised (IQR) sigmoid D$_{2cm^3}$ dose significantly increased ($p < 0.01$) from 1.16 (1.01-1.46) with the clinical configuration to 1.20 (1.12-1.65) with the grid configuration. Moreover, for the normalised (IQR) bowel D$_{2cm^3}$ dose, there was a significant increase ($p < 0.01$) from 2.12 (1.14-4.76) with the clinical configuration to 2.61 (1.5-4.51) with the grid configuration. With the ARCHITECT configuration, the median normalised (IQR) bowel D$_{2cm^3}$ dose increased significantly ($p < 0.01$) to 2.36 (1.39-4.96) from 2.12 (1.41-4.76) with the clinical configuration. There was no significant difference between the clinical and ARCHITECT configurations regarding normalised dose for the sigmoid D$_{2cm^3}$.

The median (range) conformity index increased significantly ($p < 0.05$) from 0.63 (0.37-0.88) with the clinical configuration to 0.78 (0.52-0.87) with the grid configuration and 0.78 (0.44-0.85) with the ARCHITECT configuration. Furthermore, with the use of the grid and ARCHITECT configuration, the median (IQR) total dwell time decreased significantly ($p < 0.01$) from 339 (314-397) to 299 (270-319) and 300 (263-363) seconds, respectively.

Figure 4 shows the differences in fraction doses for the clinical and the grid configuration per patient per dosimetric index. In the figure, yellow bars indicate that the corresponding treatment plan did not meet the planning aim, and green blocks indicate that the planning aim was met. For most patients, the grid configuration made better tradeoffs between OAR sparing and target dose. Decreasing the dose for some of the already reached planning aims enabled other aims to be reached. Moreover, in cases where all planning aims were met for both configurations, the grid configuration was often preferable for most dosimetric indices. For example, in patient 8, the CTV$_{HR}$ D$_{90}$ and CTV$_{HR}$ D$_{98}$ doses could be lowered in accordance with the planning aims, such that the D$_{2cm^3}$ dose for all OARs are now meeting the planning aims. The use of the grid configuration also enabled an increase in CTV$_{IR}$ D$_{98}$ dose for this patient, ensuring this planning aim was met as well.

In Figure 5 the differences in fraction doses for the clinical and the ARCHITECT configuration per patient per dosimetric index are shown. As can be seen, better tradeoffs between OAR sparing and target dose could be made for several patients. For example, in patient 8, decreasing the dose in the target volumes also allowed a decrease in the dose in the OARs, ensuring all planning aims were met. Moreover, for some patients, the target and OAR dose could be improved for all dosimetric indices except for a small increase in a single OAR dose. For example, in patient 21, all dosimetric indices obtained with the ARCHITECT configuration were preferable over the clinical configuration, except for a small increase in sigmoid dose. No correlations were found to be significant between the dosimetric indices and the number of needles used for the ARCHITECT configuration.

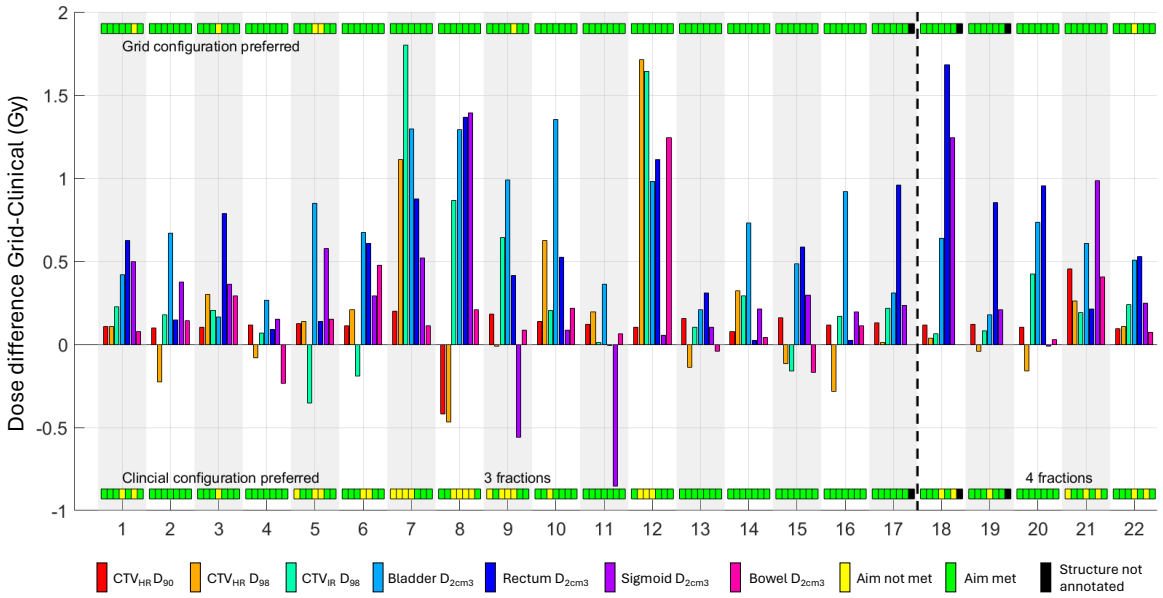

Fig. 4. Bar chart showing the difference between the relevant DVH parameters from the treatment plans obtained with the clinical and the grid configuration. Bars above the x-axis indicate that the grid configuration obtained a preferred dose for that volume, whereas bars below the x-axis indicate that the clinical configuration obtained the preferred dose. Planning aims not being met are indicated by the yellow blocks, and aims being met are indicated by the green blocks. If the structure was not annotated in the structure set, it is indicated by a black box. The patients receiving three fractions are shown on the left of the vertical black dotted line, and the patients receiving four fractions are plotted on the right of this line.

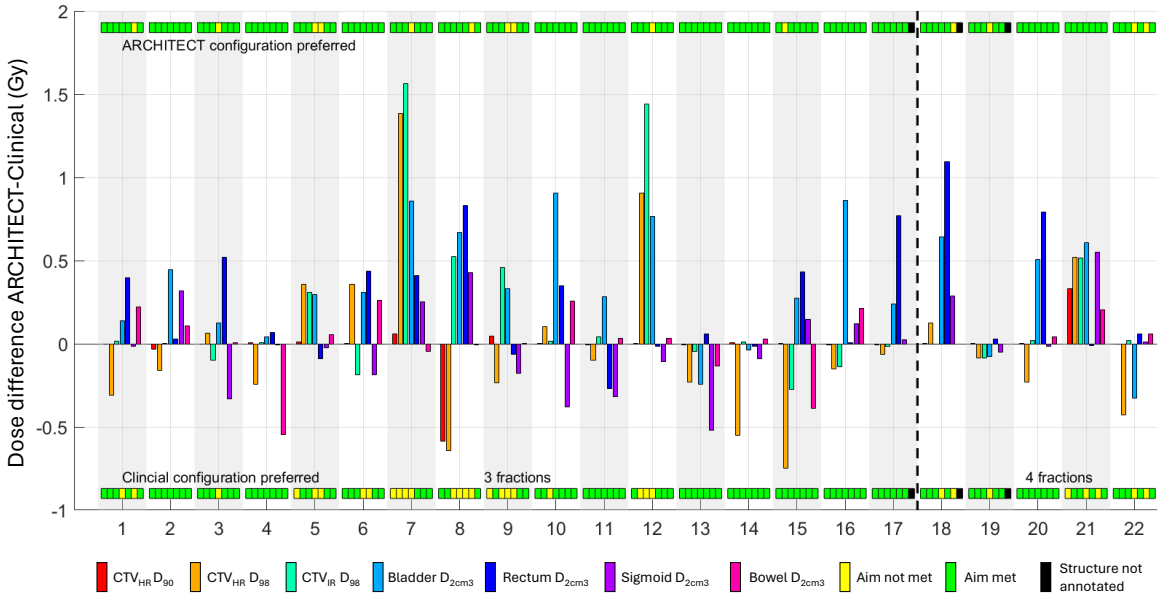

Fig. 5. Bar chart showing the difference between the relevant DVH parameters from the treatment plans obtained with the clinical and the ARCHITECT configuration. Bars above the x-axis indicate that the ARCHITECT configuration obtained a preferred dose for that volume, whereas bars below the x-axis indicate that the clinical configuration obtained the preferred dose. Planning aims not being met are indicated by the yellow blocks, and aims being met are indicated by the green blocks. If the structure was not annotated in the structure set, it is indicated by a black box. The patients receiving three fractions are shown on the left of the vertical black dotted line, and the patients receiving four fractions are plotted on the right of this line.

IV. Discussion

This study proposes and dosimetrically validates an approach to generate a patient-tailored applicator configuration without resorting to full geometric optimisation. A high-quality candidate set is created based on a treatment plan for a grid configuration placed in and around the tumour region. The optimal needle segments are selected with an iterative weighted set cover problem, in which, after each iteration, source channel optimisation is performed to check whether a feasible configuration can be found. The source channels are optimised using iterative simultaneous optimisation with fast convergence-based collision checks. A virtual configuration and planning study in a patient cohort of 22 patients demonstrated that the grid configuration could improve dose conformity for several patients. Similarly, the proposed ARCHITECT configuration could increase the dose conformity for several patients.

The current method to obtain candidate dwell positions uses BiCycle on an equally spaced grid. In this study, the grid resolution and placement are not varied. Research has shown that the step size between dwell positions plays a significant role in the dose conformity for HDR-BT for the prostate [50]. Moreover, the grid spacing and placement also affect the optimisation time and convergence of BiCycle, as, for example, more points lead to a longer optimisation time. In a study (data not shown), the 10 mm grid spacing was found to lead to good biasing of the needles while still leading to reasonable optimisation times. Besides varying the standard grid spacing, random perturbations and a circular pattern might also be beneficial.

The proposed needle selection and source channel planning methods work regardless of the approach used to find the candidate dwell positions. Therefore, other approaches that select dwell positions can also be used to generate the high-quality candidate set. Possible alternatives include GOMEA on a grid [51], a central Voronoi decomposition [18], or a genetic algorithm [52]. Methods resorting to fully geometric coverage planning might be compromised by the complicated shape of the target region and the proximity to the OAR in cervical cancer. Hence, methods not resorting to fully geometric coverage planning, like the approach in this work, might be preferred.

The candidate set used in this work is created based on three types of needles: the shortest, the tandem direction and the group needles. Other needle types create an even more diverse and possibly higher-quality candidate set. Another needle type can, for example, be created by generating straight needle segments with different directions in the tumour region [51] [53]. Moreover, the needles are only added to the candidate set if all constraints are met. If a needle does not meet a constraint, it is not added. The quality of the candidate set can be further improved by not discarding infeasible but promising needles directly. Perturbations of these needles can be generated and, if feasible, added to the candidate set.

Needle segments are matched to entry points based on minimum overall distance on the matching plane before planning the source channel paths. This matching is essential in the tradeoff between collisions and curvature. In sequential multi-robot path planning, the order in which the paths are planned is also essential for the path quality and feasibility [54]. A full search, trying all possible matching combinations [55], is not computationally efficient. Hence, heuristics are often used to obtain an efficient tradeoff [56]. Proposed heuristics for multi-robot path planning are random swapping [57], and starting with the furthest needle [54]. The current work matches entry points and needle segments based on the minimum overall squared distance evaluated on a matching height plane. The heuristic only considers distance and does not consider potential tandem collisions. A different heuristic taking into account potential collisions with the IU tandem structure might be beneficial. Possible approaches could use the minimum energy curves for all possible matching combinations, with a heuristic that increases the cost of needles in collision [58], or increases the score in the case of neighbouring paths [59]. Collisions with the IU tandem can also be prevented by adding repelling points, which increase the energy of nearby paths [44]. Besides changing the matching heuristic, the informed rematching of colliding needles can also be done based on the heuristic [60], instead of switching the colliding needed pairs. Moreover, the need for a matching algorithm can be removed by not constraining the entry points to be at a certain position but only on the entry plane inside the applicator [61]. This, however, will lead to a non-standardised entry region, reducing the clinical ease and increasing the change of channel mixups or needle reconstruction problems.

A weighted set cover formulation is used to select the optimal needle segments from the candidate set. However, the coverage problem can also be solved with other coverage problem formulations. An example of another coverage problem solution would be multiline fitting algorithms like RANSAC [62] or PEaRL [63]. The set cover problem is a generalisation of the RANSAC variations [64]. Another example of a possible coverage problem solution is a clustering method, such as k-means clustering. These methods have been used before in RFAT [65], and in IMRT [66], [67]. In the clustering approach, points would first be clustered, after which one needle per cluster would be fitted.

In the current work, the planned source channels are all planned as IS needles. In conventional applicators, there is an ovoid/ring structure for IC dwell positions. This work removes these structures to create more flexibility for IS needles and possibly increase dose conformity [68], [69]. The function of the ovoid/ring structure is recreated by placing dwell positions at a 6 mm distance from the applicator surface on the source channels. The relative contributions of IC channels and IS needles are not considered in the wishlists in this work. Hence, these contributions are allowed to deviate from Embrace ll aims. Previous research has shown that this can be safely done without having an impact

on the treatment quality [69]. This research suggests that patient-specific IC/IS applicator configurations could lead to superior dosimetric outcomes compared to traditional IC/IS applicators with oblique needles. This adds to the similar indications in previous works, where favourable patient-tailored configurations have been reported in comparison to standard IC/IS applicators [31], [70], [71]. With both the grid and ARCHITECT configurations, the number of planning aim violations was reduced compared to the clinical configuration. Moreover, with the use of the ARCHITECT configuration, a significant decrease in bladder, sigmoid and bowel D_{2cm^3} doses was achieved. Better results might be achieved by better placement of the final dwell positions in the proposed ARCHITECT configuration. These dwell positions are currently spaced at a 5 mm distance, as this is used clinically in the Erasmus Medical Centre. Different dwell spacings could be used, as the obtained dwell sequence influences the cell survival [72].

The proposed method can generate feasible patient-tailored applicators for every patient in the patient cohort within 52 minutes. User actions in the proposed workflow are limited to quality checks, implying this can be implemented in the current clinical workflow. The runtimes mentioned in this work indicate that the method can run in clinically feasible time. The computations can be further sped up by increasing the quality of the candidate set or improving the matching heuristic to reduce the replanning times. The replanning times are already reduced by limiting the number of restarts with the same number of needles. As no correlations were found to be significant between the number of needles used and the dosimetric indices, this approach is justified. Moreover, runtime reduction can also be achieved by further parallelising the computations.

There are several limitations to the method proposed in this work. The focus of this study is to show the clinical feasibility of the method and validate it on a small patient cohort. The current workflow uses the MRI taken during the first fraction with a conventional applicator in situ. Hence, the ARCHITECT applicator can only be used from the second fraction onwards. A pre-BT MRI with a conventional applicator in situ, performed by some institutions [73], enables the usage of the proposed ARCHITECT applicator in the first fraction. Moreover, the clinical configurations used in this work are all based on the first fractions; the dose conformity obtained in the second fraction with the clinical configuration could be better, as in our clinic, the number of needles used in the second fraction onwards often increases. In addition, the current comparison assumes equal dose distributions for all fractions. In practice, these dose distributions might vary between fractions, resulting in better total treatment dose conformity. Lastly, the current virtual planning study is evaluated and compared purely to the resulting DVH parameters. Experienced clinicians should also evaluate the treatment plans.

V. CONCLUSION

This study proposes a method to combine dwell time optimisation and source channel planning for the interstitial needles without resorting to fully geometric coverage planning. The proposed method and the grid configuration are demonstrated to be clinically feasible, and in the resulting treatment plans, the dose conformity could be increased for several patients.

The proposed approach benefits from the high-potential dwell points to generate a high-quality candidate set. Moreover, the method benefits from simultaneous source channel planning combined with iterative replanning, increasing the likelihood of feasible source channels with minimum curvature. The proposed approach can generate patient-tailored applicators for locally advanced cervical cancer BT with dosimetric advantages compared to the clinically used configuration.

APPENDIX I

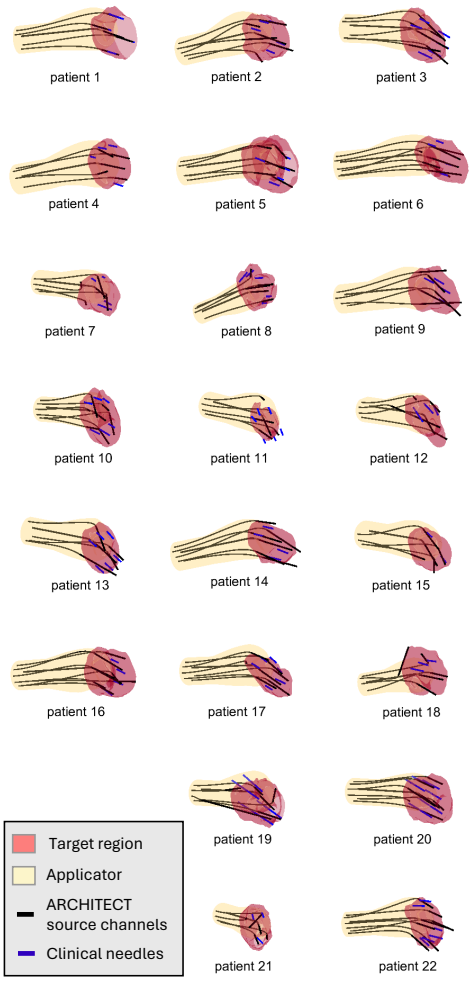

Fig. 6. Overview of patient-tailored applicators generated with the proposed method.

REFERENCES

[1] F. Bray, J. Ferlay, I. Soerjomataram, R. L. Siegel, L. A. Torre, and A. Jemal, "Global cancer statistics 2018: Globocan estimates of incidence and mortality worldwide for 36 cancers in 185 countries," *CA: a cancer journal for clinicians*, vol. 68, pp. 394–424, 11 2018. [Online]. Available: https://pubmed-ncbi-nlm-nih-gov.tudelft.idm.oclc.org/30207593/

[2] H. Sung, J. Ferlay, R. L. Siegel, M. Laversanne, I. Soerjomataram, A. Jemal, and F. Bray, "Global cancer statistics 2020: Globocan estimates of incidence and mortality worldwide for 36 cancers in 185 countries," *CA: A Cancer Journal for Clinicians*, vol. 71, pp. 209–249, 5 2021. [Online]. Available: https://onlinelibrary.wiley.com/doi/full/10.3322/caac.21660

[3] D. Cibula, R. Pötter, F. Planchamp, E. Avall-Lundqvist, D. Fischerova, C. Haie-Meder, C. Köhler, F. Landoni, S. Lax, J. C. Lindegaard, U. Mahantshetty, P. Mathevet, W. G. McCluggage, M. McCormack, R. Naik, R. Nout, S. Pignata, J. Ponce, D. Querleu, F. Raspagliesi, A. Rodolakis, K. Tamussino, P. Wimberger, and M. R. Raspollini, "The european society of gynaecological oncology/european society for radiotherapy and oncology/european society of pathology guidelines for the management of patients with cervical cancer," *Virchows Archiv*, vol. 472, pp. 919–936, 6 2018. [Online]. Available: https://link.springer.com/article/10.1007/s00428-018-2362-9

[4] L. Fokdal, A. Sturdza, R. Mazeron, C. Haie-Meder, L. T. Tan, C. Gillham, B. Šegedin, I. Jürgenliemk-Schultz, C. Kirisits, P. Hoskin, R. Pötter, J. C. Lindegaard, and K. Tanderup, "Image guided adaptive brachytherapy with combined intracavitary and interstitial technique improves the therapeutic ratio in locally advanced cervical cancer: Analysis from the retroembrace study," *Radiotherapy and Oncology*, vol. 120, pp. 434–440, 9 2016.

[5] C. Kirisits, S. Lang, J. Dimopoulos, D. Berger, D. Georg, and R. Pötter, "The vienna applicator for combined intracavitary and interstitial brachytherapy of cervical cancer: design, application, treatment planning, and dosimetric results," *International journal of radiation oncology, biology, physics*, vol. 65, pp. 624–630, 6 2006. [Online]. Available: https://pubmed-ncbi-nlm-nih-gov.tudelft.idm.oclc.org/16690444/

[6] M. Serban, C. Kirisits, A. de Leeuw, R. Pötter, I. Jürgenliemk-Schulz, N. Nesvacil, J. Swamidas, R. Hudej, G. Lowe, T. P. Hellebust, G. Menon, A. Oinam, P. Bownes, B. Oosterveld, M. D. Brabandere, K. Koedooder, A. B. L. Marthinsen, D. Whitney, J. Lindegaard, and K. Tanderup, "Ring versus ovoids and intracavitary versus intracavitary-interstitial applicators in cervical cancer brachytherapy: Results from the embrace i study," *International journal of radiation oncology, biology, physics*, vol. 106, pp. 1052–1062, 4 2020. [Online]. Available: https://pubmed.ncbi.nlm.nih.gov/32007365/

[7] R. C. Laan, R. A. Nout, J. Dankelman, and N. J. van de Berg, "Mri-driven design of customised 3d printed gynaecological brachytherapy applicators with curved needle channels," *3D Printing in Medicine*, vol. 5, 12 2019.

[8] S. Pokharel, S. Rana, J. Blikenstaff, A. Sadeghi, and B. Prestidge, "Evaluation of hybrid inverse planning and optimization (hipo) algorithm for optimization in real-time, high-dose-rate (hdr) brachytherapy for prostate," *Journal of Applied Clinical Medical Physics*, vol. 14, pp. 96–107, 7 2013. [Online]. Available: https://onlinelibrary-wiley-com.tudelft.idm.oclc.org/doi/full/10.1120/jacmp.v14i4.4198

[9] M. Oud, I. K. Kolkman-Deurloo, J. W. Mens, D. Lathouwers, Z. Perkó, B. Heijmen, and S. Breedveld, "Fast and fully-automated multi-criterial treatment planning for adaptive hdr brachytherapy for locally advanced cervical cancer," *Radiotherapy and Oncology*, vol. 148, pp. 143–150, 7 2020.

[10] L. Beaulieu, H. Al-Hallaq, B. S. Rosen, and D. J. Carlson, "Multicriteria optimization in brachytherapy," *International Journal of Radiation Oncology Biology Physics*, vol. 114, pp. 177–180, 10 2022. [Online]. Available: http://www.redjournal.org/article/S0360301622004746/fulltext

[11] S. C. Maree, N. H. Luong, E. S. Kooreman, N. van Wieringen, A. Bel, K. A. Hinnen, H. Westerveld, B. R. Pieters, P. A. Bosman, and T. Alderliesten, "Evaluation of bi-objective treatment planning for high-dose-rate prostate brachytherapy-a retrospective observer study," *Brachytherapy*, vol. 18, pp. 396–403, 5 2019. [Online]. Available: https://pubmed.ncbi.nlm.nih.gov/30718176/

[12] R. Straathof, J. P. Meijaard, S. M. van Vliet-Pérez, I. K. Kolkman-Deurloo, R. A. Nout, B. J. M. Heijmen, L. S. G. L. Wauben, J. Dankelman, and N. J. van de Berg, "Multibody dynamic modeling of the behavior of flexible instruments used in cervical cancer brachytherapy," *Medical Physics*, 1 2024. [Online]. Available: https://research.tudelft.nl/en/publications/multibody-dynamic-modeling-of-the-behavior-of-flexible-instrument

[13] B. Morén, T. Larsson, and Åsa Carlsson Tedgren, "Optimization in treatment planning of high dose-rate brachytherapy — review and analysis of mathematical models," pp. 2057–2082, 5 2021.

[14] A. Karabis, P. Belotti, and D. Baltas, "Optimization of catheter position and dwell time in prostate hdr brachytherapy using hipo and linear programming," 2009. [Online]. Available: https://link.springer.com/chapter/10.1007/978-3-642-03474-9_172

[15] B. L. Gorissen, D. D. Hertog, and A. L. Hoffmann, "Mixed integer programming improves comprehensibility and plan quality in inverse optimization of prostate hdr brachytherapy," *Physics in Medicine & Biology*, vol. 58, p. 1041, 1 2013. [Online]. Available: https://iopscience.iop.org/article/10.1088/0031-9155/58/4/1041

[16] Åsa Holm, Åsa Carlsson Tedgren, and T. Larsson, "Heuristics for integrated optimization of catheter positioning and dwell time distribution in prostate hdr brachytherapy," *Annals of Operations Research*, vol. 236, pp. 319–339, 1 2016. [Online]. Available: https://link-springer-com.tudelft.idm.oclc.org/article/10.1007/s10479-013-1448-7

[17] T. Siauw, A. Cunha, D. Berenson, A. Atamtürk, I. C. Hsu, K. Goldberg, and J. Pouliot, "Npip: A skew line needle configuration optimization system for hdr brachytherapy," *Medical Physics*, vol. 39, pp. 4339–4346, 2012.

[18] E. Poulin, C. A. C. Fekete, M. Létourneau, A. Fenster, J. Pouliot, and L. Beaulieu, "Adaptation of the cvt algorithm for catheter optimization in high dose rate brachytherapy," *Medical Physics*, vol. 40, p. 111724, 11 2013. [Online]. Available: https://onlinelibrary.wiley.com/doi/full/10.1118/1.4826335

[19] G. Ayotte, M. D'amours, S. Aubin, Lessard, J. Pouliot, and L. Beaulieu, "Sci—thurs am: Yis—02: Optimizing number and position of catheters within inverse planning simulated annealing (ipsa) for prostate and breast high dose rate brachytherapy," *Medical Physics*, vol. 36, pp. 4315–4315, 9 2009. [Online]. Available: https://onlinelibrary-wiley-com.tudelft.idm.oclc.org/doi/full/10.1118/1.3244162

[20] C. V. Guthier, A. L. Damato, A. N. Viswanathan, J. W. Hesser, and R. A. Cormack, "A fast multitarget inverse treatment planning strategy optimizing dosimetric measures for high-dose-rate (hdr) brachytherapy," *Medical physics*, vol. 44, pp. 4452–4462, 9 2017. [Online]. Available: https://pubmed-ncbi-nlm-nih-gov.tudelft.idm.oclc.org/28626978/

[21] C. V. Guthier, K. P. Aschenbrenner, R. Müller, L. Polster, R. A. Cormack, and J. W. Hesser, "Real-time inverse high-dose-rate brachytherapy planning with catheter optimization by compressed sensing-inspired optimization strategies," *Physics in Medicine & Biology*, vol. 61, p. 5956, 7 2016. [Online]. Available: https://iopscience.iop.org/article/10.1088/0031-9155/61/16/5956

[22] R. Acosta, M. Ehrgott, A. Holder, D. Nevin, J. Reese, and B. Salter, "The influence of dose grid resolution on beam selection strategies in radiotherapy treatment design," *Optimization in Medicine*, pp. 1–23, 12 2008. [Online]. Available: https://link.springer.com/chapter/10.1007/978-0-387-73299-21

[23] M. Ehrgott, A. Holder, and J. Reese, "Beam selection in radiotherapy design," *Linear Algebra and its Applications*, vol. 428, pp. 1272–1312, 3 2008.

[24] C. H. J. Lee, D. M. Aleman, and M. B. Sharpe, "A set cover approach to fast beam orientation optimization in intensity modulated radiation therapy for total marrow irradiation," *Physics in Medicine and Biology*, vol. 56, pp. 5679–5695, 9 2011. [Online]. Available: https://www.researchgate.net/publication/51559229

[25] D. M. Aleman and M. B. Sharpe, "Optimization methods for total marrow irradiation using intensity modulated radiation therapy," *https://doi.org/10.3138/infor.49.4.234*, vol. 49, pp. 234–240, 11 2017. [Online]. Available: https://www.tandfonline.com/doi/abs/10.3138/infor.49.4.234

[26] O. C. Haas, K. J. Burnham, and J. A. Mills, "Optimization of beam orientation in radiotherapy using planar geometry," *Physics in medicine and biology*, vol. 43, pp. 2179–2193, 1998. [Online]. Available: https://pubmed.ncbi.nlm.nih.gov/9725597/

[27] M. Ehrgott and R. Johnston, "Optimisation of beam directions in intensity modulated radiation therapy planning," *OR Spectrum*, vol. 25, pp. 251–264, 2003. [Online]. Available: https://link.springer.com/article/10.1007/s00291-003-0124-8

[28] L. Liang, D. Cool, N. Kakani, G. Wang, H. Ding, and A. Fenster, "Automatic radiofrequency ablation planning for liver tumors with multiple constraints based on set covering," *IEEE Transactions on Medical Imaging*, vol. 39, pp. 1459–1471, 5 2020. [Online]. Available: https://ieeexplore.ieee.org/document/8890690/

[29] P. Yu, T. Fu, C. Wu, Y. Jiang, and J. Yang, "Automatic radiofrequency ablation planning for liver tumors: A planning method based on the genetic algorithm with multiple constraints," *ACM International Conference Proceeding Series*, pp. 8–14, 8 2021. [Online]. Available: https://dl.acm.org/doi/10.1145/3484377.3484379
[30] S. Kulkarni-Thaker, D. M. Aleman, and A. Fenster, "A row-generation approach for simultaneous multiple needle trajectory planning in radiofrequency ablation," *medRxiv*, p. 2021.06.11.21258244, 6 2021. [Online]. Available: https://www.medrxiv.org/content/10.1101/2021.06.11.21258244v1
[31] R. Straathof, S. van Vliet-Pérez, I.-K. K. Kolkman-Deurloo, L. S. Wauben, R. A. Nout, B. J. Heijmen, L. Rossi, J. Dankelman, and N. J. van de Berg1, "Automated planning of curved source channels in 3d-printed patient-tailored applicators for cervical cancer brachytherapy," *[TO BE PUBLISHED]*, 2024.
[32] A. Garg, S. Patil, T. Siauw, J. A. M. Cunha, I. C. Hsu, P. Abbeel, J. Pouliot, and K. Goldberg, "An algorithm for computing customized 3d printed implants with curvature constrained channels for enhancing intracavitary brachytherapy radiation delivery," *IEEE International Conference on Automation Science and Engineering*, pp. 466–473, 2013.
[33] Y. Duan, S. Patil, J. Schulman, K. Goldberg, and P. Abbeel, "Planning locally optimal, curvature-constrained trajectories in 3d using sequential convex optimization," *Proceedings - IEEE International Conference on Robotics and Automation*, pp. 5889–5895, 9 2014.
[34] S. Patil, J. Pan, P. Abbeel, and K. Goldberg, "Planning curvature and torsion constrained ribbons in 3d with application to intracavitary brachytherapy," *IEEE Transactions on Automation Science and Engineering*, vol. 12, pp. 1332–1345, 10 2015.
[35] K. Yang and S. Sukkarieh, "3d smooth path planning for a uav in cluttered natural environments," *2008 IEEE/RSJ International Conference on Intelligent Robots and Systems, IROS*, pp. 794–800, 2008.
[36] Z. Zhang, X. Liu, and B. Feng, "Research on obstacle avoidance path planning of uav in complex environments based on improved bézier curve," *Scientific Reports 2023 13:1*, vol. 13, pp. 1–10, 9 2023. [Online]. Available: https://www.nature.com/articles/s41598-023-43783-7
[37] H. Li, Y. Luo, and J. Wu, "Collision-free path planning for intelligent vehicles based on bézier curve," *IEEE Access*, vol. 7, pp. 123 334–123 340, 2019.
[38] J. Chen, P. Zhao, T. Mei, and H. Liang, "Lane change path planning based on piecewise bezier curve for autonomous vehicle," *Proceedings of 2013 IEEE International Conference on Vehicular Electronics and Safety, ICVES 2013*, pp. 17–22, 2013.
[39] F. Gao, W. Wu, Y. Lin, and S. Shen, "Online safe trajectory generation for quadrotors using fast marching method and bernstein basis polynomial," *Proceedings - IEEE International Conference on Robotics and Automation*, pp. 344–351, 9 2018.
[40] J. W. Chang, Y. K. Choi, M. S. Kim, and W. Wang, "Computation of the minimum distance between two bézier curves/surfaces," *Computers & Graphics*, vol. 35, pp. 677–684, 6 2011.
[41] T. M. Works and Inc., "Matlab version 2021b," 2021. [Online]. Available: https://nl.mathworks.com/
[42] "Gurobi optimizer reference manual - gurobi optimization." [Online]. Available: https://www.gurobi.com/documentation/current/refman/index.html
[43] H. W. Kuhn, "The hungarian method for the assignment problem," *Naval Research Logistics Quarterly*, vol. 2, pp. 83–97, 3 1955. [Online]. Available: https://onlinelibrary.wiley.com/doi/full/10.1002/nav.3800020109
[44] R. C. Veltkamp and W. Wesselink, "Modeling 3d curves of minimal energy," *Computer Graphics Forum*, vol. 14, pp. 97–110, 8 1995. [Online]. Available: https://onlinelibrary.wiley.com/doi/full/10.1111/j.1467-8659.1995.cgf143&0097.x
[45] Y. J. Ho and J. S. Liu, "Collision-free curvature-bounded smooth path planning using composite bezier curve based on voronoi diagram," *Proceedings of IEEE International Symposium on Computational Intelligence in Robotics and Automation, CIRA*, pp. 463–468, 2009.
[46] C. E. Luis, M. Vukosavljev, and A. P. Schoellig, "Online trajectory generation with distributed model predictive control for multi-robot motion planning," *IEEE Robotics and Automation Letters*, vol. 5, pp. 604–611, 4 2020.
[47] T. Mercy, R. V. Parys, and G. Pipeleers, "Spline-based motion planning for autonomous guided vehicles in a dynamic environment," *IEEE Transactions on Control Systems Technology*, vol. 26, pp. 2182–2189, 11 2018.
[48] G. V. den Bergen, "A fast and robust gjk implementation for collision detection of convex objects," *Journal of Graphics Tools*, vol. 4, pp. 7–25, 1 1999. [Online]. Available: https://www.tandfonline.com/doi/abs/10.1080/10867651.1999.10487502
[49] B. Sabetghadam, R. Cunha, and A. Pascoal, "Real-time trajectory generation for multiple drones using bézier curves," *IFAC-PapersOnLine*, vol. 53, pp. 9276–9281, 1 2020.
[50] A. Manikandan, B. Sarkar, V. T. Rajendran, P. R. King, N. V. M. Sresty, R. Holla, S. Kotur, and S. Nadendla, "Role of step size and max dwell time in anatomy based inverse optimization for prostate implants," *Journal of Medical Physics / Association of Medical Physicists of India*, vol. 38, p. 148, 7 2013. [Online]. Available: https://www.ncbi.nlm.nih.gov/pmc/articles/PMC3775040/
[51] M. C. van der Meer, P. A. Bosman, Y. Niatsetski, T. Alderliesten, N. van Wieringen, B. R. Pieters, and A. Bel, "Bi-objective optimization of catheter positions for high-dose-rate prostate brachytherapy," *Medical physics*, vol. 47, pp. 6077–6086, 12 2020. [Online]. Available: https://pubmed.ncbi.nlm.nih.gov/33000874/
[52] P. McGeachy, J. Madamesila, A. Beauchamp, and R. Khan, "An open-source genetic algorithm for determining optimal seed distributions for low-dose-rate prostate brachytherapy," *Brachytherapy*, vol. 14, pp. 692–702, 9 2015. [Online]. Available: https://pubmed.ncbi.nlm.nih.gov/26023047/
[53] M. C. V. D. Meer, T. Alderliesten, B. R. Pieters, A. Bel, Y. Niatsetski, and P. A. Bosman, "Better and faster catheter position optimization in hdr brachytherapy for prostate cancer using multi-objective real-valued gomea," *GECCO 2018 - Proceedings of the 2018 Genetic and Evolutionary Computation Conference*, pp. 1387–1394, 7 2018. [Online]. Available: https://dl-acm-org.tudelft.idm.oclc.org/doi/10.1145/3205455.3205505
[54] J. P. V. D. Berg and M. H. Overmars, "Prioritized motion planning for multiple robots," *2005 IEEE/RSJ International Conference on Intelligent Robots and Systems, IROS*, pp. 430–435, 2005.
[55] K. Azarm and G. Schmidt, "Conflict-free motion of multiple mobile robots based on decentralized motion planning and negotiation," *Proceedings - IEEE International Conference on Robotics and Automation*, vol. 4, pp. 3526–3533, 1997.
[56] J. R. Heselden and G. P. Das, "Heuristics and rescheduling in prioritised multi-robot path planning: A literature review," *Machines 2023, Vol. 11, Page 1033*, vol. 11, p. 1033, 11 2023. [Online]. Available: https://www.mdpi.com/2075-1702/11/11/1033/
[57] M. Bennewitz, W. Burgard, and S. Thrun, "Optimizing schedules for prioritized path planning of multi-robot systems," *Proceedings - IEEE International Conference on Robotics and Automation*, vol. 1, pp. 271–276, 2001.
[58] R. Regele and P. Levi, "Cooperative multi-robot path planning by heuristic priority adjustment," *2006 IEEE/RSJ International Conference on Intelligent Robots and Systems*, pp. 5954–5959, 2006.
[59] C. M. Clark, T. Bretl, and S. Rock, "Applying kinodynamic randomized motion planning with a dynamic priority system to multi-robot space systems," *IEEE Aerospace Conference Proceedings*, vol. 7, pp. 3621–3631, 2002.
[60] A. Andreychuk and K. Yakovlev, "Two techniques that enhance the performance of multi-robot prioritized path planning," *Proceedings of the International Joint Conference on Autonomous Agents and Multiagent Systems, AAMAS*, vol. 3, pp. 2177–2179, 5 2018. [Online]. Available: https://arxiv.org/abs/1805.01270v1
[61] J. Jiao, Z. Cao, P. Zhao, X. Liu, and M. Tan, "Bezier curve based path planning for a mobile manipulator in unknown environments," *2013 IEEE International Conference on Robotics and Biomimetics, ROBIO 2013*, pp. 1864–1868, 2013.
[62] P. C. Niedfeldt and R. W. Beard, "Recursive ransac: Multiple signal estimation with outliers," *IFAC Proceedings Volumes*, vol. 46, pp. 430–435, 1 2013.
[63] H. Isack and Y. Boykov, "Energy-based geometric multi-model fitting," *International Journal of Computer Vision*, vol. 97, pp. 123–147, 4 2012.
[64] L. Magri and A. Fusiello, "Multiple models fitting as a set coverage problem," *Proceedings of the IEEE Computer Society Conference on Computer Vision and Pattern Recognition*, vol. 2016-December, pp. 3318–3326, 12 2016.
[65] S. Kulkarni-Thaker, D. M. Aleman, and A. Fenster, "Inverse planning for radiofrequency ablation in cancer therapy using multiple damage models," *medRxiv*, p. 2021.06.07.21258239, 6 2021. [Online]. Available: https://www.medrxiv.org/content/10.1101/2021.06.07.21258239v1
[66] M. Bangert and U. Oelfke, "Spherical cluster analysis for beam angle optimization in intensity-modulated radiation therapy treatment planning," *Physics in Medicine & Biology*, vol. 55, p. 6023, 9 2010. [Online]. Available: https://iopscience-iop-org.tudelft.idm.oclc.org/article/10.1088/0031-9155/55/19/025
[67] Z. Zhou, J. Li, J. Tu, R. Xin, W. Zhang, and D. Wu, "Clustering of nasopharyngeal carcinoma intensity modulated radiation therapy plans

based on k-means algorithm and geometrical features," *International Journal of Radiation Research*, vol. 19, pp. 13–21, 1 2021.

[68] J. C. Lindegaard, M. L. Madsen, A. Traberg, B. Meisner, S. K. Nielsen, K. Tanderup, H. Spejlborg, L. U. Fokdal, and O. Nørrevang, "Individualised 3d printed vaginal template for mri guided brachytherapy in locally advanced cervical cancer," *Radiotherapy and oncology : journal of the European Society for Therapeutic Radiology and Oncology*, vol. 118, pp. 173–175, 1 2016. [Online]. Available: https://pubmed.ncbi.nlm.nih.gov/26743833/

[69] M. Serban, L. Fokdal, S. K. Nielsen, S. B. Hokland, A. T. Hansen, H. Spejlborg, S. Rylander, P. Petric, J. C. Lindegaard, and K. Tanderup, "Characterization of combined intracavitary/interstitial brachytherapy including oblique needles in locally advanced cervix cancer," *Brachytherapy*, vol. 20, pp. 796–806, 7 2021. [Online]. Available: https://pubmed.ncbi.nlm.nih.gov/33994344/

[70] H. B. Z. Logar, R. Hudej, and B. Šegedin, "Development and assessment of 3d-printed individual applicators in gynecological mri-guided brachytherapy," *Journal of Contemporary Brachytherapy*, vol. 11, p. 128, 2019. [Online]. Available: https://www.ncbi.nlm.nih.gov/pmc/articles/PMC6536148/

[71] D. Zhang, Z. Yang, S. Jiang, L. Zhou, Z. Zhou, and W. Wang, "Individualized and inverse optimized needle configuration for combined intracavitary-interstitial brachytherapy in locally advanced cervical cancer," *Journal of cancer research and therapeutics*, vol. 15, pp. 1589–1596, 10 2019. [Online]. Available: https://pubmed.ncbi.nlm.nih.gov/31939442/

[72] M. R. Arnfield, P. S. Lin, M. A. Manning, D. W. Arthur, B. D. Kavanagh, R. D. Zwicker, and R. K. Schmidt-Ullrich, "The effect of high-dose-rate brachytherapy dwell sequence on cell survival," *International Journal of Radiation Oncology*Biology*Physics*, vol. 52, pp. 850–857, 3 2002.

[73] L. Fokdal, K. Tanderup, S. B. Hokland, L. Røhl, E. M. Pedersen, S. K. Nielsen, M. Paludan, and J. C. Lindegaard, "Clinical feasibility of combined intracavitary/interstitial brachytherapy in locally advanced cervical cancer employing mri with a tandem/ring applicator in situ and virtual preplanning of the interstitial component," *Radiotherapy and oncology : journal of the European Society for Therapeutic Radiology and Oncology*, vol. 107, pp. 63–68, 4 2013. [Online]. Available: https://pubmed.ncbi.nlm.nih.gov/23452917/

5 EXTENSIVE EXPLANATION CONCEPTS IN PAPER

In this chapter, a more extensive explanation of some of the concepts presented in the paper is given, specifically focusing on the grid configuration (Section 5.1), the candidate set creation (Section 5.2), the set cover formulation (Section 5.3), the path planner (Section 5.4), the matching algorithm (Section 5.5), and the iterative replanning (Section 5.6).

5.1. GRID CONFIGURATION

To obtain the high-potential dwell positions, BiCycle is used on a grid of possible dwell positions. The grid is created in the direction of the IU tandem with a uniform step size. The grid points inside the OARs are removed to speed up the optimisation. An example of a grid placed in the anatomy of a patient is shown in Figure 5.1.

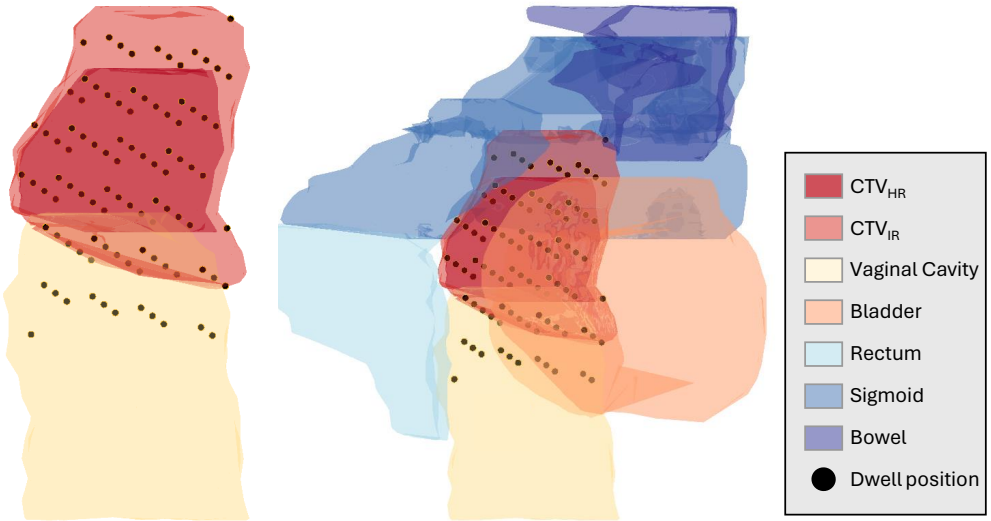

Figure 5.1: Visualisation of a grid of possible dwell positions placed on the anatomy of a patient without OARs (left) and with OARs (right).

A modified version of BiCycle is used on this grid. The inputs for BiCycle are the structure set (RTStruct) and the treatment plan (RTPlan), which are both in DICOM (.dcm) format. The RTPlan contains the dwell positions that can be used. BiCycle uses a wishlist that separates the tandem, ovoids, and needle contributions. All grid points are artificially placed in the tandem structure. As BiCycle includes smoothing of the dwell times per channel, and all dwell points are now contained in a single channel, the smoothing definition needs to be modified. The new smoothing definition is normalised for the amount of dwell points in the channel. Moreover, the relative contributions of the different parts are not relevant as all points that are to be considered are placed in the tandem. The BiCycle wishlist used for the grid configurations and the clinical wishlist are shown in Section A.1 and Section A.2, respectively.

5.2. CANDIDATE SET CREATION

As stated, in this work the high-quality candidate set is generated based on the candidate dwell positions. There are different types of needles created based on these candidate dwell positions. The different needle types are described below and are visualised in Figure 5.2.

The different needle types are the shortest needle (left), the tandem direction needle (middle), and the group needle (right). The shortest needle is created from a single dwell point to the closest point in the coverable region (purple). The tandem direction needle is created by finding the closest point in the coverable region in the direction of the IU tandem from the candidate dwell position. The group needles combine multiple dwell positions with one needle. Firstly, a line is fitted through all candidate dwell positions in the group (green line). Secondly, the closest point in the coverable region to the fitted line is found (black star). Lastly, a line is fitted through all candidate dwell positions in the group, enforcing the closest point to be on the line (blue line). The resulting line is the group needle.

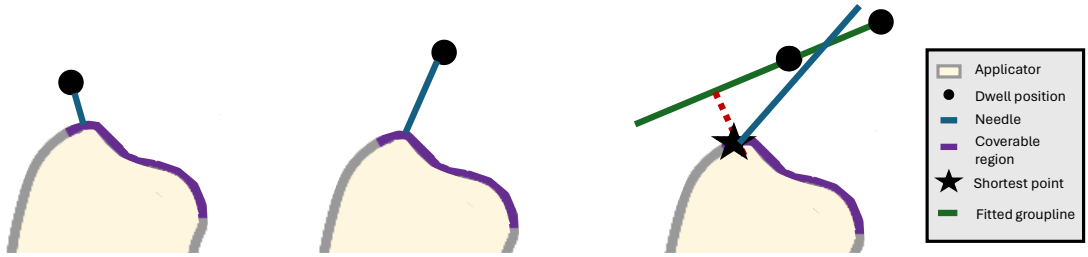

Figure 5.2: Visualisation of different needle types: the shortest needle (left), the tandem direction needle (middle), and the group needle (right).

5.3. SET COVER FORMULATION

To select the best set of needle segments from the candidate set to cover all candidate dwell points, a weighted set cover problem (WSCP) formulation is used. The WSCP formulated as an integer linear program (ILP) is solved using the state-of-the-art solver Gurobi (Beaverton, Oregon, USA) [65]. Gurobi includes deterministic, parallel branch-and-cut, nontraditional tree-of-trees search, multiple default heuristics, solution improvements, cutting planes, and symmetry detection algorithms and is created by Gurobi optimisation. Gurobi is often used in literature for coverage problems, for example, for set cover [66], max cover [67], and facility location [68].

In our problem formulation of the WSCP $U = 1, 2, ..., n$ is a ground set of n candidate dwell points. $\mathbb{S}$ is the candidate set of m candidate needle segments of U, $|\mathbb{S}| = m$. A cover C is a collection of sets $C \subset \mathbb{S}$ whose union is U. Each needle segment $s \in \mathbb{S}$ has a cost c_s. The goal is to find a cover of maximum cost.

$$\text{maximise} \quad \sum_{s=1}^{m} c_s x_s \qquad \text{(WSCP)} \tag{5.1a}$$

$$\text{subject to} \quad \sum_{s:e\in\mathbb{S}} A_{s,j} \geq 1 \quad \text{for all } j \in U \tag{5.1b}$$

$$x_s \in \{0,1\} \quad \text{for all } s \in \mathbb{S} \tag{5.1c}$$

$$x_y + x_z \leq 1 \quad \text{for all } (y,z) \in \mathbb{B} \tag{5.1d}$$

$$\sum_{s=1}^{m} x_s \leq N_{\max} \tag{5.1e}$$

In this formulation, x_s denotes if needle s has been selected, and $A_{s,j}$ denotes if dwell point j has been covered by needle s. Constraint (5.1b) ensures that all dwell points are covered by at least one needle. Dwell points within the cover distance d_c from the needle are said to be covered by a needle. As the

needles need to be mutually collision-free, constraint (5.1d) prevents collision pairs from being selected, as distinguished by the pairwise validity matrix $\mathbb{B}$. Lastly, the number of selected needles is limited to $N_{\max}$ by constraint (5.1e).

The constraints of the WSCP are added to the optimisation in Gurobi. Constraints (5.1b),(5.1d) and (5.1e) are added as inequality constraints. Constraint (5.1c) is enforced by constraining every element of x to 1 or 0. The implementations of the different inequality constraints in the optimisation are explained below.

The covering constraint (5.1b) can be posed as the following linear inequality constraints:

$$-A_{n\times m}\ x_{m\times 1} \quad \leq \quad \mathbf{1}_{n\times 1} \tag{5.2}$$

The columns of A belonging to the dwell points within the cover distance from the IU tandem are filled with ones, ensuring these dwell points do not have to be covered by needles anymore. The collision constraints (5.1d) are added with the following linear inequality constraints:

$$C_{m\times m}\ x_{m\times 1} \quad \leq \quad \mathbf{1}_{m\times 1} \tag{5.3}$$

In the collision matrix C, $C_{y,z}$ is 1 for every colliding needle pair y,z. All elements on the diagonal are set as 1 and all elements below the diagonal are set to zero. The forbidden needle pairs and forbidden needles are implemented making use of the collision matrix. A forbidden needle pair (o,p) is added by setting $C_{o,p}$ to 1 and for a forbidden needle (v), $C_{v,v}$ is set to 2. The number of needles that are selected is constrained by constraint (5.1e). This constraint is implemented by ensuring that a $(1 \times m)$ array filled with ones, multiplied by the needle-selecting array is smaller or equal to $N_{\max}$ for every index.

Needles are scored based on the inverse squared distance to the dwell positions covered by the needle, and weighted by the corresponding dwell time in the BiCycle plan on the grid configuration. The cost of a needle, c_s, is given by:

$$c_s = -\sum_{j\in U} A_{s,j}\, d_{s,j}^2\, t_j \tag{5.4}$$

All dwell positions inside the cover distance are used in the score of a needle, even though another selected needle might also cover the dwell position. Hence, the selection of the cover distance is critical for the success of the set cover formulation. Selecting a too large cover distance results in central needles covering a lot of dwell positions and, therefore, getting a more negative score. While needles on the side cover fewer needles and get a less negative score. If the cover distance is too low, there is no feasible solution. Hence, the cover distance is iteratively increased until a feasible solution is found, ensuring that the cover distance is as low as possible and reducing the possibility of penalising for distances to the same dwell positions more than once. An example visualisation of the effect of the cover distance on the selection of at most two needles out of a candidate set is shown in Figure 5.3. Here, a too low cover distance (left), leads to no feasible solution. A too large cover distance (middle), results in the dwell point distances counting in all needles and therefore the selection of only the red needle. If the cover distance is set properly (right), the blue and green needles are selected, resulting in a total minimum distance between the dwell points and the closest needle when selecting two needles at maximum.

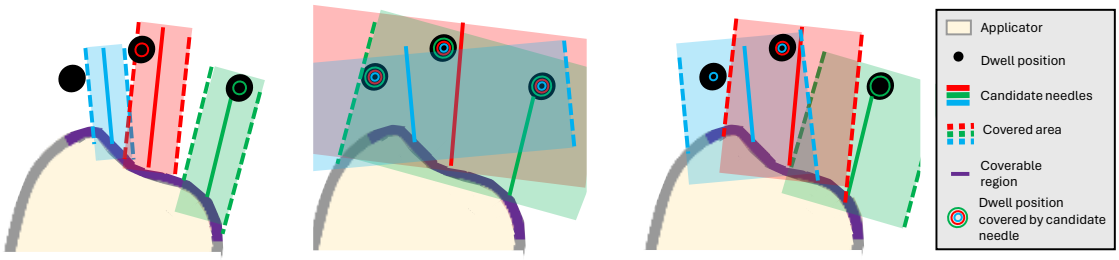

Figure 5.3: Visualisation of the effect of different cover distances. In the image, there are three dwell positions (black circles) to be covered by a maximum of two needles (red, blue and green). The cover distance is shown by the filled rectangles bounded by the striped lines. If a dwell point is covered by a needle is indicated by the coloured circles on the dwell position. If the cover radius is too small (left), no feasible solution is found. If the cover radius is too large (middle) the dwell point distances count in multiple needles and the algorithm prefers the selection of few needles. In this case, only the red needle would be selected. If the cover distance is correct (right), the algorithm selects the optimal needles (blue and green).

5.4. PATH PLANNER

The source channels' centrelines in this work are represented by Bézier curves. Bézier curves are based on Bernstein's polynomial bases. The formula for a Bernstein's polynomial basis is shown below:

$$b_n^i(t) = \binom{n}{i} \cdot t^i \cdot (t-1)^{n-i} \tag{5.5}$$

A linear combination of Bernstein basis polynomials is called a Bézier curve. The formula for a Bézier curve is shown in (5.6). Here, c_j is the set of control points of the jth piece of the Bézier curve.

$$B_j(t) = c_j^0 b_n^0(t) + c_j^1 b_n^1(t) + ... = \sum_{i=0}^{n} c_j^i b_n^i(t) \tag{5.6}$$

A Bézier curve has different properties that are listed in Table 5.1 [69].

Table 5.1: Table containing the properties of a Bézier curve and their explanation.

Property	Description
Convex hull property	Bézier curves are always completely contained within the convex hull of their control points.
Endpoint interpolation property	A Bézier curve's initial and final points are the first and the last control points respectively.
Hodograph property	The derivative of an nth order Bézier curve is an (n-1)th order Bézier curve.
Fixed interval property	The Bézier curve parameterised to variable t is defined on $t \in [0,1]$.

5.4.1. MINIMUM ENERGY FORMULATION

As stated before the curvature of the needle path (κ) needs to be minimised. This can be done by minimising the bending energy of a curve (E_{bend}) [70]. The bending energy of an in-extensible linearly elastic rod can be calculated in the following way:

$$E_{bend}(x) = \int \kappa^2(t)||x'(t)||dt \tag{5.7}$$

The computation of the curvature is computationally expensive. Hence, the bending energy can be approximated with equation (5.8).

$$\overline{E}_{bend} = \int ||x''(t)||^2 dt \tag{5.8}$$

The cost function for minimising the kth derivative of a Bézier curve (J) can be written in the following way [52]:

$$J = \sum_{\mu \in [x,y,z]} \int_0^T \left(\frac{d^k f_\mu(t)}{dt^k}\right) dt \tag{5.9}$$

For minimising the bending energy, the second derivative is to be minimised ($k = 2$). Hence, this problem can be rewritten into a quadratic problem, $P^T Q_0 P$, where P contains all three dimensions of the control points in a single column and Q_0 is the Hessian of the objective. The calculation of Q_0 will be explained below. The kth derivative of a Bézier curve of order n can be represented as the following, as it only requires the derivative of the Bernstein basis and not of the control points, with $g_m(\tau) = \sum c_\mu^i b_n^i(\tau)$. The derivative also follows a De Casteljau scheme.

$$\frac{d^k}{d\tau^k} g_\mu(\tau) = \frac{n!}{(n-k)!} \sum_{i=0}^{n-k} \Delta^k c_\mu^i b_{n-k}^i \tag{5.10}$$

$$\Delta^k c_\mu^i = \Delta^{k-1} c_\mu^{i+1} - \Delta^{k-1} c_\mu^i \tag{5.11}$$

In the case of bending energy minimisation with $k = 2$, the forward difference operator Δ^k is:

$$\Delta^2 c_\mu^i = \Delta^1 c_\mu^{i+1} - \Delta^1 c_\mu^i = c_\mu^{i+2} - 2c_\mu^{i+1} + c_\mu^i \tag{5.12}$$

The derivative can also be expressed in matrix form:

$$\frac{d^k}{d\tau^k} g_\mu(\tau) = b^k(\tau)^T D^k p \tag{5.13}$$

$$b^k(\tau)^T = [b_{n-k}^0, b_{n-k}^1, ..., b_{n-k}^{n-k}] \tag{5.14}$$

$$p = [c_\mu^0, c_\mu^1, ..., c_\mu^n]^T \tag{5.15}$$

$$D^k = \frac{n!}{(n-k)!} \begin{pmatrix} -1 & & 1 & & \\ & \ddots & & \ddots & \\ & & -1 & & 1 \end{pmatrix} \tag{5.16}$$

D_r is the forward difference operator as a $(n-k) \times n$ matrix. This split makes the cost function the following:

$$J_\mu = \frac{1}{s^{2k-a}} p^T D^{k\,t} \left(\int_0^1 b^k(\tau) b^k(\tau)^T d\tau \right) D^k p \tag{5.17}$$

The part between the brackets is H^k.

$$H_{a,b}^k = \int_0^1 b^k(\tau) b^k(\tau)^T d\tau = \binom{n-k}{a} \binom{n-k}{b} \int_0^1 \tau^{a+b} (1-\tau)^{2n-2k-a-b} d\tau = \frac{\binom{n-k}{a}\binom{n-k}{b}}{\binom{2n-2k}{a+b}} \frac{1}{2n-2k+1} \tag{5.18}$$

This follows from the multiplication of two Bernstein bases [71]:

$$b_{n-k}^a b_{n-k}^b = \frac{\binom{n-k}{a}\binom{n-k}{b}}{\binom{2n-2k}{a+b}} b_{2n-2k}^{a+b} \tag{5.19}$$

$$\text{where: } \int_0^1 b_n^i dx = \frac{1}{n+1} \tag{5.20}$$

The cost function per dimension then becomes the following matrix product:

$$J_\mu = \begin{pmatrix} c_\mu^0 \\ \vdots \\ c_\mu^n \end{pmatrix}^T \begin{pmatrix} \frac{1}{s_0^{2k-a}} {D^k}^T H^k D^k & & \\ & \ddots & \\ & & \frac{1}{s_n 2k-a} {D^k}^T H^k D^k \end{pmatrix} \begin{pmatrix} c_\mu^0 \\ \vdots \\ c_\mu^n \end{pmatrix} \tag{5.21}$$

By adding the other dimensions of μ one arrives at the quadratic problem:

$$J = \begin{pmatrix} c_x^0 \\ \vdots \\ c_x^n \\ \vdots \\ c_z^0 \\ \vdots \\ c_z^n \end{pmatrix}^T Q_0 \begin{pmatrix} c_x^0 \\ \vdots \\ c_x^n \\ \vdots \\ c_z^0 \\ \vdots \\ c_z^n \end{pmatrix} \tag{5.22}$$

To ensure that the location and direction of both the start and endpoint of the source channel are correct, two types of equality constraints are incorporated into the optimisation: the position constraints and the direction constraints. The position constraints make use of the endpoint interpolation property and the direction constraints make use of the hodograph property. The resulting optimisation is solved using the MATLAB optimisation routine fmincon and is shown below:

$$\text{minimise} \quad \sum_{k=0}^{m} J_q \tag{5.23a}$$

$$\text{subject to} \quad c_{\mu,q}^0 = P_{\text{entry},\mu} \qquad \forall \mu, \forall q \in \mathbb{M} \tag{5.23b}$$

$$c_{\mu,q}^n = P_{\text{needle},\mu} \qquad \forall \mu, \forall q \in \mathbb{M} \tag{5.23c}$$

$$\hat{u}_{\mu 1,q} c_{\mu 1,q}^1 + \hat{u}_{\mu 2,q} c_{\mu 2,q}^1 = \hat{u}_{\mu 1,q} c_{\mu 1,q}^0 + \hat{u}_{\mu 2,q} c_{\mu 2,q}^0 \qquad \forall \mu 1, \forall \mu 2, (\mu 1 \neq \mu 2), \forall q \in \mathbb{M} \tag{5.23d}$$

$$\hat{v}_{\mu 1,q} c_{\mu 1,q}^{n-1} + \hat{v}_{\mu 2,q} c_{\mu 2,q}^{n-1} = \hat{v}_{\mu 1,q} c_{\mu 1,q}^n + \hat{v}_{\mu 2,q} c_{\mu 2,q}^n \qquad \forall \mu 1, \forall \mu 2, (\mu 1 \neq \mu 2), \forall q \in \mathbb{M} \tag{5.23e}$$

Here $\mathbb{M}$ contains all m selected needles. The equality constraint for the qth needle consists of different parts. Firstly, all three dimensions of the first control point are set to be equal to the corresponding entry point dimension ($P_{\text{entry},\mu}$) with constraint (5.23b). Similarly, all three dimensions of the last control point are set to be equal to the corresponding needle segment location ($P_{\text{needle},\mu}$) with constraint (5.23c). Secondly, the second control point location is constrained to be in the upward direction ($\hat{u}$) by adding three equality constraints each enforcing the point to be on a plane (5.23d). The three planes used are the planes defined by two of the three direction dimensions ($\mu 1, \mu 2$). Similarly, the second to last control point location is constrained to be in the direction of the needle segment ($\hat{v}$) by adding three plane constraints (5.23e). The total equality constraint matrix is created by adding the equality constraint matrix per needle on the diagonal of the total equality constraint matrix.

5.4.2. COLLISION AVOIDANCE

The planned source channel paths need to be mutually collision-free. This can be checked by making use of the convex hull property [72], which results in overly conservative bounds[73], [74]. Another option is to use a point-per-point evaluation, which is slow and might suffer from the tunnelling effect. Hence, a method with a converging lower and upper bound on the distance between two Bézier curves is used [75]. The pseudocode for this method is shown in Algorithm 1 and a visualisation of the process is shown in Figure 5.4. The method is explained below.

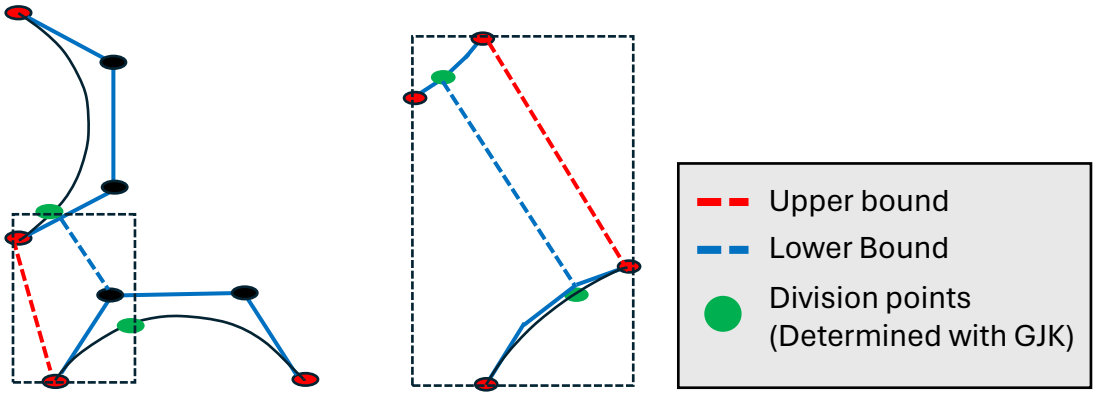

Figure 5.4: Visualisation of an example of the fast distance determination algorithm. The Bézier curves are shown in the black lines and their control points are shown with the black circles. The upper bound (red striped line) is the minimum distance between the first and last control points (red circles). The blue line represents the lower bound and is determined by the minimum distance between the convex hulls (blue lines) of the control points. If the relative difference between the bounds is too high, the Bézier curves are split in the division points (green circles) and the process is repeated (see black striped rectangle) until the difference is within the bounds.

Let two Bézier curves be defined as:

$$C_1(u) = \sum_{i=0}^{n} P_i B_i^n(u) \qquad C_2(v) = \sum_{j=0}^{m} Q_j B_j^m(v)$$

In these curves $u, v \in [0,1]$ and $B_i^n(u)$ and $B_j^m(v)$ are the nth and mth degree Bézier basis functions. P_i and Q_j are the control points in 3D space.

Algorithm 1 Computing the minimum distance α between a given pair of nodes

Require: The global upper bound of minimum distance α, two set of points $N1, N2$, and a tolerance ϵ
  if upperbound$(N_1,N_2) \leq \alpha$ **then**
    $\alpha \leftarrow$ upperbound(N_1,N_2)
  end if
  if lowerbound$(N_1,N_2) \geq \alpha(1-\epsilon)$ **then**
    return α
  else
    Subdivide N_1 into N_{11} and N_{12}
    Subdivide N_2 into N_{21} and N_{22}
    $\alpha \leftarrow$ min $(\alpha$, Algorithm 1$(N_{11},N_{21},\alpha))$
    $\alpha \leftarrow$ min $(\alpha$, Algorithm 1$(N_{11},N_{22},\alpha))$
    $\alpha \leftarrow$ min $(\alpha$, Algorithm 1$(N_{12},N_{21},\alpha))$
    $\alpha \leftarrow$ min $(\alpha$, Algorithm 1$(N_{12},N_{22},\alpha))$
  end if
  return α

It is guaranteed that the distance between two points on the different Bézier curves is greater than or equal to the minimum distance between the Bézier curves. Therefore, the upper bound on the minimum distance between two Bézier curves can be obtained by sampling two points. By making use of the endpoint interpolation property, the upper bound can be determined whilst reducing the sampling cost. According to the endpoint interpolation property the following holds: $P_0 = C_1(0), P_n = C_1(1), Q_0 = C_2(0), Q_m = C_2(1)$. The upper bound of the minimum distance can be any one of $|P_0 - Q_0|, |P_0 - Q_m|, |P_n - Q_0|, |P_n - Q_m|$. Hence, the upper bound is set as the minimum of these four values.

In the determination of the lower bound (blue striped line) the convex hull property is used. The lower bound is set to be the minimum distance between the two convex hulls of the Bézier curves. To determine the minimum distance between two convex hulls the GJK algorithm is used [76].

To decrease the gap between the upper and lower bounds in the algorithm, a dynamic scheme for node division is used. This is based on the use of minimum distance points on the two convex hulls. By subdividing the Bézier curve as close to this closest point pair, faster convergence of the algorithm can be achieved. The GJK algorithm returns the closest point pair as a weighted combination of the vertices of the convex hulls. The parameters for the subdivision are then calculated as follows:

$$u^* = \sum_{i=0}^{n} x_i \frac{i}{n}, \qquad v^* = \sum_{j=0}^{m} x_j \frac{j}{m} \tag{5.24}$$

The Bézier curves are then subdivided using De Casteljau's algorithm at u^* and v^* respectively (green points) [77]. If the relative difference between the upper and lower bound is larger than the tolerance, the process is repeated on the re-divided Bézier curves. This is visualised in the black-striped square.

The collision constraints (5.25) are added as nonlinear constraints to the optimisation formulation found in (5.23).

$$d_{y,z,\text{fast}} - d_{y,z,\text{needed}} < 0 \quad \forall (y,z) \in \mathbb{M} \quad \& \quad \forall y \in \mathbb{M}, z \in \mathbb{T} \tag{5.25}$$

Here, $d_{\text{y,z,fast}}$ is the distance between needles y and z or between needle y and part z of the IU tandem structure according to the fact-checking algorithm. The parts of the IU tandem structure in $\mathbb{M}$ are the small and the large IC tubes. $d_{y,z,\text{needed}}$ is the minimum distance between two needles (y,z) or between a needle y and a part z of the IU tandem. In Figure 5.5 the different parts of the IU tandem structure are shown. In this work, the IC tandem tubes are also modelled with two Bézier curves ($\mathbb{T}$). Therefore, in total, there are $\frac{N_{\text{needles}} \cdot (N_{\text{needles}}-1)}{2} + 2 \cdot N_{\text{needles}}$ nonlinear collision constraints.

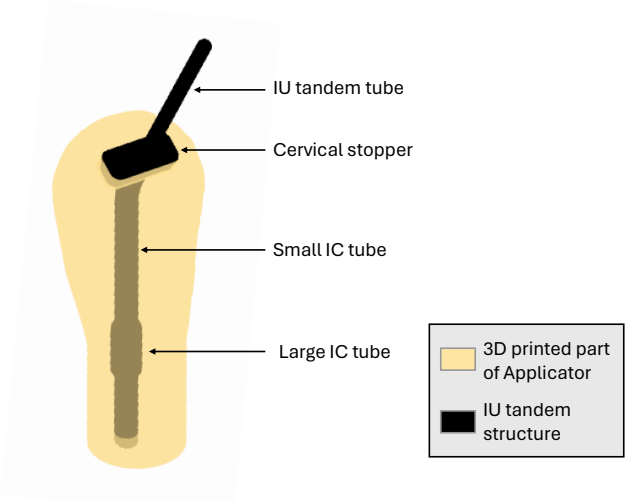

Figure 5.5: Visualisation of the ARCHITECT applicator with different parts of the IU tandem structure annotated.

5.5. MATCHING ALGORITHM

To plan paths from the needle segments to the entry points, needle segments and entry points are matched considering that their respective channel should have minimum curvature and be collision-free. The heuristic used to consider these constraints is the distance between the entry points and the needle segments projected onto a matching plane. This process is visualised in Figure 5.7 and explained below. In Figure 5.6, a visualisation of the entry region is shown.

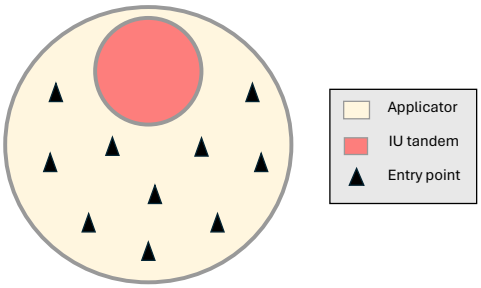

Figure 5.6: Illustration of the standardised entry region seen from below.

The needles are projected in their direction onto a plane at a matching height from the origin of the needle (green and purple). In this plane, the Hungarian method is used to minimise the overall squared distance from the projected needle points to the matched entry points [78]. The height of this plane is an important factor for obtaining the trade-off between channel curvature and collisions. This is visualised with an example in Figure 5.7. Here, two matching planes are visualised at different heights. As can be seen, the matching between the entry points (middle and right) and the needle segments (red and blue) changes by changing the height of the matching plane. A lower matching plane leads to lower curvature but more collisions and vice versa. The height of the matching plane was empirically determined to be in the middle of the entry region and the top plane.

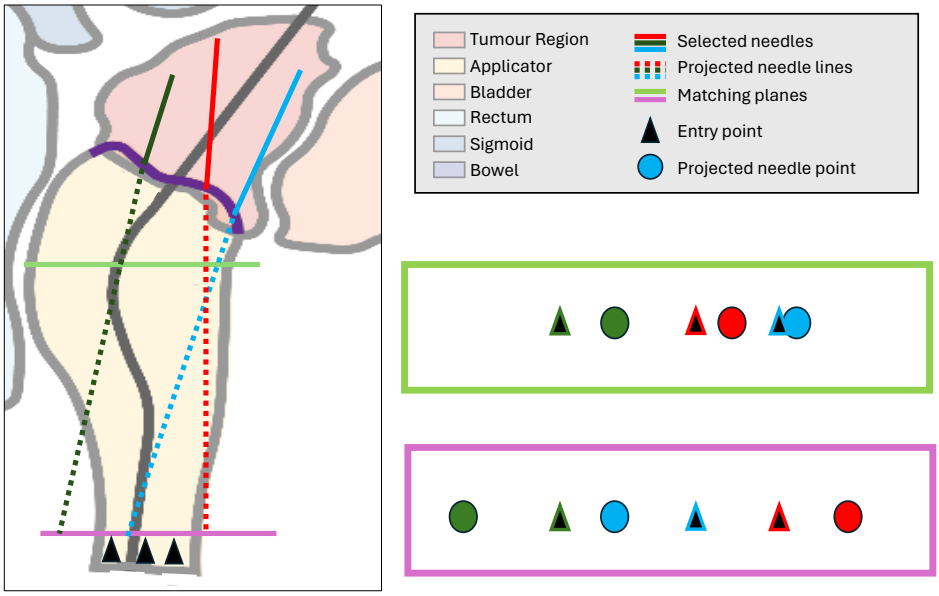

Figure 5.7: Visualisation of two example matching between entry points and needle segments with the matching algorithm. The needles are projected in their direction onto a plane at a matching height from the origin of the needle (green and purple). In this plane, the Hungarian method is used to minimise the overall squared distance from the projected needle points (circles) to the matched entry points (triangles). As can be seen, the height of the matching plane is very relevant as it can change the matching of entry points to needles. In the example the matchings of the blue and red needles are switched by changing the matching plane height (green and purple).

5.6. ITERATIVE REPLANNING

In the previous sections, all main steps of the source channel planning method proposed in this work are described. In the proposed method, these steps are used iteratively to obtain the optimal set of feasible source channels. This process is visualised in Figure 5.9.

For the sake of computational efficiency, path planning without considering collision constraints is used as initialisation for the path planning considering collision constraints. The paths are then optimised considering the aforementioned collision constraints and subsequently undergo verification through a brute force straight-line collision assessment. If all paths clear this verification step without any detected collisions the paths are approved. Conversely, if collisions are identified in instances where the rapid collision assessment failed to detect any, a more meticulous straight-line collision optimisation process is initiated. For computational efficiency this is only done if the fast collision checking method detected no collisions. This path optimisation process is visualised in Figure 5.8.

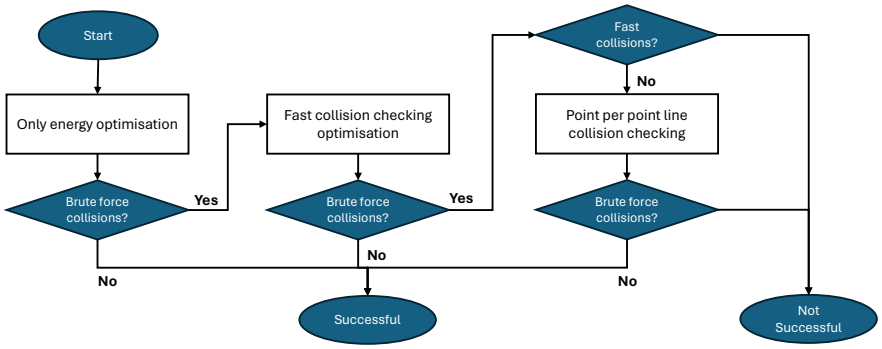

Figure 5.8: Activity diagram of the source channel paths optimisation algorithm.

Should collisions persist after this optimisation, the entry points of the conflicting needle pairs are switched and the path planning process is restarted. If the algorithm fails to find a feasible solution using these needles after N (= 3) restarts, more retries with the same needles are unlikely to lead to a feasible solution. Hence, the number of restarts is limited to N restarts. If no feasible source channels are found even after these restarts, a new set of needles is selected. In this set, needle pairs that have previously been in collision are not allowed to both be selected. Needles that have been in collision with the IU tandem are removed from the candidate set. If multiple collisions occur after the restarts, the maximum number of needles is reduced and a new set of needles is selected.

During the switching of colliding needles, the colliding needles switch their matched entry points. However, if a needle's entry point is already switched, the entry point can not be switched again. Otherwise, it would be possible that a needle's entry point is switched multiple times in a row and, in doing so, creates new collisions. Whereas switching two needles also resolves the other collisions. Not all collisions have to be resolved after the first switching step. If there are still collisions after the first switching step, these could be solved in the next switching step. Needles colliding with the IU tandem are moved to the free entry point with the lowest heuristic value. If the number of needles is decreased to below 1, the algorithm stops and no feasible paths are returned.

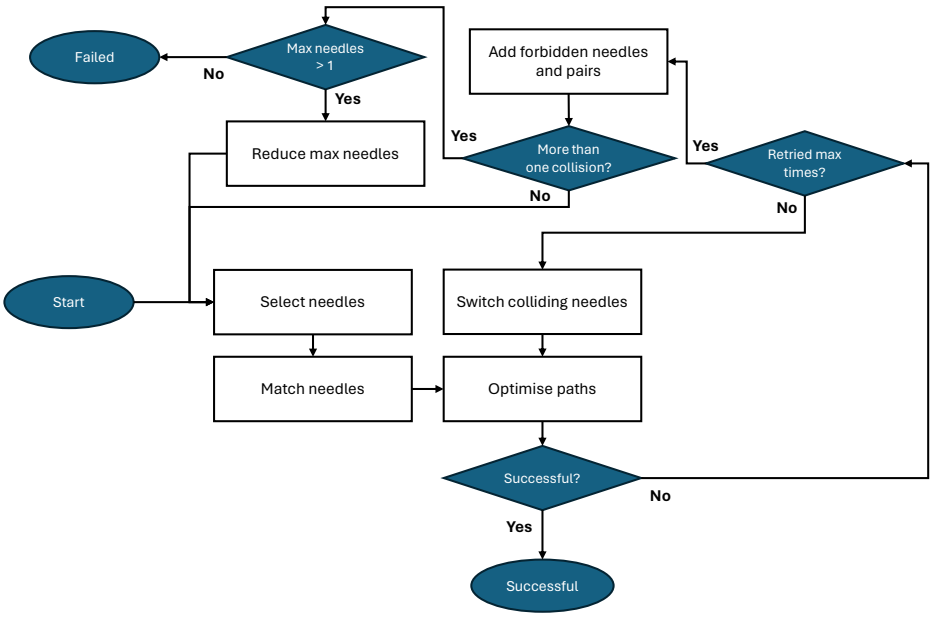

Figure 5.9: Activity diagram of the iterative optimisation of the simultaneous Bézier curve path planning algorithm.

6 COMPLEMENTARY RESULTS

In this chapter, extra results that are not presented in the paper but give valuable insights into the proposed method are presented. In Section 6.1, more results of the grid configurations are presented. In Section 6.2, more results of the ARCHITECT configurations are presented. Tables containing all treatment planning results for the patients receiving three and four fractions are shown in Section 6.3. A component-based analysis of the different components of the proposed method is presented in Section 6.4. Recommendations to improve the method are presented in Section 6.5.

6.1. GRID CONFIGURATION RESULTS

To obtain the high-potential dwell positions, BiCycle is used to create a treatment plan on a grid configuration. In Figure 6.1, a visualisation of the resulting treatment plan for patient 1 is shown. Here, the dwell positions in the grid configuration are shown in black, and the corresponding dwell time in the treatment plan is visualised in green.

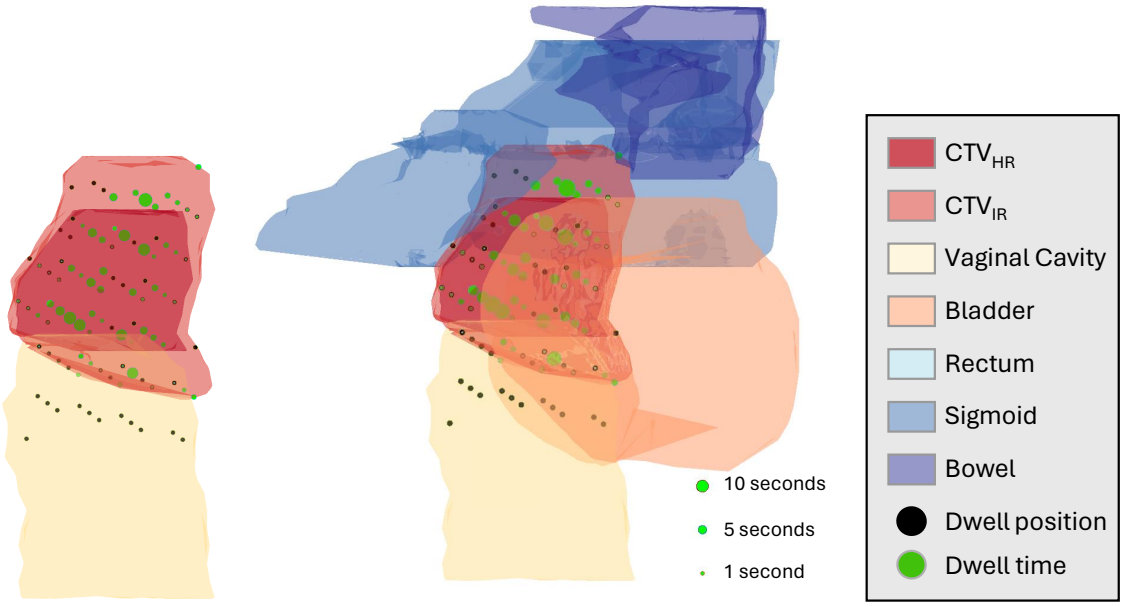

Figure 6.1: Visualisation of the treatment plan with the grid configuration for patient 1. All potential dwell positions are shown in black. The corresponding dwell time is visualised in green. The larger the diameter of the circle, the larger the dwell time. On the left, only the tumour region and the vaginal cavity is displayed. On the right, the OARs are also visualised.

The maximum dwell time in this grid configuration treatment plan was 21 seconds. In contrast, the treatment plan with the clinical configuration for this patient had a maximum dwell time of 26 seconds. This adds to the indication that the grid configuration has a preferred dose distribution over the clinical configuration as the dwell time is more homogeneous.

6.2. ARCHITECT CONFIGURATION

The proposed source channel planning algorithm found feasible solutions for all 22 patient cases. The generated ARCHITECT applicator for patient 1 is shown in Figure 6.2. The corresponding treatment plan is visualised in Figure 6.3.

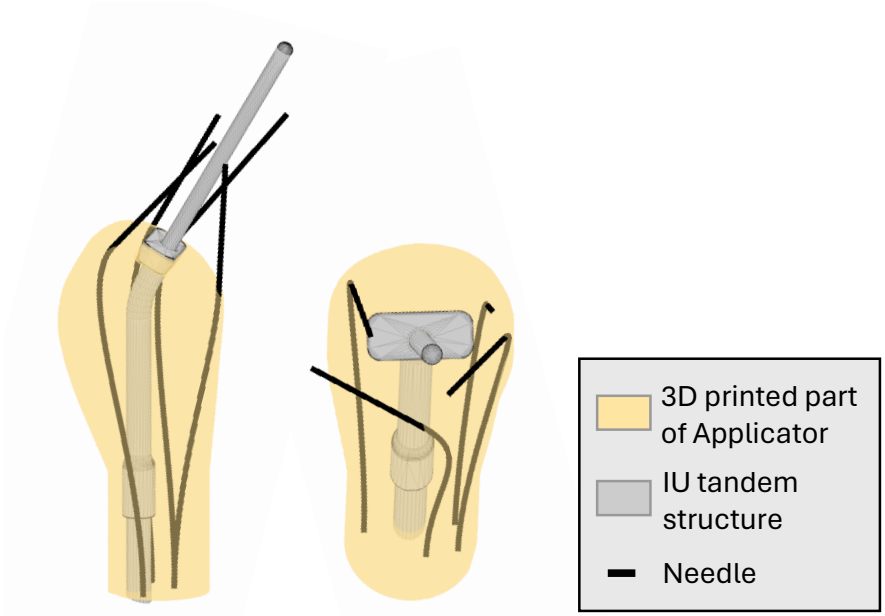

Figure 6.2: Patient-tailored applicator generated with the proposed method visualised from different angles.

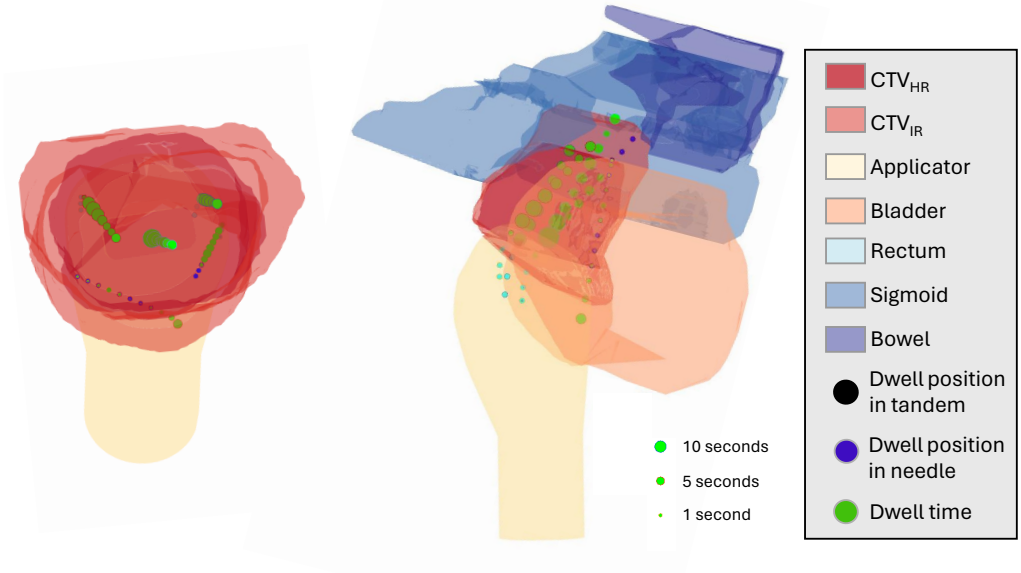

Figure 6.3: Visualisation of the treatment plan with the proposed ARCHITECT configuration for patient 1. The dwell times are visualised in green. The larger the diameter of the circle, the larger the dwell time. On the left, only the tumour region and the vaginal cavity is displayed. On the right, the OARs are also visualised.

As stated, the relevant DVH parameters do not fully describe the dose distribution. Hence, the dose distributions are also visualised on MRI slices. The conventional clinically used applicator has oblique needles pointing slightly away from the tandem and not reaching the appropriate depths. Hence, this applicator lacks superior coverage of the target volume. In Figure 6.4a, a resulting dose distribution on a superior axial slice of an MRI is shown. As can be seen, the lack of dwell positions results in a non-optimal coverage of the target volume. The resulting dose distribution with the proposed ARCHITECT applicator on the same slice is shown in Figure 6.4b. This applicator has multiple dwell positions in the superior region, allowing for better target volume coverage whilst decreasing the OAR dose.

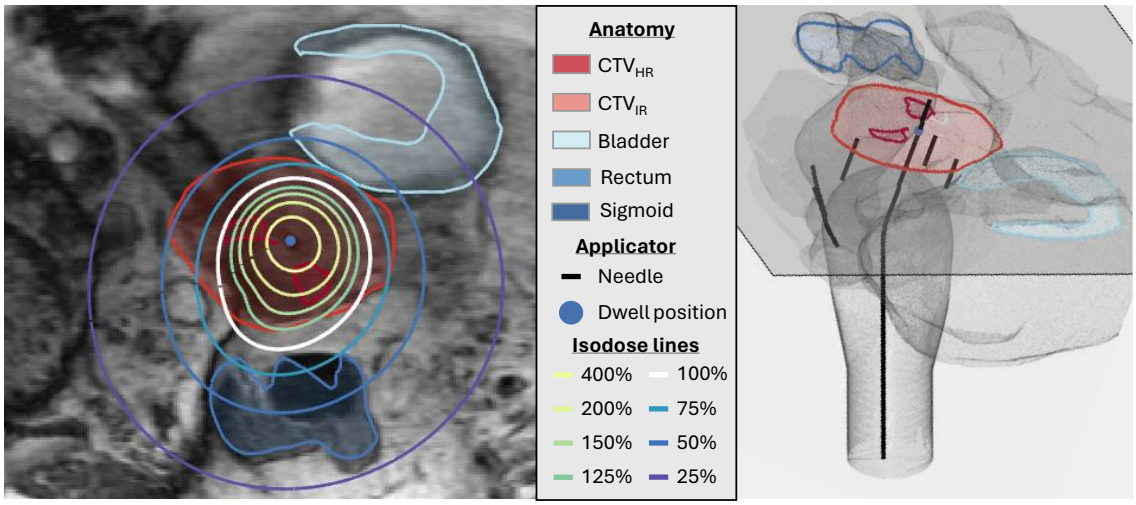

(a) The clinical configuration

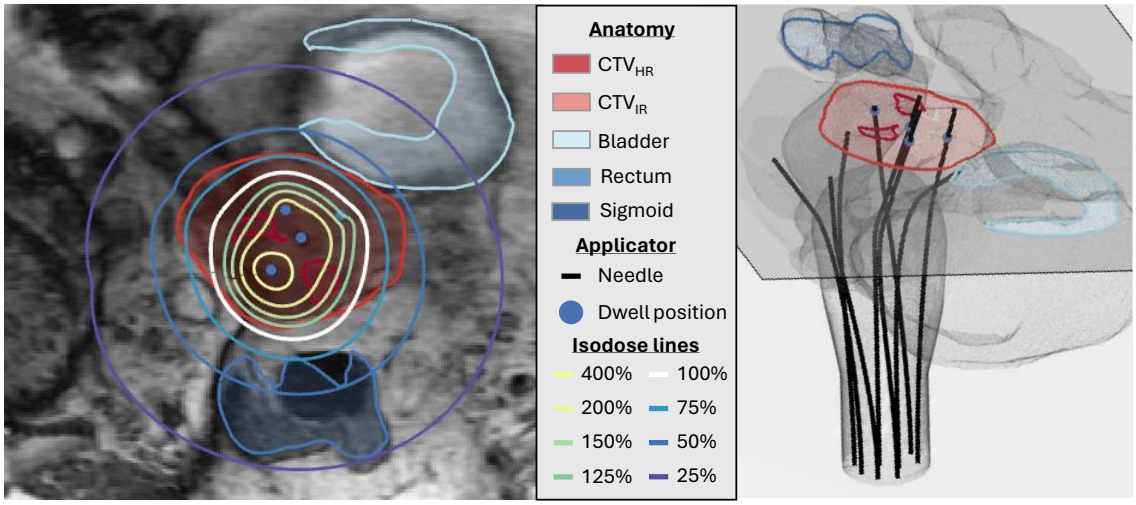

(b) The ARCHITECT configuration

Figure 6.4: Visualisation of dose distribution on a superior axial MRI slice obtained with the treatment plan with the clinical (a) and the ARCHITECT (b) configuration. On the right, the corresponding needle configuration is visualised in the 3D anatomy of the patient. The different clinically relevant volumes are also annotated on the slice height.

In Figure 6.5a and Figure 6.5b, the dose distribution on a lower axial slice of the MRI is displayed for the clinical and ARCHITECT configuration, respectively. The dose distribution with the ARCHITECT applicator is created with more dwell positions, and because the spread of the dwell points is better, the individual dwell points have lower dwell times, resulting in a larger dropoff in radiation. This can be observed in the distance between the 150% and the 100% isodose lines. This larger dropoff results in a lower OAR dose, which can be seen in the reduced overlap between the isodose lines and the delineated OARs. Moreover, the area receiving 400% of the prescribed dose is smaller with the ARCHITECT configuration, adding to the belief that a better spread of dwell positions can reduce hot spots.

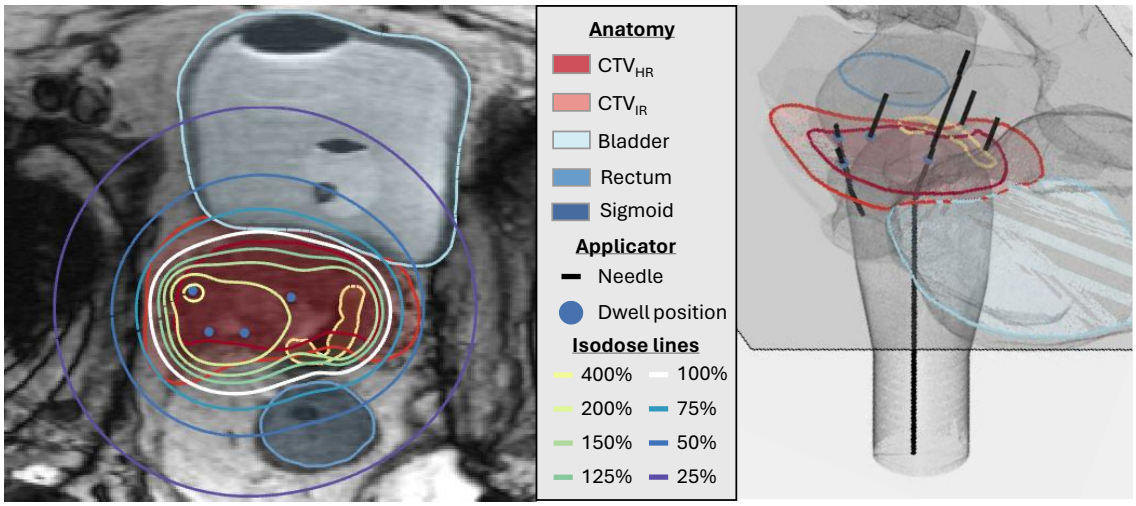

(a) The clinical configuration

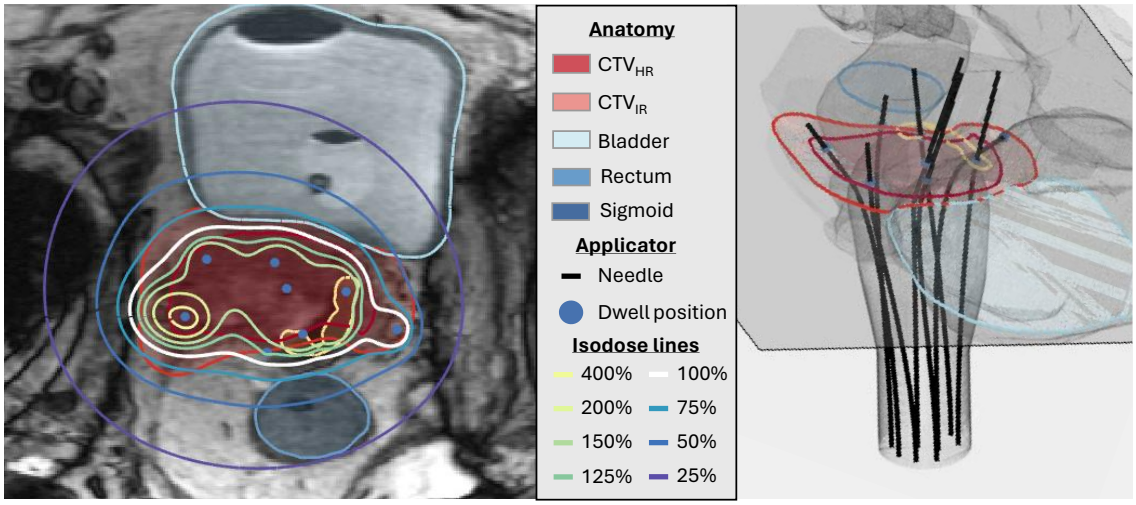

(b) The ARCHITECT configuration

Figure 6.5: Visualisation of dose distribution on an axial MRI slice obtained with the treatment plan with the clinical (a) and the ARCHITECT (b) configuration. On the right the corresponding needle configuration is visualised in the 3D anatomy of the patient. The different clinically relevant volumes are also annotated on the slice height.

6.3. ALL RESULTS

Table 6.1 and Table 6.2 show the mean, range, and p-value for the different parameters for all three configurations used in this work for patients receiving 3 and 4 fractions, respectively. The p-values for the grid and ARCHITECT configurations are evaluated using Wilcoxon signed rank tests using the clinical configurations as a comparison.

Table 6.1: Overall results for patients with three fractions for the different configurations.

	Clinical				ARCHITECT					Grid				
Parameter	**median**	**max**	**min**	**IQR**	**median**	**max**	**min**	**IQR**	**p-value**	**median**	**max**	**min**	**IQR**	**p-value**
CTV_{HR} D_{90} (Gy)	9.43	10.01	9.37	0.01	9.43	9.44	9.43	0.01	7.09e-1	9.56	9.59	9.51	0.02	6.15e-4
CTV_{HR} D_{98} (Gy)	7.80	8.20	6.48	0.56	7.47	8.17	7.13	0.67	4.45e-1	7.98	8.19	7.18	0.44	1.99e-1
CTV_{IR} D_{98} (Gy)	4.42	5.49	2.89	0.35	4.44	5.80	4.39	0.05	2.11e-1	4.65	5.13	4.43	0.12	2.15e-3
Bladder D_{2cm^3} (Gy)	6.46	7.45	4.10	1.61	6.17	7.12	4.05	1.41	7.79e-4	5.81	6.57	3.83	1.28	4.01e-5
Rectum D_{2cm^3} (Gy)	3.85	5.85	1.63	2.25	3.59	5.92	1.81	2.50	8.15e-3	3.06	5.63	1.64	2.58	6.08e-5
Sigmoid D_{2cm^3} (Gy)	3.99	5.92	1.08	1.48	4.18	5.93	1.19	2.01	8.58e-1	4.43	5.42	1.03	1.47	1.93e-3
Bowel D_{2cm^3} (Gy)	2.77	4.94	0.54	2.82	2.71	5.33	0.51	3.15	8.90e-3	2.68	5.11	0.46	2.68	5.30e-5
CTV_{HR} V_{100} (cm^3)	0.98	0.99	0.96	0.01	0.98	0.99	0.97	0.02	5.70e-1	0.99	0.99	0.97	0.01	1.15e-1
CTV_{HR} V_{150} (cm^3)	0.73	0.79	0.68	0.02	0.73	0.78	0.63	0.05	4.26e-1	0.64	0.71	0.55	0.08	5.30e-5
COIN (-)	0.65	0.37	0.88	0.15	0.73	0.44	0.85	0.19	2.62e-2	0.77	0.52	0.87	0.12	9.15e-5
Total dwelltime (s)	338	523	221	94	331	512	220	61	1.73e-3	299	431	218	68	4.01e-5
Number of needles (-)	4	2	6	2.00	5	4	7	1.25	2.64e-1	-	-	-	-	-

Table 6.2: Overall results for patients with four fractions for the different configurations.

	Clinical				ARCHITECT					Grid				
Parameter	**median**	**max**	**min**	**IQR**	**median**	**max**	**min**	**IQR**	**p-value**	**median**	**max**	**min**	**IQR**	**p-value**
CTV_{HR} D_{90} (Gy)	7.74	7.75	7.41	0.09	7.75	7.75	7.74	0.003	7.09e-1	7.86	7.87	7.84	0.02	6.15e-4
CTV_{HR} D_{98} (Gy)	6.47	6.73	5.84	0.86	6.36	6.61	5.97	0.50	4.45e-1	6.57	6.66	5.88	0.56	1.99e-1
CTV_{IR} D_{98} (Gy)	3.56	3.68	3.50	0.10	3.58	4.10	3.51	0.20	2.11e-1	3.77	3.98	3.58	0.13	2.15e-3
Bladder D_{2cm^3} (Gy)	5.96	6.08	5.44	0.47	5.43	6.28	4.93	0.54	7.79e-4	5.44	5.45	4.71	0.20	4.01e-5
Rectum D_{2cm^3} (Gy)	3.54	3.93	1.28	1.74	2.65	3.90	1.29	1.03	8.15e-3	2.06	3.07	1.07	1.10	6.08e-5
Sigmoid D_{2cm^3} (Gy)	4.71	4.97	3.37	0.73	4.47	4.70	3.42	0.46	8.58e-1	3.98	4.47	3.17	0.94	1.93e-3
Bowel D_{2cm^3} (Gy)	0.92	1.20	0.51	0.52	0.88	0.99	0.45	0.41	8.90e-3	0.79	0.89	0.44	0.34	5.30e-5
CTV_{HR} V_{100} (cm^3)	0.98	0.99	0.95	0.03	0.97	0.98	0.96	0.01	5.70e-1	0.98	0.98	0.96	0.02	1.15e-1
CTV_{HR} V_{150} (cm^3)	0.67	0.70	0.63	0.05	0.68	0.70	0.66	0.03	4.26e-1	0.50	0.53	0.47	0.05	5.30e-5
COIN (-)	0.62	0.60	0.68	0.06	0.73	0.59	0.78	0.10	2.62e-2	0.79	0.70	0.82	0.05	9.15e-5
Total dwelltime (s)	349	428	315	71	340	402	307	64	1.73e-3	298	319	265	27	4.01e-5
Number of needles (-)	4	2	6	2.00	5	4	7	1.25	2.64e-1	-	-	-	-	-

6.4. COMPONENT-BASED ANALYSIS OF THE PROPOSED METHODOLOGY

In this section, the different components of the proposed method are analysed. The components that are analysed are the candidate dwell point selection (Subsection 6.4.1), the needle selection (Subsection 6.4.2), the path planning algorithm (Subsection 6.4.3), and the IC dwell point placement (Subsection 6.4.4). Additionally, the runtime of the current implementation of the proposed method is analysed in Subsection 6.4.5.

6.4.1. CANDIDATE DWELL POINT SELECTION

The number of candidate dwell points selected to create the candidate set can influence the quality of the resulting treatment plan. In this work, the candidate dwell points are obtained by making use of BiCycle on a grid configuration. From the resulting treatment plan, the D_{max} dwell positions with the highest dwell time are selected as the candidate dwell positions. As the value of D_{max} is user-selected, an analysis of the effect of this value is conducted.

There are various ways in which the number of candidate dwell points can influence the resulting dose conformity. Some of these stem from the set cover formulation requirement that all candidate dwell points must be covered at least once. Consequently, if a candidate dwell point is positioned close to an OAR, the selected candidate needles are likely to be closer to the OAR as well, increasing the probability of over-radiating the OAR. Furthermore, if a candidate dwell point is challenging to reach while adhering to all needle constraints, it will be sparsely covered by needles in the candidate set. This underrepresentation might lead to a greater cover distance, possibly resulting in lower dose conformity. Conversely, utilising too few candidate dwell points might lead to a set of candidate dwell points not properly representing the resolution optimal dose distribution, potentially leading to regions of the CTV not being radiated properly.

To analyse the effect of the number of candidate dwell points, a candidate set is created for different values of D_{max}. From this candidate set, the optimal needles are selected using the set cover problem formulation proposed in this work. In this analysis, no path-planning steps are performed. The selected needles are used directly to create the configuration on which BiCycle is used to do the dwell time optimisation. The original ovoid dwell positions from the clinical configuration are used as IC points to ensure that inferior coverage is not compromised in this analysis. The different values for D_{max} that have been tested are 30, 35, 40 and 45.

The results of the treatment optimisations for the different values of D_{max} are shown in Table 6.3. As can be observed, the number of candidate dwell points used to create the candidate set influenced the number of planning aims that were met. For every patient, the number of planning aims that were met is the highest with the candidate set created based on 35 candidate dwell points. Consequently, D_{max} is selected to be 35 in this work.

Table 6.3: Results of the treatment optimisations with BiCycle on the configurations with different numbers of candidate dwell points ($D_{\max}$). The configurations are created based on the $D_{\max}$ dwell points with the highest dwell time from the grid configuration. These dwell points are used to create a candidate set from which the optimal needles are selected, making use of the set cover formulation. The selected needles are used directly to create the configuration without performing path planning. CD stands for cover distance.

	Clinical		D_{max} = 30			D_{max} = 35			D_{max} = 40			D_{max} = 45		
Patient	**Needles**	**Aims met**	**CD**	**Needles**	**Aims met**	**CD**	**Needles**	**Aims met**	**CD**	**Needles**	**Aims met**	**CD**	**Needles**	**Aims met**
1	4	5/7	7	10	6/7	8	10	6/7	8	10	6/7	10	8	6/7
2	5	7/7	11	6	7/7	9	9	7/7	10	10	7/7	13	6	7/7
3	6	6/7	9	7	7/7	10	6	6/7	10	8	5/7	10	6	5/7
4	4	7/7	8	8	7/7	8	8	7/7	8	8	7/7	8	8	7/7
5	5	4/7	9	9	4/7	10	9	5/7	10	9	5/7	10	10	5/7
6	3	5/7	9	10	7/7	9	10	7/7	9	9	7/7	9	9	7/7
7	4	3/7	11	10	7/7	12	10	7/7	10	7	7/7	16	4	6/7
8	4	3/7	10	9	7/7	11	8	7/7	11	7	7/7	14	5	7/7
9	4	3/7	10	5	5/7	10	6	5/7	10	7	5/7	19	3	3/7
10	5	6/7	9	7	7/7	9	7	7/7	10	9	7/7	12	6	7/7
11	4	7/7	9	7	7/7	9	7	7/7	9	9	7/7	9	9	7/7
12	6	4/7	12	8	6/7	10	8	7/7	10	7	6/7	10	7	6/7
13	3	7/7	8	8	7/7	8	10	7/7	10	7	7/7	10	8	7/7
14	6	7/7	8	9	7/7	9	10	7/7	9	9	7/7	10	8	7/7
15	6	7/7	8	9	7/7	8	9	7/7	10	7	6/7	10	7	6/7
16	3	7/7	7	5	7/7	8	8	7/7	9	10	7/7	9	10	7/7
17	6	6/6	7	10	6/6	8	8	6/6	10	7	6/6	10	9	6/6
18	6	4/6	9	9	6/6	8	10	6/6	10	7	6/6	26	2	1/6
19	4	5/6	8	8	5/6	8	8	5/6	11	9	4/6	10	10	5/6
20	2	7/7	10	10	7/7	10	10	7/7	10	7	7/7	9	9	7/7
21	4	4/7	10	10	6/7	10	10	6/7	20	4	5/7	32	2	5/7
22	6	5/7	8	10	5/7	10	10	6/7	10	7	6/7	15	4	5/7

6.4.2. NEEDLE SELECTION ALGORITHM

The quality of the needle selection is crucial for the resulting dose conformity. Hence, the working of the needle selection algorithm is tested extensively. Firstly, the ability to recreate clinical needles based on the clinical dwell positions is tested. Secondly, the dose conformity of the configuration obtained by only using the set cover formulation is analysed.

When using the clinical dwell points as input for the needle selection algorithm, the algorithm should return the clinically used needles. No extra needles should be placed, and all dwell points should be covered exactly. In Figure 6.6, the selected needles based on clinical dwell points can be seen. As observed, the selected needles cover all dwell points precisely, meaning the algorithm successfully passed the test.

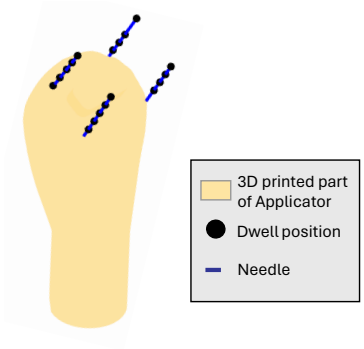

Figure 6.6: Visualisation of the selected needles (blue) by the proposed method based on the original clinical dwell points (black).

The effectiveness of the set cover problem in selecting a needle set that leads to good dose conformity is evaluated. To this end, the selected needle set by the set cover formulation is directly used to create a treatment configuration. The original ovoid dwell positions from the clinical configuration are used as IC points in this configuration. The differences in fraction doses for the clinical and the set cover configuration per patient per dosimetric index are shown in Figure 6.7. The resulting treatment plans obtained clinically feasible treatment plans that met 5 fewer planning aims than the treatment plans with the grid configurations. As losing dose conformity due to the needle feasibility constraints is unavoidable, the weighted set cover approach is believed to be valid.

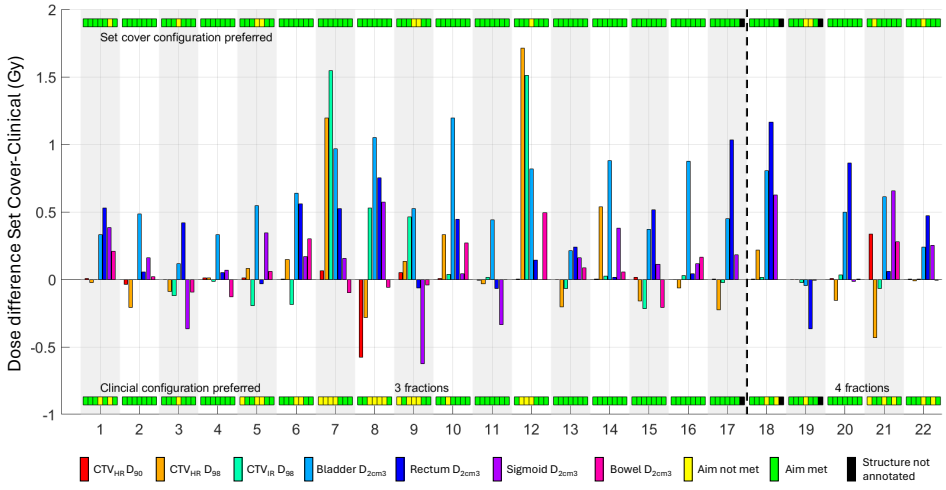

Figure 6.7: Bar chart showing the differences between the relevant DVH parameters from the treatment plans obtained with the clinical and the set cover configuration. Bars above the x-axis indicate that the set cover configuration obtained a preferred dose for that volume, whereas bars below the x-axis indicate that the clinical configuration obtained the preferred dose. Planning aims not being met are indicated by the yellow blocks, and aims being met are indicated by the green blocks. If the structure was not annotated in the structure set, it is indicated by a black box. The patients receiving three fractions are shown on the left of the vertical black dotted line, and the patients receiving four fractions are plotted on the right of this line.

Even though the set cover approach is believed to be valid, possible improvements can still be made. Several patients in the patient cohort have vaginal extensions of the target volumes. The candidate set created for these patients might have candidate dwell points that are sparsely covered by candidate needles in the candidate set. Sparsely covered candidate dwell points are candidate dwell points that are not covered by a lot of needles within a small coverage distance. The requirements used in this work, like the requirement on tissue insertion angle, make the candidate dwell points of the vaginal extension difficult to cover. Furthermore, in this work, potential needles are only added to the candidate set if all constraints are met and are directly discarded otherwise. In order to prevent the sparse points from leading to a large coverage distance in the adaptive algorithm and, therefore, to the selection of non-optimal needles, extra candidate needle segments can be added to cover the sparse dwell positions. These extra candidate needle segments are called sparse point needles.

These sparse point candidate needles are generated through different steps. Firstly, the sparse candidate dwell positions are identified. Any candidate dwell position not covered by at least ten candidate needles in the candidate set, using a coverage distance of 6 mm, is considered a sparse point. Secondly, for each sparse point, random needles are sampled towards the nearest part of the applicator. The sampled needles are added to the candidate set if all constraints are met. Lastly, for groups of sparse points, needles are similarly sampled and added to the candidate set, provided all constraints are met. An example candidate set with sparse point needles is shown in Figure 6.8. In this Figure, there are 4 sparse dwell positions, denoted with the pink circles. As can be seen, all sparse dwell positions are indeed in the vaginal extension of the tumour. The extra sparse candidate needles that are added to the candidate set are shown in red. The original candidate set size and the number of sparse point needles added to cover the sparse points for every patient are displayed in Table 6.4.

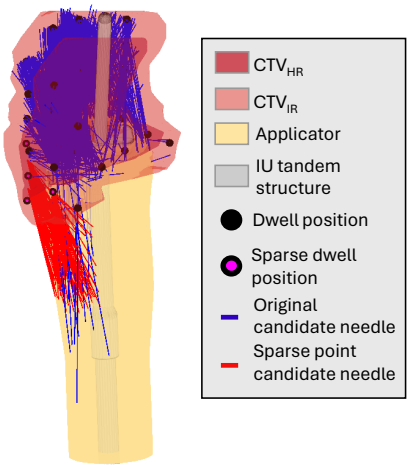

Figure 6.8: Visualisation of an example candidate set with added needles for sparsely covered dwell positions. The dwell positions are denoted with black circles, and a sparse dwell position is denoted with a pink circle. The original candidate needles are visualised in blue, and the needles added to cover the sparse dwell positions are shown in red.

Table 6.4: Table showing the original candidate set size and the number of sparse point needles added to cover the sparse points.

Patient	**1**	**2**	**3**	**4**	**5**	**6**	**7**	**8**	**9**	**10**	**11**
Number of sparse point needles	58	80	16	0	40	0	80	40	0	39	42
Original candidate set size	1656	2305	1281	2406	1607	2188	2555	2314	2554	2273	1906
Patient	**12**	**13**	**14**	**15**	**16**	**17**	**18**	**19**	**20**	**21**	**22**
Number of sparse point needles	200	0	40	58	0	40	0	120	40	65	0
Original candidate set size	1445	1817	2113	1982	1953	2431	2993	2690	1761	2884	1993

The maximum number of sparse point needles that are added for the patients in the current patient cohort is 200. Considering that the total number of candidate needles in the original candidate set is between 1817 and 2993 for this patient cohort, the candidate set size increase due to adding sparse point needles is not large. Therefore, if the addition of this limited number of needles increases the dose conformity, the addition is considered to be desired.

The set cover configurations with the addition of sparse point needles obtain the results shown in Figure 6.9 when compared to the clinical configurations. As can be seen, the addition of the sparse points only increased the dose conformity of the resulting treatment plan for patient 19, compared to the set cover configuration without sparse point needles. Hence, the additional sparse needles are not added to the standard candidate set. It should be noted that in this test, only one needle is needed to cover a dwell point, as all selected needles are directly accepted. In the real ARCHITECT configuration with source channel planning, straight needle segments might not lead to feasible source channel paths and thus be rejected. Consequently, having extra needles to cover the sparse points might become beneficial.

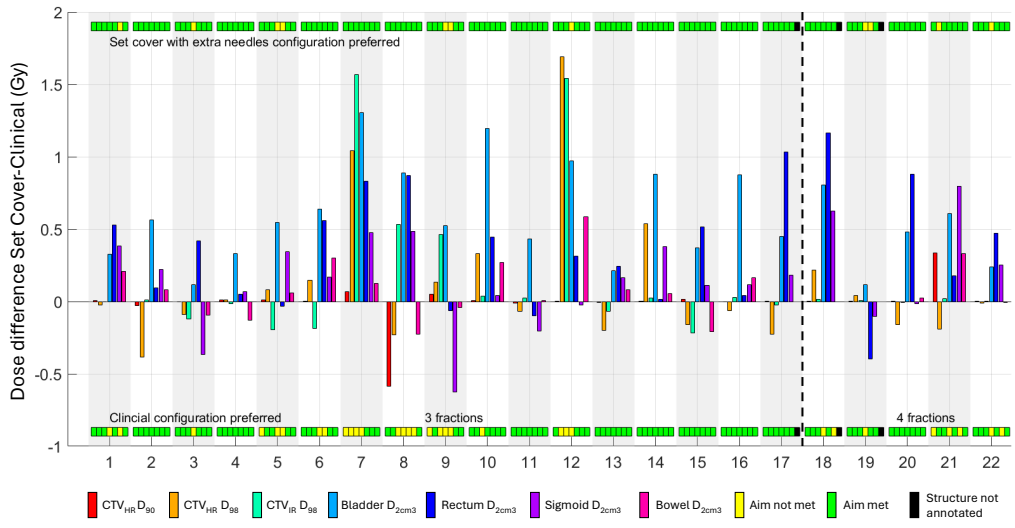

Figure 6.9: Bar chart showing the differences between the relevant DVH parameters from the treatment plans obtained with the clinical configuration and the set cover configuration with extra needles for the sparse points. Bars above the x-axis indicate that the set cover configuration obtained a preferred dose for that volume, whereas bars below the x-axis indicate that the clinical configuration obtained the preferred dose. Planning aims not being met are indicated by the yellow blocks, and aims being met are indicated by the green blocks. If the structure was not annotated in the structure set, it is indicated by a black box. The patients receiving three fractions are shown on the left of the vertical black dotted line, and the patients receiving four fractions are plotted on the right of this line.

6.4.3. TANDEM COLLISIONS

The proposed iterative simultaneous path planning algorithm plans source channel paths from the straight needle segments to the corresponding entry points. These paths are only deemed feasible if all paths remain within the applicator, are not in collision with each other, and are not in collision with the IU tandem structure. The current matching heuristic obtains a tradeoff between the curvature of the source channels and the number of inter-source channel collisions. The heuristic does not take collisions with the IU tandem into account. A different heuristic taking these collisions into account might result in fewer rejected sets of needles and consequently lead to higher dose conformity. The loss in dose conformity due to tandem collisions in the proposed method is investigated to get an estimate of the benefit of a matching algorithm that prevents IU tandem collisions. This analysis is performed by creating the ARCHITECT configuration with the proposed method, only without the IU tandem distance constraints. In the comparison with the full ARCHITECT configuration, the losses due to the tandem collisions can be observed.

In Figure 6.10, the differences between the relevant DVH parameters from the treatment plans obtained with the clinical and the ARCHITECT configurations without taking tandem collisions into account are shown. The total amount of planning aims not being met was equal with and without the tandem collisions. However, for almost all planning aims that are not met, the resulting treatment plan with the ARCHITECT configuration without tandem collisions obtained a preferable dose over the treatment plan with the ARCHITECT configuration with tandem collisions. Therefore, the method could benefit from an adaptation that leads to fewer sets of needles being rejected due to tandem collisions.

The rejection of some needle sets due to infeasibility is unavoidable; however, if fewer sets are rejected, the resulting dose conformity will be closer to pure set cover configuration dose conformity. The rematching of needles already ensures fewer sets of needles are rejected due to infeasibility, but even fewer rejected sets would improve the dose conformity even more. The current matching heuristic only considers distance and does not consider potential tandem collisions. A different heuristic taking into account potential collisions with the IU tandem structure might be beneficial.

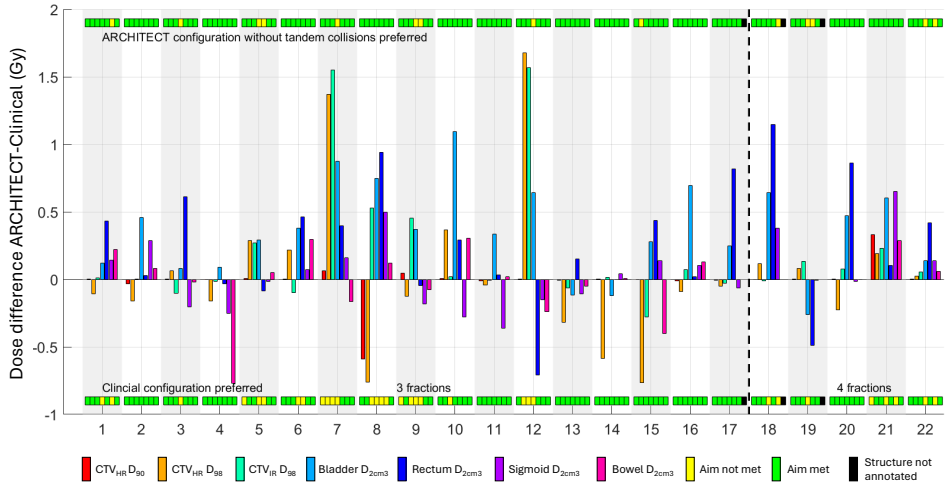

Figure 6.10: Bar chart showing the differences between the relevant DVH parameters from the treatment plans obtained with the clinical and the ARCHITECT configuration without taking tandem collisions into account. Bars above the x-axis indicate that the set cover configuration obtained a preferred dose for that volume, whereas bars below the x-axis indicate that the clinical configuration obtained the preferred dose. Planning aims not being met are indicated by the yellow blocks, and aims being met are indicated by the green blocks. If the structure was not annotated in the structure set, it is indicated by a black box. The patients receiving three fractions are shown on the left of the vertical black dotted line, and the patients receiving four fractions are plotted on the right of this line.

6.4.4. IC DWELL POINT PLACEMENT

As stated, all straight needle segments selected in the current work are IS needles. The IC dwell positions used in the ARCHITECT configuration are placed on the curved source channel paths optimised by the simultaneous path planner. The path planner does not optimise the position of the IC dwell positions, hence their quality needs to be checked. To evaluate the quality of these IC dwell positions, the resulting dose conformity is compared to a theoretical treatment plan that retains the original ovoid IC positions. Although these original positions are not feasible in combination with the selected needles, this comparison serves as a benchmark to assess the quality of the adapted IC dwell positions. If the quality of the current IC dwell positions is not sufficient, extra IC channels can be added to the configuration to increase the IC radiation possibility and, thereby, the dose conformity.

In Figure 6.11, the differences in relevant DVH parameters between the treatment plans obtained with the clinical configuration and the ARCHITECT configuration using the original ovoid points are shown, As can be seen, using the original ovoid dwell positions increased dose conformity for several patients. This suggests that adding extra IC source channels might improve the quality of the IC dwell positions and, consequently, increase dose conformity.

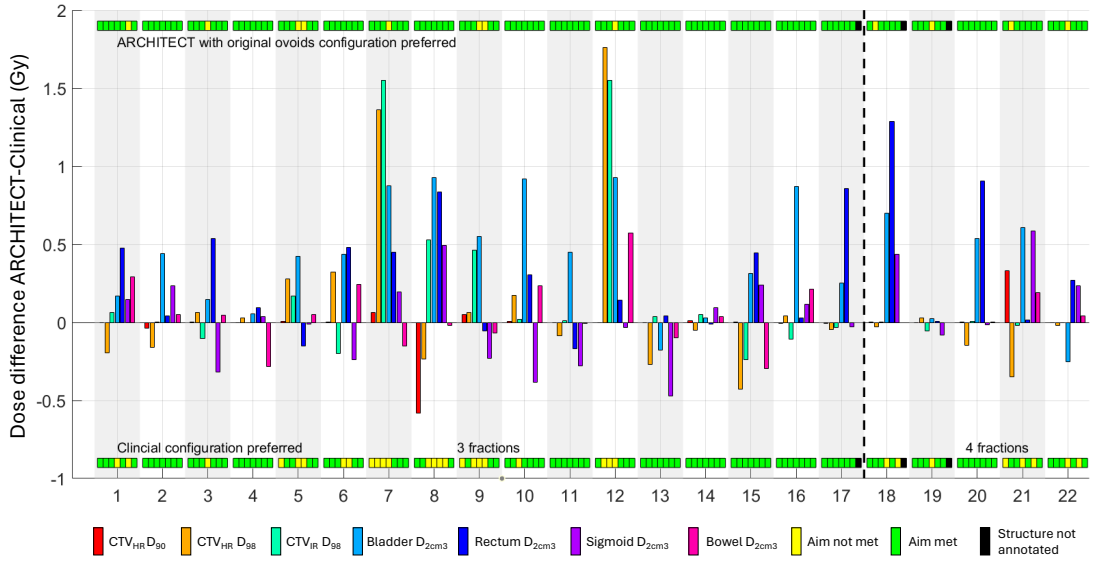

Figure 6.11: Bar chart showing the differences between the relevant DVH parameters from the treatment plans obtained with the clinical configuration and the ARCHITECT configuration with the original ovoid points. Bars above the x-axis indicate that the ARCHITECT configuration obtained a preferred dose for that volume, whereas bars below the x-axis indicate that the clinical configuration obtained the preferred dose. Planning aims not being met are indicated by the yellow blocks, and aims being met are indicated by the green blocks. If the structure was not annotated in the structure set, it is indicated by a black box. The patients receiving three fractions are shown on the left of the vertical black dotted line, and the patients receiving four fractions are plotted on the right of this line.

6.4.5. RUNTIME ANALYSIS

The runtime of the algorithm is analysed to identify potential parts of the algorithm that would need speeding up. The runtimes of the different parts of the algorithm for the different patients in the patient cohort are shown in Figure 6.12.

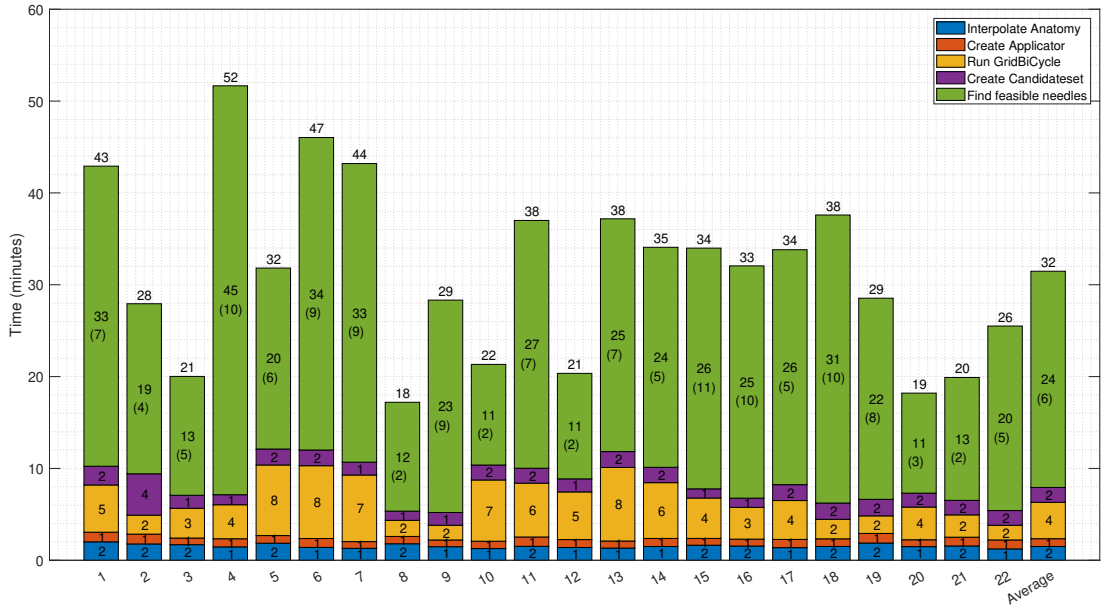

Figure 6.12: Bar chart showing the runtimes for the different parts of the proposed methodology per patient in the patient cohort. The runtimes in minutes are also inside the bars and the total runtime is displayed on top of the bars. In between the brackets, the number of times the iterative path planner is restarted on a different matching or needle selection is displayed.

The average runtime of the current implementation of the proposed method was 32 minutes, with a maximum of 52 minutes, indicating that it is already within a clinically feasible runtime range. However, there is potential to further reduce this runtime, for example, by more extensively parallelising the calculations. The most time-consuming step is the needle selection and the generation of the corresponding paths. The needle selection process is repeated until the simultaneous path planning algorithm finds feasible source channels for all selected needles. The median number of times the path optimisation algorithm was restarted is six times. As can be observed, more restarts were related to longer runtimes. Consequently, a reduction in runtime can be achieved by increasing the success probability of the path planner on the initially selected needles. This could involve incorporating additional needle checks, only allowing needles with high path-planning success probability in the candidate set, or adapting the matching heuristic to reduce the number of collisions.

6.5. RECOMMENDATIONS

Based on the component-based analysis of the proposed methodology different areas of improvement are identified. There are three recommended areas of improvement: i) the IC dwell positions, ii) the IU tandem collision avoidance and iii) the candidate dwell point selection. The recommended areas of improvement, together with suggested improvement approaches, are described below.

The use of the original ovoid dwell positions in the ARCHITECT configuration has demonstrated that the quality of the IC dwell point can be improved. The addition of extra IC dwell positions can lead to improvement in dose conformity. Extra IC source channels can be created by random sampling [9]. By adding biased sampling towards the vaginal extensions, a possibly higher target dose can be achieved.

The analysis of the effect of the IU tandem collisions in the proposed source channel path planning method shows that the IU tandem collisions lead to losses in dose conformity compared to the set cover configuration. Even though rejections due to these collisions are unavoidable, fewer rejections lead to better dose conformity. Using a different heuristic, taking into account potential collisions with the IU tandem structure, might be beneficial. Possible approaches could use the minimum energy

curves for all possible matching combinations, with a heuristic that increases the cost of needles in collision [79], or increases the score in the case of neighbouring paths [80]. In this case, increasing the score of a match in which the minimum energy curve is in collision with the IU tandem or increasing the score of entry points close to the IU tandem. Besides adapting the matching heuristic, collisions with the IU tandem can also be prevented by adding repelling points in the IU tandem structure [70]. The repelling points increase the energy of nearby paths, increasing the distance between the needles and the IU tandem structure.

The current method to obtain candidate dwell positions uses BiCycle on an equally spaced grid. In this study, the grid resolution and placement are not varied. Research has shown that the step size between dwell positions plays a significant role in the dose conformity for HDR-BT for the prostate [81]. Moreover, the grid spacing and placement also affect the optimisation time and convergence of BiCycle, as, for example, more points lead to a longer optimisation time. In a study (data not shown), the 10 mm grid spacing was found to lead to good biasing of the needles while still leading to reasonable optimisation times. Besides varying the standard grid spacing, random perturbations and a circular pattern might also be beneficial. A weighted combination of multiple sparse grids is also an option to be considered. Additionally, the D_{max} dwell positions in the target volume with the highest dwell time according to the grid configuration treatment plan are used. This number is empirically determined to be 35 based on the candidate dwell point selection analysis. The amount of dwell positions selected could be made relative to the size of the clinical target volume.

REFERENCES

[1] F. Bray, J. Ferlay, I. Soerjomataram, R. L. Siegel, L. A. Torre, and A. Jemal, "Global cancer statistics 2018: Globocan estimates of incidence and mortality worldwide for 36 cancers in 185 countries," *CA: a cancer journal for clinicians*, vol. 68, pp. 394–424, 11 2018. [Online]. Available: https://pubmed-ncbi-nlm-nih-gov.tudelft.idm.oclc.org/30207593/

[2] H. Sung, J. Ferlay, R. L. Siegel, M. Laversanne, I. Soerjomataram, A. Jemal, and F. Bray, "Global cancer statistics 2020: Globocan estimates of incidence and mortality worldwide for 36 cancers in 185 countries," *CA: A Cancer Journal for Clinicians*, vol. 71, pp. 209–249, 5 2021. [Online]. Available: https://onlinelibrary.wiley.com/doi/full/10.3322/caac.21660https://onlinelibrary.wiley.com/doi/abs/10.3322/caac.21660https://acsjournals.onlinelibrary.wiley.com/doi/10.3322/caac.21660

[3] D. Cibula, R. Pötter, F. Planchamp, E. Avall-Lundqvist, D. Fischerova, C. Haie-Meder, C. Köhler, F. Landoni, S. Lax, J. C. Lindegaard, U. Mahantshetty, P. Mathevet, W. G. McCluggage, M. McCormack, R. Naik, R. Nout, S. Pignata, J. Ponce, D. Querleu, F. Raspagliesi, A. Rodolakis, K. Tamussino, P. Wimberger, and M. R. Raspollini, "The european society of gynaecological oncology/european society for radiotherapy and oncology/european society of pathology guidelines for the management of patients with cervical cancer," *Virchows Archiv*, vol. 472, pp. 919–936, 6 2018. [Online]. Available: https://link.springer.com/article/10.1007/s00428-018-2362-9

[4] L. Fokdal, A. Sturdza, R. Mazeron, C. Haie-Meder, L. T. Tan, C. Gillham, B. Šegedin, I. Jürgenliemk-Schultz, C. Kirisits, P. Hoskin, R. Pötter, J. C. Lindegaard, and K. Tanderup, "Image guided adaptive brachytherapy with combined intracavitary and interstitial technique improves the therapeutic ratio in locally advanced cervical cancer: Analysis from the retroembrace study," *Radiotherapy and Oncology*, vol. 120, pp. 434–440, 9 2016.

[5] C. Kirisits, S. Lang, J. Dimopoulos, D. Berger, D. Georg, and R. Pötter, "The vienna applicator for combined intracavitary and interstitial brachytherapy of cervical cancer: design, application, treatment planning, and dosimetric results," *International journal of radiation oncology, biology, physics*, vol. 65, pp. 624–630, 6 2006. [Online]. Available: https://pubmed-ncbi-nlm-nih-gov.tudelft.idm.oclc.org/16690444/

[6] M. Oud, "Automated multi-criterial treatment planning for adaptive high-dose-rate brachytherapy for locally advanced cervical cancer," 2019.

[7] M. Serban, C. Kirisits, A. de Leeuw, R. Pötter, I. Jürgenliemk-Schulz, N. Nesvacil, J. Swamidas, R. Hudej, G. Lowe, T. P. Hellebust, G. Menon, A. Oinam, P. Bownes, B. Oosterveld, M. D. Brabandere, K. Koedooder, A. B. L. Marthinsen, D. Whitney, J. Lindegaard, and K. Tanderup, "Ring versus ovoids and intracavitary versus intracavitary-interstitial applicators in cervical cancer brachytherapy: Results from the embrace i study," *International journal of radiation oncology, biology, physics*, vol. 106, pp. 1052–1062, 4 2020. [Online]. Available: https://pubmed.ncbi.nlm.nih.gov/32007365/

[8] R. C. Laan, R. A. Nout, J. Dankelman, and N. J. van de Berg, "Mri-driven design of customised 3d printed gynaecological brachytherapy applicators with curved needle channels," *3D Printing in Medicine*, vol. 5, 12 2019.

[9] R. Straathof, S. van Vliet-Pérez, I.-K. K. Kolkman-Deurloo, L. S. Wauben, R. A. Nout, B. J. Heijmen, L. Rossi, J. Dankelman, and N. J. van de Berg1, "Automated planning of curved source channels in 3d-printed patient-tailored applicators for cervical cancer brachytherapy," *[TO BE PUBLISHED]*, 2024.

[10] L. Eapen, C. Kayser, Y. Deshaies, G. Perry, C. E, C. Morash, J. E. Cygler, D. Wilkins, and S. Dahrouge, "Correlating the degree of needle trauma during prostate brachytherapy and the development of acute urinary toxicity," *International Journal of Radiation Oncology Biology Physics*, vol. 59, pp. 1392–1394, 8 2004. [Online]. Available: https://pubmed-ncbi-nlm-nih-gov.tudelft.idm.oclc.org/15275724/

[11] S. Anbumani, N. A. Nambiraj, S. Dayalan, K. Ganesh, P. Anchineyan, and R. S. Bilimagga, "A brachytherapy plan evaluation tool for interstitial applications," *Advances in Bioinformatics*, vol. 2014, pp. 1–6, 2 2014. [Online]. Available: /pmc/articles/PMC3934649//pmc/articles/PMC3934649/?report=abstracthttps://www-ncbi-nlm-nih-gov.tudelft.idm.oclc.org/pmc/articles/PMC3934649/

[12] B. Sanchez-Nieto and A. E. Nahum, "Bioplan: software for the biological evaluation of radiotherapy treatment plans," *Medical Dosimetry*, vol. 25, pp. 71–76, 3 2000.

[13] S. Pokharel, S. Rana, J. Blikenstaff, A. Sadeghi, and B. Prestidge, "Evaluation of hybrid inverse planning and optimization (hipo) algorithm for optimization in real-time, high-dose-rate (hdr) brachytherapy for prostate," *Journal of Applied Clinical Medical Physics*, vol. 14, pp. 96–107, 7 2013. [Online]. Available: https://onlinelibrary-wiley-com.tudelft.idm.oclc.org/doi/full/10.1120/jacmp.v14i4.4198https://onlinelibrary-wiley-com.tudelft.idm.oclc.org/doi/abs/10.1120/jacmp.v14i4.4198https://aapm-onlinelibrary-wiley-com.tudelft.idm.oclc.org/doi/10.1120/jacmp.v14i4.4198

[14] M. Oud, I. K. Kolkman-Deurloo, J. W. Mens, D. Lathouwers, Z. Perkó, B. Heijmen, and S. Breedveld, "Fast and fully-automated multi-criterial treatment planning for adaptive hdr brachytherapy for locally advanced cervical cancer," *Radiotherapy and Oncology*, vol. 148, pp. 143–150, 7 2020.

[15] L. Beaulieu, H. Al-Hallaq, B. S. Rosen, and D. J. Carlson, "Multicriteria optimization in brachytherapy," *International Journal of Radiation Oncology Biology Physics*, vol. 114, pp. 177–180, 10 2022. [Online]. Available: http://www.redjournal.org/article/S0360301622004746/fulltexthttp://www.redjournal.org/article/S0360301622004746/abstracthttps://www.redjournal.org/article/S0360-3016(22)00474-6/abstract

[16] S. C. Maree, N. H. Luong, E. S. Kooreman, N. van Wieringen, A. Bel, K. A. Hinnen, H. Westerveld, B. R. Pieters, P. A. Bosman, and T. Alderliesten, "Evaluation of bi-objective treatment planning for high-dose-rate prostate brachytherapy-a retrospective observer study," *Brachytherapy*, vol. 18, pp. 396–403, 5 2019. [Online]. Available: https://pubmed.ncbi.nlm.nih.gov/30718176/

[17] "Prescribing, recording, and reporting brachytherapy for cancer of the cervix:," *Journal of the ICRU*, vol. 13, pp. NP.1–NP, 4 2013.

[18] S. S. Patankar, A. I. Tergas, I. Deutsch, W. M. Burke, J. Y. Hou, C. V. Ananth, Y. Huang, A. I. Neugut, D. L. Hershman, and J. D. Wright, "High versus low-dose rate brachytherapy for cervical cancer," *Gynecologic Oncology*, vol. 136, pp. 534–541, 3 2015.

[19] K. Fjellanger, "Treatment planning for external beam radiation therapy with simultaneous integrated lymph node boost in cervical cancer," 2018.

[20] S. M. V. Vliet-Pérez, R. V. Paassen, L. S. G. L. Wauben, R. Straathof, N. J. V. D. Berg, J. Dankelman, B. J. M. Heijmen, I.-K. K. Kolkman-Deurloo, and R. A. Nout, "Time-action and patient experience analyses of locally advanced cervical cancer brachytherapy," *Brachytherapy*, vol. 0, 2024. [Online]. Available: http://www.brachyjournal.com/article/S1538472124000114/fulltexthttp://www.brachyjournal.com/article/S1538472124000114/abstracthttps://www.brachyjournal.com/article/S1538-4721(24)00011-4/abstract

[21] O. V. Gul, G. Inan, and H. Basaran, "Impact of different treatment plans on eqd2 for intracavitary brachytherapy of cervical cancer," *Journal of the Egyptian National Cancer Institute*, vol. 33, pp. 1–8, 12 2021. [Online]. Available: https://jenci.springeropen.com/articles/10.1186/s43046-021-00084-2

[22] P. Annede, I. Dumas, A. Schernberg, A. Tailleur, I. Fumagalli, S. Bockel, F. Mignot, M. Kissel, E. Deutsch, C. Haie-meder, and C. Chargari, "Radiobiological optimization comparison between pulse-dose-rate and high-dose-rate brachytherapy in patients with locally advanced cervical cancer," *Brachytherapy*, vol. 18, pp. 370–377, 5 2019.

[23] B. Chow, B. Warkentin, and G. Menon, "Radiobiological dose calculation parameters for cervix cancer brachytherapy: A systematic review," *Brachytherapy*, vol. 18, pp. 546–558, 7 2019.

[24] M. A. Ebert, A. Haworth, R. Kearvell, B. Hooton, B. Hug, N. A. Spry, S. A. Bydder, and D. J. Joseph, "Comparison of dvh data from multiple radiotherapy treatment planning systems," *Physics in Medicine & Biology*, vol. 55, p. N337, 5 2010. [Online]. Available: https://iopscience.iop.org/article/10.1088/0031-9155/55/11/N04https://iopscience.iop.org/article/10.1088/0031-9155/55/11/N04/meta

[25] "Handbook of radiotherapy physics : Theory and practice," *Handbook of Radiotherapy Physics*, 6 2007. [Online]. Available: https://www.taylorfrancis.com/books/mono/10.1201/9781420012026/handbook-radiotherapy-physics-mayles-nahum-rosenwald

[26] C. Kirisits, F. A. Siebert, D. Baltas, M. D. Brabandere, T. P. Hellebust, D. Berger, and J. Venselaar, "Accuracy of volume and dvh parameters determined with different brachytherapy treatment planning systems," *Radiotherapy and Oncology*, vol. 84, pp. 290–297, 9 2007.

[27] R. Pötter, K. Tanderup, C. Kirisits, A. de Leeuw, K. Kirchheiner, R. Nout, L. T. Tan, C. Haie-Meder, U. Mahantshetty, B. Segedin, P. Hoskin, K. Bruheim, B. Rai, F. Huang, E. V. Limbergen, M. Schmid, N. Nesvacil, A. Sturdza, L. Fokdal, N. B. K. Jensen, D. Georg, M. Assenholt, Y. Seppenwoolde, C. Nomden, I. Fortin, S. Chopra, U. van der Heide, T. Rumpold, J. C. Lindegaard, and I. Jürgenliemk-Schulz, "The embrace ii study: The outcome and prospect of two decades of evolution within the gec-estro gyn working group and the embrace studies," *Clinical and Translational Radiation Oncology*, vol. 9, pp. 48–60, 2 2018.

[28] R. E. Drzymala, R. Mohan, L. Brewster, J. Chu, M. Goitein, W. Harms, and M. Urie, "Dose-volume histograms," *International Journal of Radiation Oncology*Biology*Physics*, vol. 21, pp. 71–78, 5 1991.

[29] D. Berger, J. Dimopoulos, P. Georg, D. Georg, R. Pötter, and C. Kirisits, "Uncertainties in assessment of the vaginal dose for intracavitary brachytherapy of cervical cancer using a tandem-ring applicator," *International journal of radiation oncology, biology, physics*, vol. 67, pp. 1451–1459, 4 2007. [Online]. Available: https://pubmed.ncbi.nlm.nih.gov/17289290/

[30] S. A. Bhide, M. Davies, K. Burke, H. A. McNair, V. Hansen, Y. Barbachano, I. A. El-Hariry, K. Newbold, K. J. Harrington, and C. M. Nutting, "Weekly volume and dosimetric changes during chemoradiotherapy with intensity-modulated radiation therapy for head and neck cancer: A prospective observational study," *International Journal of Radiation Oncology*Biology*Physics*, vol. 76, pp. 1360–1368, 4 2010.

[31] C. V. Guthier, A. L. Damato, A. N. Viswanathan, J. W. Hesser, and R. A. Cormack, "A fast multitarget inverse treatment planning strategy optimizing dosimetric measures for high-dose-rate (hdr) brachytherapy," *Medical physics*, vol. 44, pp. 4452–4462, 9 2017. [Online]. Available: https://pubmed-ncbi-nlm-nih-gov.tudelft.idm.oclc.org/28626978/

[32] E. Lessard and J. Pouliot, "Inverse planning anatomy-based dose optimization for hdr-brachytherapy of the prostate using fast simulated annealing algorithm and dedicated objective function," *Medical physics*, vol. 28, pp. 773–779, 2001. [Online]. Available: https://pubmed-ncbi-nlm-nih-gov.tudelft.idm.oclc.org/11393472/

[33] G. Jozsef, O. E. Streeter, and M. A. Astrahan, "The use of linear programming in optimization of hdr implant dose distributions," *Medical physics*, vol. 30, pp. 751–760, 5 2003. [Online]. Available: https://pubmed-ncbi-nlm-nih-gov.tudelft.idm.oclc.org/12772981/

[34] M. J. Webster, S. Devic, T. Vuong, D. Y. Han, J. C. Park, D. Scanderbeg, J. Lawson, B. Song, W. T. Watkins, T. Pawlicki, and W. Y. Song, "Dynamic modulated brachytherapy (dmbt) for rectal cancer," *Medical physics*, vol. 40, 2013. [Online]. Available: https://pubmed-ncbi-nlm-nih-gov.tudelft.idm.oclc.org/23298088/

[35] T. Siauw, A. Cunha, A. Atamtürk, I. C. Hsu, J. Pouliot, and K. Goldberg, "Ipip: A new approach to inverse planning for hdr brachytherapy by directly optimizing dosimetric indices," *Medical Physics*, vol. 38, pp. 4045–4051, 2011.

[36] B. L. Gorissen, D. D. Hertog, and A. L. Hoffmann, "Mixed integer programming improves comprehensibility and plan quality in inverse optimization of prostate hdr brachytherapy," *Physics in Medicine & Biology*, vol. 58, p. 1041, 1 2013. [Online]. Available: https://iopscience.iop.org/article/10.1088/0031-9155/58/4/1041https://iopscience.iop.org/article/10.1088/0031-9155/58/4/1041/meta

[37] S. Breedveld, A. B. Bennan, S. Aluwini, D. R. Schaart, I. K. K. Kolkman-Deurloo, and B. J. Heijmen, "Fast automated multi-criteria planning for hdr brachytherapy explored for prostate cancer," *Physics in Medicine and Biology*, vol. 64, 10 2019.

[38] B. Morén, T. Larsson, and Åsa Carlsson Tedgren, "An extended dose-volume model in high dose-rate brachytherapy - using mean-tail-dose to reduce tumor underdosage," *Medical physics*, vol. 46, pp. 2556–2566, 6 2019. [Online]. Available: https://pubmed.ncbi.nlm.nih.gov/30972758/

[39] K. L. Sadowski, T. Alderliesten, Y. Niatsetski, M. C. V. D. Meer, D. Thierens, A. Bel, N. H. Luong, R. V. D. Laarse, and P. A. Bosnian, "Exploring trade-offs between target coverage, healthy tissue sparing, and the placement of catheters in hdr brachytherapy for prostate cancer using a novel multi-objective model-based mixed-integer evolutionary algorithm," *GECCO 2017 - Proceedings of the 2017 Genetic and Evolutionary Computation Conference*, pp. 1224–1231, 7 2017. [Online]. Available: https://dl.acm.org/doi/10.1145/3071178.3071311

[40] N. H. Luong, T. Alderliesten, B. R. Pieters, A. Bel, Y. Niatsetski, and P. A. Bosman, "Fast and insightful bi-objective optimization for prostate cancer treatment planning with high-dose-rate brachytherapy," *Applied Soft Computing*, vol. 84, p. 105681, 11 2019.

[41] B. Morén, T. Larsson, and Åsa Carlsson Tedgren, "Optimization in treatment planning of high dose-rate brachytherapy — review and analysis of mathematical models," pp. 2057–2082, 5 2021.

[42] A. Karabis, P. Belotti, and D. Baltas, "Optimization of catheter position and dwell time in prostate hdr brachytherapy using hipo and linear programming," 2009. [Online]. Available: www.springerlink.com

[43] Åsa Holm, Åsa Carlsson Tedgren, and T. Larsson, "Heuristics for integrated optimization of catheter positioning and dwell time distribution in prostate hdr brachytherapy," *Annals of Operations Research*, vol. 236, pp. 319–339, 1 2016. [Online]. Available: https://link-springer-com.tudelft.idm.oclc.org/article/10.1007/s10479-013-1448-7

[44] T. Siauw, A. Cunha, D. Berenson, A. Atamtürk, I. C. Hsu, K. Goldberg, and J. Pouliot, "Npip: A skew line needle configuration optimization system for hdr brachytherapy," *Medical Physics*, vol. 39, pp. 4339–4346, 2012.

[45] E. Poulin, C. A. C. Fekete, M. Létourneau, A. Fenster, J. Pouliot, and L. Beaulieu, "Adaptation of the cvt algorithm for catheter optimization in high dose rate brachytherapy," *Medical Physics*, vol. 40, p. 111724, 11 2013. [Online]. Available: https://onlinelibrary.wiley.com/doi/full/10.1118/1.4826335https://onlinelibrary.wiley.com/doi/abs/10.1118/1.4826335https://aapm.onlinelibrary.wiley.com/doi/10.1118/1.4826335

[46] G. Ayotte, M. D'amours, S. Aubin, Lessard, J. Pouliot, and L. Beaulieu, "Sci—thurs am: Yis—02: Optimizing number and position of catheters within inverse planning simulated annealing (ipsa) for prostate and breast high dose rate brachytherapy," *Medical Physics*, vol. 36, pp. 4315–4315, 9 2009. [Online]. Available: https://onlinelibrary-wiley-com.tudelft.idm.oclc.org/doi/full/10.1118/1.3244162https://onlinelibrary-wiley-com.tudelft.idm.oclc.org/doi/abs/10.1118/1.3244162https://aapm-onlinelibrary-wiley-com.tudelft.idm.oclc.org/doi/10.1118/1.3244162

[47] C. V. Guthier, K. P. Aschenbrenner, R. Müller, L. Polster, R. A. Cormack, and J. W. Hesser, "Real-time inverse high-dose-rate brachytherapy planning with catheter optimization by compressed sensing-inspired optimization strategies," *Physics in Medicine & Biology*, vol. 61, p. 5956, 7 2016. [Online]. Available: https://iopscience.iop.org/article/10.1088/0031-9155/61/16/5956https://iopscience.iop.org/article/10.1088/0031-9155/61/16/5956/meta

[48] A. Garg, S. Patil, T. Siauw, J. A. M. Cunha, I. C. Hsu, P. Abbeel, J. Pouliot, and K. Goldberg, "An algorithm for computing customized 3d printed implants with curvature constrained channels for enhancing intracavitary brachytherapy radiation delivery," *IEEE International Conference on Automation Science and Engineering*, pp. 466–473, 2013.

[49] Y. Duan, S. Patil, J. Schulman, K. Goldberg, and P. Abbeel, "Planning locally optimal, curvature-constrained trajectories in 3d using sequential convex optimization," *Proceedings - IEEE International Conference on Robotics and Automation*, pp. 5889–5895, 9 2014.

[50] S. Patil, J. Pan, P. Abbeel, and K. Goldberg, "Planning curvature and torsion constrained ribbons in 3d with application to intracavitary brachytherapy," *IEEE Transactions on Automation Science and Engineering*, vol. 12, pp. 1332–1345, 10 2015.

[51] S. Bhattacharya, M. Likhachev, and V. Kumar, "Search-based path planning with homotopy class constraints," *Proceedings of the AAAI Conference on Artificial Intelligence*, vol. 3, pp. 2097–2099, 2010.

[52] F. Gao, W. Wu, Y. Lin, and S. Shen, "Online safe trajectory generation for quadrotors using fast marching method and bernstein basis polynomial," *Proceedings - IEEE International Conference on Robotics and Automation*, pp. 344–351, 9 2018.

[53] Y. Ni, S. Mulier, Y. Miao, L. Michel, and G. Marchal, "A review of the general aspects of radiofrequency ablation," *Abdominal Imaging*, vol. 30, pp. 381–400, 8 2005. [Online]. Available: https://link.springer.com/article/10.1007/s00261-004-0253-9

[54] R. Acosta, M. Ehrgott, A. Holder, D. Nevin, J. Reese, and B. Salter, "The influence of dose grid resolution on beam selection strategies in radiotherapy treatment design," *Optimization in Medicine*, pp. 1–23, 12 2008. [Online]. Available: https://link.springer.com/chapter/10.1007/978-0-387-73299-2_1

[55] M. Ehrgott, A. Holder, and J. Reese, "Beam selection in radiotherapy design," *Linear Algebra and its Applications*, vol. 428, pp. 1272–1312, 3 2008.

[56] O. C. Haas, K. J. Burnham, and J. A. Mills, "Optimization of beam orientation in radiotherapy using planar geometry," *Physics in medicine and biology*, vol. 43, pp. 2179–2193, 1998. [Online]. Available: https://pubmed.ncbi.nlm.nih.gov/9725597/

[57] M. Ehrgott and R. Johnston, "Optimisation of beam directions in intensity modulated radiation therapy planning," *OR Spectrum*, vol. 25, pp. 251–264, 2003. [Online]. Available: https://link.springer.com/article/10.1007/s00291-003-0124-8

[58] D. Djajaputra, Q. Wu, Y. Wu, and R. Mohan, "Algorithm and performance of a clinical imrt beam-angle optimization system," *Physics in medicine and biology*, vol. 48, pp. 3191–3212, 10 2003. [Online]. Available: https://pubmed.ncbi.nlm.nih.gov/14579860/

[59] C. H. J. Lee, D. M. Aleman, and M. B. Sharpe, "A set cover approach to fast beam orientation optimization in intensity modulated radiation therapy for total marrow irradiation," *Physics in Medicine and Biology*, vol. 56, pp. 5679–5695, 9 2011. [Online]. Available: https://www.researchgate.net/publication/51559229_A_set_cover_approach_to_fast_beam_orientation_optimization_in_intensity_modulated_radiation_therapy_for_total_marrow_irradiation

[60] D. M. Aleman and M. B. Sharpe, "Optimization methods for total marrow irradiation using intensity modulated radiation therapy," *https://doi.org/10.3138/infor.49.4.234*, vol. 49, pp. 234–240, 11 2017. [Online]. Available: https://www.tandfonline.com/doi/abs/10.3138/infor.49.4.234

[61] L. Liang, D. Cool, N. Kakani, G. Wang, H. Ding, and A. Fenster, "Automatic radiofrequency ablation planning for liver tumors with multiple constraints based on set covering," *IEEE Transactions on Medical Imaging*, vol. 39, pp. 1459–1471, 5 2020. [Online]. Available: https://ieeexplore.ieee.org/document/8890690/

[62] P. Yu, T. Fu, C. Wu, Y. Jiang, and J. Yang, "Automatic radiofrequency ablation planning for liver tumors: A planning method based on the genetic algorithm with multiple constraints," *ACM International Conference Proceeding Series*, pp. 8–14, 8 2021. [Online]. Available: https://dl.acm.org/doi/10.1145/3484377.3484379

[63] S. Kulkarni-Thaker, D. M. Aleman, and A. Fenster, "A row-generation approach for simultaneous multiple needle trajectory planning in radiofrequency ablation," *medRxiv*, p. 2021.06.11.21258244, 6 2021. [Online]. Available: https://www.medrxiv.org/content/10.1101/2021.06.11.21258244v1https://www.medrxiv.org/content/10.1101/2021.06.11.21258244v1.abstract

[64] E. Altobelli, M. Amichetti, A. Langiu, F. Marzi, F. Mignosi, P. Pisciotta, G. Placidi, F. Rossi, G. Russo, M. Schwarz, S. Smriglio, S. Vennarini, E. Altobelli, M. Amichetti, A. Langiu, F. Marzi, F. Mignosi, P. Pisciotta, G. Placidi, F. Rossi, G. Russo, M. Schwarz, S. Smriglio, and S. Vennarini, "Combinatorial optimisation in radiotherapy treatment planning," *AIMS Medical Science 2018 3:204*, vol. 5, pp. 204–223, 2018. [Online]. Available: http://www.aimspress.com/article/doi/10.3934/medsci.2018.3.204http://www.aimspress.com/rticle/doi/10.3934/medsci.2018.3.204

[65] "Gurobi optimizer reference manual - gurobi optimization." [Online]. Available: https://www.gurobi.com/documentation/current/refman/index.html

[66] B. McNally, Y. Lu, E. Shively-Ertas, M. S. Song, and F. J. Vasko, "A simple and effective methodology for generating bounded solutions for the set k-covering and set variable k-covering problems: A guide for or practitioners," *Review of Computer Engineering Research*, vol. 8, pp. 76–95, 2021.

[67] L. Mrkela and Z. Stanimirović, "A variable neighborhood search for the budget-constrained maximal covering location problem with customer preference ordering," *Operational Research*, vol. 22, pp. 5913–5951, 11 2022. [Online]. Available: https://link.springer.com/article/10.1007/s12351-021-00652-3

[68] D. Chauhan, A. Unnikrishnan, and M. Figliozzi, "Maximum coverage capacitated facility location problem with range constrained drones," *Transportation Research Part C: Emerging Technologies*, vol. 99, pp. 1–18, 2 2019.

[69] S. B. Mehdi, R. Choe, V. Cichella, and N. Hovakimyan, "Collision avoidance through path replanning using bézier curves," *AIAA Guidance, Navigation, and Control Conference 2015, MGNC 2015 - Held at the AIAA SciTech Forum 2015*, 2015.

[70] R. C. Veltkamp and W. Wesselink, "Modeling 3d curves of minimal energy," *Computer Graphics Forum*, vol. 14, pp. 97–110, 8 1995. [Online]. Available: https://onlinelibrary.wiley.com/doi/full/10.1111/j.1467-8659.1995.cgf143_0097.xhttps://onlinelibrary.wiley.com/doi/abs/10.1111/j.1467-8659.1995.cgf143_0097.xhttps://onlinelibrary.wiley.com/doi/10.1111/j.1467-8659.1995.cgf143_0097.x

[71] E. H. Doha, A. H. Bhrawy, and M. A. Saker, "Integrals of bernstein polynomials: An application for the solution of high even-order differential equations," *Applied Mathematics Letters*, vol. 24, pp. 559–565, 4 2011.

[72] Y. J. Ho and J. S. Liu, "Collision-free curvature-bounded smooth path planning using composite bezier curve based on voronoi diagram," *Proceedings of IEEE International Symposium on Computational Intelligence in Robotics and Automation, CIRA*, pp. 463–468, 2009.

[73] C. E. Luis, M. Vukosavljev, and A. P. Schoellig, "Online trajectory generation with distributed model predictive control for multi-robot motion planning," *IEEE Robotics and Automation Letters*, vol. 5, pp. 604–611, 4 2020.

[74] T. Mercy, R. V. Parys, and G. Pipeleers, "Spline-based motion planning for autonomous guided vehicles in a dynamic environment," *IEEE Transactions on Control Systems Technology*, vol. 26, pp. 2182–2189, 11 2018.

[75] J. W. Chang, Y. K. Choi, M. S. Kim, and W. Wang, "Computation of the minimum distance between two bézier curves/surfaces," *Computers & Graphics*, vol. 35, pp. 677–684, 6 2011.

[76] G. V. den Bergen, "A fast and robust gjk implementation for collision detection of convex objects," *Journal of Graphics Tools*, vol. 4, pp. 7–25, 1 1999. [Online]. Available: https://www.tandfonline.com/doi/abs/10.1080/10867651.1999.10487502

[77] B. Sabetghadam, R. Cunha, and A. Pascoal, "Real-time trajectory generation for multiple drones using bézier curves," *IFAC-PapersOnLine*, vol. 53, pp. 9276–9281, 1 2020.

[78] H. W. Kuhn, "The hungarian method for the assignment problem," *Naval Research Logistics Quarterly*, vol. 2, pp. 83–97, 3 1955. [Online]. Available: https://onlinelibrary.wiley.com/doi/full/10.1002/nav.3800020109https://onlinelibrary.wiley.com/doi/abs/10.1002/nav.3800020109https://onlinelibrary.wiley.com/doi/10.1002/nav.3800020109

[79] R. Regele and P. Levi, "Cooperative multi-robot path planning by heuristic priority adjustment," *2006 IEEE/RSJ International Conference on Intelligent Robots and Systems*, pp. 5954–5959, 2006.

[80] C. M. Clark, T. Bretl, and S. Rock, "Applying kinodynamic randomized motion planning with a dynamic priority system to multi-robot space systems," *IEEE Aerospace Conference Proceedings*, vol. 7, pp. 3621–3631, 2002.

[81] A. Manikandan, B. Sarkar, V. T. Rajendran, P. R. King, N. V. M. Sresty, R. Holla, S. Kotur, and S. Nadendla, "Role of step size and max dwell time in anatomy based inverse optimization for prostate implants," *Journal of Medical Physics / Association of Medical Physicists of India*, vol. 38, p. 148, 7 2013. [Online]. Available: https://www.ncbi.nlm.nih.gov/pmc/articles/PMC3775040/

A APPENDIX

A.1. BICYCLE WISHLIST FOR THE GRID CONFIGURATION

Table A.1: Table containing the BiCycle wishlist used for the grid configuration.

Structure	Min/Max	Function	Measure	Limit	Goal	Sufficient	Priority
			Constraints				
Bladder	Minimise	Dose- Volume	D2cc	2	-	-	Constraint
Rectum	Minimise	Dose- Volume	D2cc	2	-	-	Constraint
Sigmoid	Minimise	Dose- Volume	D2cc	2	-	-	Constraint
Smoothing	Minimise	Quadratic		50	-	-	Constraint
Bowel	Minimise	Dose- Volume	D2cc	2	-	-	Constraint
RectoVaginalPoint	Minimise	Linear		Q	-	-	Constraint
			Objectives				
CTV IR	Maximise	Dose- Volume	V98	-	98	98	1
CTV HR	Maximise	Dose- Volume	V90	-	91.3	91.3	3
Bladder	Minimise	Dose- Volume	D2cc	-	2	2	6
Bladder	Minimise	EUD		-	100	0.01	6
Rectum	Minimise	Dose- Volume	D2cc	-	2	2	7
Rectum	Minimise	EUD		-	100	0.01	7
Bowel	Minimise	Dose- Volume	D2cc	-	2	2	8
Sigmoid	Minimise	Dose- Volume	D2cc	-	2	2	8
RectoVaginalPoint	Minimise	Linear	Dmax	-	R	0.01	8
Bowel	Minimise	EUD		-	100	0.01	8
Sigmoid	Minimise	EUD		-	100	0.01	8
Vaginal Top Left	Minimise	Linear	Dmax	-	S	S	12
Vaginal Top Right	Minimise	Linear	Dmax	-	T	T	12
Al	Maximise	Linear	Dmax	-	0	N	13
Ar	Maximise	Linear	Dmax	-	0	O	13
Smoothing	Minimise	Quadratic		-	1000	0	14

A.2. BiCycle wishlist for the clinical and the ARCHITECT configurations

Table A.2: Table containing the BiCycle wishlist used for the clinical and ARCHITECT configurations.

Structure	Min/Max	Function	Measure	Limit	Goal	Sufficient	Priority
			Constraints				
GTV res	Minimise	Linear		C	-	-	Constraint
Bladder	Minimise	Dose- Volume	D2cc	2	-	-	Constraint
Rectum	Minimise	Dose- Volume	D2cc	2	-	-	Constraint
Sigmoid	Minimise	Dose- Volume	D2cc	2	-	-	Constraint
Bowel	Minimise	Dose- Volume	D2cc	2	-	-	Constraint
RectoVaginalPoint	Minimise	Linear		Q	-	-	Constraint
Smoothing	Minimise	Quadratic	Tandem/Intra	200	-	-	Constraint
Smoothing	Minimise	Quadratic	Needle	400	-	-	Constraint
			Objectives				
CTV IR	Maximise	Dose- Volume	V98	-	98	98	1
CTV HR	Maximise	Dose- Volume	V90	-	90	90	3
Bladder	Minimise	Dose- Volume	D2cc	-	2	2	6
Bladder	Minimise	EUD		-	100	0.01	6
Rectum	Minimise	Dose- Volume	D2cc	-	2	2	7
Rectum	Minimise	EUD		-	100	0.01	7
Bowel	Minimise	Dose- Volume	D2cc	-	2	2	8
Sigmoid	Minimise	Dose- Volume	D2cc	-	2	2	8
Bowel	Minimise	EUD		-	100	0.01	8
Sigmoid	Minimise	EUD		-	100	0.01	8
RectoVaginalPoint	Minimise	Linear	Dmax	-	R	0.01	8
Vaginal Top Left	Minimise	Linear	Dmax	-	S	S	12
Vaginal Top Right	Minimise	Linear	Dmax	-	T	T	12
Al	Maximise	Linear	Dmax	-	0	N	13
Ar	Maximise	Linear	Dmax	-	0	O	13
Smoothing	Minimise	Quadratic	Tandem/Intra	-	200	0	14
Smoothing	Minimise	Quadratic	Needle	-	400	0	14